

https://dspace.org/

The effect of the presence of species mimicking metal-support interactions adsorbed on a Co(0001) metal surface

Mohotlhoane, Sifiso Alec

2016

http://hdl.handle.net/10539/21752

Mohotlhoane, Sifiso Alec (2016) The effect of the presence of species mimicking metal-support interactions adsorbed on a Co(0001) metal surface, University of Witwatersrand, Johannesburg, <http://wiredspace.wits.ac.za/handle/10539/21752>

Downloaded from a DSpace repository. https://dspace.org/

The effect of the presence of species mimicking metal-support interactions adsorbed on a Co(0001) metal surface

By

S.A. Mohotlhoane



A Dissertation submitted in fulfillment of the requirements for the degree

Master of Science

in the Faculty of Sciences

at the University of the Witwatersrand, Johannesburg

October 2016

Declaration

I, Sifiso Alec Mohotlhoane, hereby declare that the work on which this thesis is based, has not, to my knowledge, previously been submitted for a degree at this or any other university. This work is my own and all reference material that has been used or quoted has been indicated and acknowledged.

_____

Sifiso Alec Mohotlhoane

_____day of_____20 ___in _____

Dedication

To my mom

Dolly Mohotlhoane

Acknowledgements

I would like to thank my family for their continuous support and patience over the course of my studies.

My supervisors Dr Lerotholi and Dr Doyle for affording me the opportunity to learn from their wisdom, experiences and their guidance throughout my studies.

UJ Physics department, for the use of Ultra High Vacuum (UHV) facilities.

A HUGE thank you to the CATOMMAT group, you managed to make the journey bearable and fun.

To Professor Neil Coville, words cannot define how grateful I am. Thanks a lot and may the Lord continue to bless you.

The financial support of SASOL and C^* change towards these studies is acknowledged.

To my better half and pillar of strength Basetsane Khoza for her patience, support and motivation during my studies and last but not least the Almighty God for His blessings.

Abstract

The adsorption of molecules on a metal surface is core in heterogeneous catalysis. Surface sensitive techniques such as low energy electron diffraction (LEED), X-ray photoelectron spectroscopy (XPS) and temperature programmed desorption (TPD) are key tools to study adsorption geometries and structures of molecules and atoms on a metal surface. As our first model system we investigated the dissociation of NO on Ir{100}. The LEED experimental results showed a $p(2 \times 2)$ diffraction pattern at 300 K using. In this study two options were explored: phase mixing where dissociated nitrogen and oxygen are on the same unit cell, as well as phase separation where both nitrogen and oxygen form their own separate unit cell which results in a $p(2 \times 2)$ unit cell.

Calculations were done on atop, bridge and hollow sites, with only perpendicular parameters and vibrational amplitude being varied initially. Results for phase mixing calculations gave the lowest R-factor of 0.70 ± 0.11 for atop site. We further considered phase separation for hollow and bridge sites for nitrogen and oxygen respectively because these two sites were found to be the most stable sites using DFT from previous studies.

The lowest R-factors were 0.37 ± 0.06 for nitrogen c(2x2) and 0.24 ± 0.13 for oxygen $p(2 \times 1)$ For oxygen significant row pairing of iridium atoms stabilized the structure as mentioned in previous studies. Therefore from our results it is evident that phase separation models the experimental data better than phase mixing. Nitrogen and oxygen form $c(2 \times 2)$ and $p(2 \times 1)$ overlayer structures respectively which in combination result in a $p(2 \times 2)$ pattern that is in agreement with experimental results.

The second system involves enantio-selectivity and chiral resolution at the organic-inorganic interfaces. The d-serine molecule was adsorbed on the Cu{110} surface. Density functional theory (DFT) calculations were used as a benchmark for our CLEED calculations. LEED experiments showed a $(-1 + 2{:}4\ 0)$ overlayer pattern for d-serine adsorbed on Cu{110} surface. Three structures from DFT calculations with the lowest energy were used for CLEED calculations.

These structures differed by the way they bond to the surface and molecular interactions. Calculations were carried out on these three structures and the structure with intra-dimer bonding was the best structure. The searches for this structure were further optimized by introducing pairing of the atoms in the row reconstruction on the copper surface and angle search. The lowest value obtained was 0.37 ± 0.09, which suggests that further understanding of this system is needed.

The ultra-high vacuum (UHV) chamber was fully commissioned and is now ready for TPD and XPS studies.

Table of Contents

1. Declaration 2
2. Dedication 3
3. Acknowledgements 4
4. Abstract 5

List of figures 10

5. **Chapter 1** 13

1.1 General Background 13

1.2 Aims and Objectives 17

1.3 Dissertation Organization 18

6. **Chapter 2** 19

Literature review 19

2.1 Introduction 19

Surface science experimental techniques 19

2.2 Photoelectron spectroscopy 20

2.2.1 Basic principles 20

2.2.2 Basic component for XPS measurements 22

2.3 Temperature programmed adsorption (TPD) 26

2.3.1 Basic experimental requirements 27

2.3.2 Basic principles 28

7. **Chapter 3** 32

Low Energy Electron Diffraction (LEED) 32

3.1.1 Basic Principles 32

3.1.2 The LEED pattern 34

3.2 CLEED program 36

3.2.1 Introduction 36

3.2.2 Description of the CLEED program 36

3.2.3 Accuracy of the structure determination 40

3.3 CLEED modification 41

3.3.1 Multiple domains 41

3.4 CLEED calculations: NO adsorbed on Ir{100} and D-serine adsorbed on Cu{110} **42**
8. **CHAPTER 4** **43**
4.1 Literature review **43**
4.1.1 Metal support interactions **43**
4.1.2 Studies of CO adsorption on Co(0001) **43**
4.2 UHV chamber commissioning **48**
4.2.1 Introduction **48**
4.2.3 Commissioning and calibrating the XPS technique **53**
4.2.4 Commissioning the components for TPD. **56**
4.2.4.1 Testing the heating by radiation method for TPD analysis **60**
4.2.5 Commissioning other components of the chamber. **61**
9. **CHAPTER 5** **64**
NO on Ir{100} **64**
5.1 Introduction **64**
5.2 Literature review **65**
5.3 Results and discussions **66**
5.3.1 Clean surface structure of Ir{100}-1 × 1 ..... **67**
5.3.2 NO on Ir{100} **70**
5.3.2.1 Phase mixing calculations **71**
5.3.2.1 Phase separation calculations **71**
. 5.3.2.1 Calculations for oxygen only **72**
5.3.2.2 Calculations for N only **77**
5.4 Conclusions **80**
10. **CHAPTER 6** **82**
D-serine on Cu{110} **82**
6.1 Introduction **82**
6.2 D-serine **83**
6.3 Literature review on D-serine on Cu{110} **84**
6.4 Experimental and calculation methods **85**
6.5 Results and discussions **86**
6.5.1 Clean Cu{110} surface **88**
6.5.2 D-serine adsorbed on Cu{110} **90**

6.5.2.1 Conclusions and future work 95

11. **Appendix** **97**

Mixed phase N+O 97

Phase Separation N only c(2x2) 99

Phase separation p(2x2) 101

Phase separation p(2x1) O 102

D-serine on Cu{110} 104

12. **References** 107

List of figures

Figure 1.1: Schematic diagram illustrating the "pressure gap" between surface science and technical catalysis. The variable "structure complexity" refers to the surface structure of the catalytic material.

Figure 2.1: Graphical summary of the photoemission process. The figure was reproduced from reference. 13.[13]

Figure 2.2: Schematic of an XPS spectrometer system illustrating the radiation source, electron energy analyzer, sample and detector. A hemispheric electron analyzer is used for the specific example shown here. The abbreviations OH and IH stand for outer and inner hemisphere respectively.

Figure 2.3: Graphical description of the photoemission process. The grey-shaded area represents the valence band of the sample. The inset figures give examples of recorded photoemission spectra where the lower and upper spectrum show the C 1s core level and valence band spectra respectively. The two arrows in the upper inset figure indicate CO related peaks. The figure was reproduced from reference 26.

Figure 3.1: Schematic of a conventional LEED system. The figure was reproduced from reference 20.

Figure 3.2: The iteration process used in the CLEED package to solve the surface crystal structure.

Figure 3.3: Schematic illustrating the "trial and error" method used in CLEED structural determination calculation. Figure reproduced from reference 67.

Figure 4.1: The vacuum development time scale from 1660 to 1900. Note that there is a break in the time scale. Figure reproduced from reference 26.

Figure 4.2: The vacuum development time scale from 1900 to 1950. Figure reproduced from reference 26.

Figure 4.3: A picture showing a gasket and a flange which are parts used in a UHV chamber.

Figure 4.4: A picture of the UHV chamber wrapped with an aluminium foil during baking.

Figure 4.5: Illustration of the sample manipulator and the gold foil.

Figure 4.6: Spectrum of the Au 4*f* peaks at a pass energy of 200 eV, illustrating the shift in peak positions between spectra (a) and (b).

Figure 4.7: Spectrum of the Au 4*f* peaks at pass energy of 50 eV, after calibration. The peak positions are close to the literature values.

Figure 4.8: Spectrum of the Au 4*f* peaks at a pass energy of 50 eV, illustrating the increase in counts after sputtering the sample.

Figure 4.9: A schematic of the sample holder made from stainless steel and the Co{0001} crystal mounted using a tungsten wire.

Figure 4.10: A schematic illustration of the concept of electron heating for TPD technique.

Figure 4.11: The schematic illustration of a) a shield in place between the sample holder and the filament b) the filament and sample without the shield.

Figure 4.12: A picture showing the home-made glass doser and a valve connected to the chamber.

Figure 4.13: Mass spectra of fragments of aluminium tri-sec-butoxide, (left) from our doser test and compared to literature results (right).

Figure 5.1: (a) image observed during LEED experiments at 120 eV and (b) a pattern drawn using LEEDpat program of a (2×2) diffraction pattern.

Figure 5.2: Side view of the schematic structure of Ir{100} clean surface.

Figure 5.3: Comparison of experimental (solid lines) and theoretical (dashed lines) I-V curves for the structure of clean Ir{100} shown in figure 5.2.

Figure 5.4: Possible configurations of phase mixing for dissociated NO on Ir{100}, where in configuration A atoms are adsorbed on an atop site, B and C on a bridge site and D on a hollow site. The red and blue spheres are oxygen and nitrogen respectively.

Figure 5.5: A schematic of LEED patterns in real and reciprocal space; showing that combining a $p(1 \times 2)$ (left) and $c(2 \times 2)$ (right) results in a $p(2 \times 2)$ (bottom).

Figure 5.6: Schematic top view of oxygen adsorbed on a bridge site of Ir{100} surface in a $p(1 \times 2)$ overlayer. The arrows indicate the direction of the row pairing reconstruction.

Figure 5.7: Side view of the schematic structure of O on Ir{100} surface.

Figure 5.8: Comparison of experimental (solid lines) and theoretical (dashed lines) I-V curves for the structure of O on Ir{100} shown in figure 5.7.

Figure 5.9: Possible configurations of N on Ir{100} for: (a) $p(2 \times 2)$ and (b) $c(2 \times 2)$ overlayers.

Figure 5.10: Side view of the schematic structure of N on Ir{100} surface.

Figure 5.11: Comparison of experimental (solid lines) and theoretical (dashed lines) I-V curves for the structure of N on Ir{100} shown in figure 5.10.

Figure 5.12: A schematic of the islands formed when NO dissociates on Ir{100}-(1×1) surface at 300 K.

Figure 6.1: Molecular structure models of L and D serine, left and right respectively. The figure was reproduced from reference 68.

Figure 6.2: The molecular structure of the three models with the lowest energy adsorbed on Cu{110}.

Figure 6.3: Comparison of experimental (solid lines) and theoretical (dashed lines) I-V curves for the structure of Cu{110} shown in figure 6.4.

Figure 6.4: Side view of the schematic structure of Cu{110} clean surface.

Figure 6.5: Schematic models of d-serine adsorbed on Cu{110} surface unit cell with the growth direction domains w_2 and substrate vectors a_1 and a_2. (b) Mimicked row pairing reconstruction on the d-serine unit cell. Figured reproduced from reference 68.

Figure 6.6: Schematic of the Cu atoms in a unit cell and an illustration of the reconstruction introduced in the optimization of structure #001 where the atoms in a row are paired.

Figure 6.7: Comparison of experimental (solid lines) and theoretical (dashed lines) I-V curves for the structure of d-serine on Cu{110} .

Chapter 1

1.1 General Background

In the last 30 years the research field of surface science has developed enormously and new techniques are continually being developed to study clean surfaces and surfaces covered with adsorbates.[1] The continuous growth and development of surface science as an interdisciplinary research area is accredited to the interaction of concepts in physical chemistry, condensed matter physics and the evolution of technologies like semiconductor microelectronics, vacuum processing and the construction of scanning probe microscopes. Theoretical tools and most of the concepts used in the field stem from condensed matter physics and physical chemistry. For example, electron emission and scattering for surface characterization, electron tunneling for imaging and density functional theory (DFT) for prediction of surface structure and reaction dynamics.[2]

There are four major events that contributed to the rapid and significant development of the surface science research area. The first event occurred in the 1960's when a combination of ultra-high vacuum (UHV) technology and the theoretical knowledge that electrons in the range of 50 to 500 eV possess inelastic mean free paths in the order of a few angstroms gave birth to the field. This then enabled the production of clean surfaces that could stay adsorbate free for a long period of time, thus making it possible to study surfaces and surface processes. The theory of electron-solid scattering was revised and became the foundation of electron spectroscopy in surface characterization.[1,2] The second event began in the 1980's and this involved the discovery of transistors and the development of the semiconductor industry. This produced good electronics that enabled the use of multiple sophisticated surface characterization probes simultaneously in a UHV chamber. This then made fabrication and control of surfaces the driving force in technological developments. [1,2]

The third event was the energy crisis that took place in the 1970's. This propelled the development of catalyst based processes in the oil and petroleum industry and further development of surface science. The fourth event entailed the invention of the scanning tunneling microscope (STM) in the 1980's and its maturation in the 1990's. This made atomic-resolution imaging of complex microscopic surfaces possible and videos of the dynamics of their evolution led to a profound understanding of processes such as growth, deposition etching and chemical reactions. This event also involved the use of surface science to study complex system such as fragile biological samples and liquid-solid interfaces. Although the latter is still at its developmental stage it shows a lot of ground breaking potential.[1,2]

Characterization and understanding of surfaces at a molecular level was a prerequisite for the development of sensors, new catalysts and smaller semiconductor based devices. This then meant new surface science based technologies had to be developed that would enable or improve molecular level study of surfaces. Single crystals were used as surfaces in the early studies and they are still used even today, mainly because they provide control over surface structure which is an element in controlling surface properties. The use of single crystals also makes it easier to compare experimental and theoretically studies. In other studies such as selective gas adsorption and catalysis, high surface porous materials are used in contrast to single crystals.[3]

Studying surfaces and surface reactions at the atomic and molecular level defines modern surface science. There is a lot of information that can be obtained from a surface science analysis of a system but the most important piece of information is the position of atoms on the interface, a phenomenon known as surface crystallography. The structure of the surface is different from the bulk termination structure largely because both the coordination and electronic structure is significantly different from that of the bulk. The modification from bulk to surface comes in several forms such as defects, relaxation, reconstructions or even more drastic modifications, that include mass transport of atoms across the surface resulting in notable changes in surface atom's coordination and symmetry.[3]

These effects mentioned above were identified for clean metal surfaces; because it was a tradition to model the surface layer as a "rigid" bulk terminated structure during adsorption studies. This assumption came about mainly because surface science techniques available at that time had a shortfall of not being able to handle the complexity that comes when surface layers

were allowed to reconstruct.[4] The rationale to this assumption was that when adsorbates adsorb on the clean metal surface the surface layer returns to its bulk termination coordination. This assumption was changed because modern techniques allowed the determination of the geometry of both the adsorbates and underlying surface atoms. [5] Employing clean metal surfaces as a reference it was found that the top layers of a metal actually undergo reconstruction during adsorption studies. Therefore the rigid layer model was replaced by a mobile plastic model which responds to the presence of adsorbate atoms or molecules on the surface which induce structural modifications. Studies of adsorbates are more complex when compared to clean surface studies mainly because they have more parameters that need optimizing during structural determination studies. Nonetheless significant progress has been made in the field of surface science which helps overcome the challenges posed by the increased parameters.[3]

Surface science has been used to study and understand heterogeneous catalysts mainly because catalysis is the foundation of most chemical and petrochemical technologies as well as its importance in life science and environmental protection technologies. Modern surface science makes it possible to study catalysts on an atomic scale and understand molecular constituents that make them function. In the early 1960's prior to the use of surface science, heterogeneous catalysts were viewed as a "black box" that converts reactants into desired products. From the 1990's catalyst design based on knowledge gained from surface science studies become a norm rather than an exception. [6]

The use of surface science in heterogeneous catalysis also has short fallings or criticisms. The common criticism is that surface science uses UHV and (mostly) single crystal surfaces which are far from reality when it comes to technical heterogeneous catalysis reaction conditions. These differences between the two fields are called the "pressure and material gap". Figure 1.1 shows a diagram (graph) that strives to illustrate the extent of the "pressure and material gap" between UHV surface science and technical catalysis. The vertical axis of the figure gives pressure and the horizontal axis "structural complexity". As an example, the horizontal axis illustrates that smooth single crystals of low miller index have single surfaces and are less complex. This is in contrast to single crystals with evenly dispersed kinks with higher well-defined structure complexity. Thus the horizontal axis illustrate the variety of catalytic materials and this correlates to the "material gap" since less complex structures are used in ideal surface

science in contrast to highly complex materials employed in technical catalysis. Similarly for pressure, technical catalysis processes occur at higher pressures and ideal surface science occurs at much lower pressures. The extended surface science and catalytic model experiments are illustrated which are a bridge between ideal surface science and technical catalysis. The variation in "material gap" is also shown.

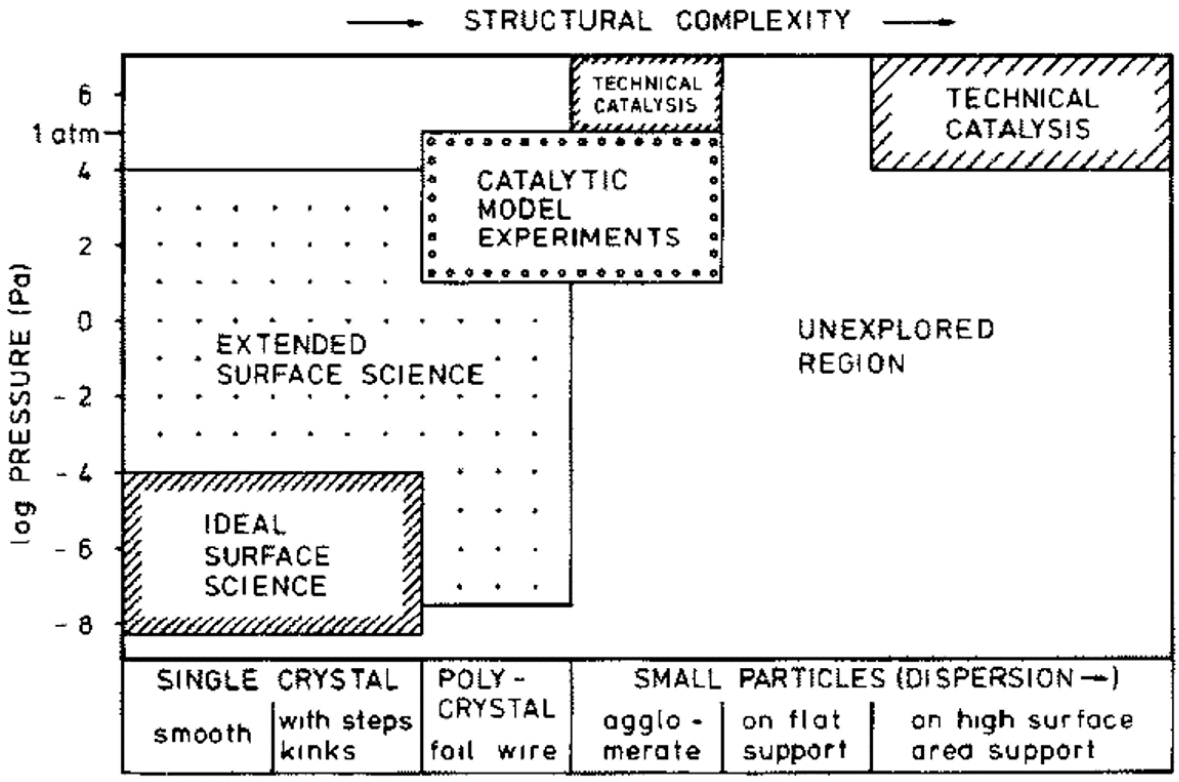

Figure 1.1: Schematic diagram illustrating the "pressure gap" between surface science and technical catalysis. The variable "structure complexity" refers to the surface structure of the catalytic material. The figure was reproduced from reference 7.[7]

In essence the diagram shows where technical catalysis and surface science falls in terms of pressure and structure complexity. The figure also illustrate the work that has been done to try and bridge the "pressure gap" while for the "material gap" the region of material with high complexity has not been explored as yet. [7]

There have been several efforts to bridge the "pressure gap" between UHV and practical catalytic studies such as the incorporation of high pressure cells into UHV chambers. This has

made it possible to perform catalytic kinetic studies under conditions identical to those in reactors used in chemical technologies or industries and carry out surface science analytical measurements before and after a reaction.[8] The appearance of products and the disappearance of reactants can be monitored using a quadrupole mass spectrometer. These studies are done on well-defined single crystal surfaces using a plane that will model a site or set of sites that are anticipated to exist on practical catalysts. The mating of UHV and a high pressure cell has enabled detailed studies of the effects of inhibitors/promoters on catalytic activity, structure sensitivity and in some cases identification of reaction intermediates by analyzing post reaction surface measurements. These kinds of studies have provided data that rationalized the use of single crystals to model various reactions that employ complex practical catalysts and as a reference for evaluating industrial catalytic systems. Even though modelling of catalysts has been successful there is still a need for development of model systems with a high level of complexity in order to be able to study issues related to very small particles and interactions between the support and particles. This includes bridging the "material gap" as well.[6,8]

There have been efforts to bridge the "material gap" such as preparing model catalysts in thin film form in contrast to single crystal form. More complex model catalysts have been prepared by growing atomic layers of Fe_2O_3 or TiO_2 on metal single crystal surfaces using atomic layer epitaxy. Growing four to eight monolayers of the oxides mimics the catalytic behavior of a high surface area oxide catalyst. Catalyst promoters or modifiers can also be studied by depositing them from the vapor phase on the model metal single crystal surface. This gives information on their effect on the catalytic behavior as bonding or structure modifiers. This is an indication that complex catalytic systems can be mimicked by growing or depositing layers on the surface of the model single crystal metal.[6]

1.2 Aims and Objectives

The aims of this masters work was to start by commissioning a multifaceted UHV chamber with facilities for X-ray photoelectron spectroscopy (XPS), low energy electron diffraction (LEED) and temperature programmed desorption (TPD). The aim was then to use the multifaceted UHV chamber to study the effect of the presence of species mimicking strong metal support interactions adsorbed on a Co metal surface using the surface science approach. The metal

support interactions will be studied on Co using Co{0001} single crystal as a model surface. The focus will be on alumina type interactions, and these will be made by adsorbing aluminium tri-sec-butoxide on the Co{0001} single crystal surface. CO will be used as a probe molecule to investigate the influence of the presence of species mimicking the metal-support interactions. The results will then be compared to theoretical DFT studies which are being done at University of Cape Town.

This will be followed by the structure determination of two surface science systems using the Cambridge low energy electron diffraction (CLEED) program. The first system involves the adsorption of NO on Ir{100} and the other system is the adsorption of d-serine on Cu{110} surface. For both systems the main aim is to solve the structure using data obtained from LEED experiments. For the NO adsorbed on Ir{100} we will be solving the (2×2) structure formed when NO was adsorbed at room temperature. While for the d-serine system we have the LEED pattern and need to solve the structure of supra-structures formed has a (-1 +2; 4 2) lattice on the Cu(110) surface.

1.3 Dissertation Organization

There are six chapters, including this chapter, the introduction which summarizes the history, concepts and the use of surface science in heterogeneous catalysis. In chapter 2 basic concepts needed to understand surface science and an introduction on the surface science techniques, XPS and TPD. This will be followed by chapter 3 where the LEED surface technique will be explained then followed by the operating procedure and the theory behind the CLEED program. In the main sections chapter 4, 5 and 6 experimental results are presented and discussed. Chapter 4 discusses the commissioning of the UHV chamber with aim of studying the effects of mimicking metal-support interactions. This was done by adsorbing aluminium tri-sec-butoxide on Co{0001} surface and use CO to probe the interactions. In chapter 5 and 6 CLEED calculations for NO on Ir{100} and d-serine on Cu{100} respectively are presented and discussed.

Chapter 2

Literature review

In this chapter basic ideas necessary for understanding surface science concepts and techniques will be reviewed. The basic theory of x-ray photoelectron spectroscopy (XPS), and temperature programmed desorption (TPD) will be discussed and low energy electron diffraction (LEED) will discussed in the next chapter.

2.1 Introduction

Surface science experimental techniques

Surfaces of metals are studied using surface science techniques that give information on the structure, and the composition of the surface are required. These techniques must also provide the identity, position and the geometry of the adsorbed species.[9] The latter information is more useful if it is provided at the atomic scale. Surface techniques can also be time-resolved so as to allow for effective studying of kinetics for dynamic processes such as adsorption, desorption, reaction on the surface and ordering.[9,10] To achieve the above mentioned requirements two prerequisites should be met which are high surface sensitivity and the capability to produce clean surfaces that remain adsorbate free for a long period of time. Surface sensitivity is achieved by using particles possessing a short inelastic mean free path such as low energy electrons. Ultra-high vacuum (UHV) is used to meet the second prerequisite.

Several surface science techniques are used to study heterogeneous catalysis model systems but we will focus mainly on the three techniques used in this study. These are x-ray photoelectron spectroscopy (XPS), temperature programmed desorption (TPD) and low energy electron diffraction (LEED).

2.2 Photoelectron spectroscopy

XPS has become a widely used technique to study properties of molecules, solids and surfaces. It has developed enormously since the first experiment of its kind by Robinson and Rawlinson in 1914 to its current state. Most of the growth occurred in the past 10 to 30 years which was stimulated by pioneering studies that begun in the 1950's. It all started from the observation by Siegbahn and colleagues that core photoelectron peak intensities are useful in quantitative analysis and that core electron binding energies possess chemically-induced shifts. The latter coupled with the development of the interpretive theory has provided a well-nourished pool of information that can be obtained from analyzing different aspects of XPS spectra.[11]

2.2.1 Basic principles

Photoemission is a process based on Einstein's theory of the photoelectric effect. In photoelectric effect theory, a photon prompts the emission of an electron from the surface of a metal as shown in figure 2.1. The photon can only induce the emission of the photoelectron if it has an energy greater than the work function (minimum energy needed to move an electron from the highest occupied energy level to the "vacuum" level) of the metal.[9,12] The emitted electron can be from either the core or Fermi (valence) level depending on the energy of the incident photon as illustrated in figure 2.1 which shows the core level electron excitation. This is the principle which the XPS technique is based on. A monochromatic beam of x-rays is used in XPS experiments, and is produced by bombarding a metal anode with electrons which results in the emission of an x-ray beam and then a monochromator may be employed to produce a monochromatic beam.[12] When the x-ray beam is incident on the metal it induces the emission of photoelectrons. The emitted electrons are collected and go through an electron lens into a concentric hemispherical analyzer as shown in figure 2.2. This analyzer consist of a potential difference which allows only electrons of a chosen kinetic energy (known as "pass energy") to pass through to the detector, which then measures how many electrons there are of that total energy. A XPS spectrum is then obtained which is the intensity of the electron signal against the kinetic energy of the electrons. The binding energy of the electrons can then be calculated using

equation 2.1**.** XPS is surface sensitive and it is used for identifying, to analyze and quantifying atoms that are on or near the surface, to give the surface composition.[9,12] The main aim of XPS spectral analysis is to determine the location, intensities and in some instances the shapes of the various peaks observed.[9]

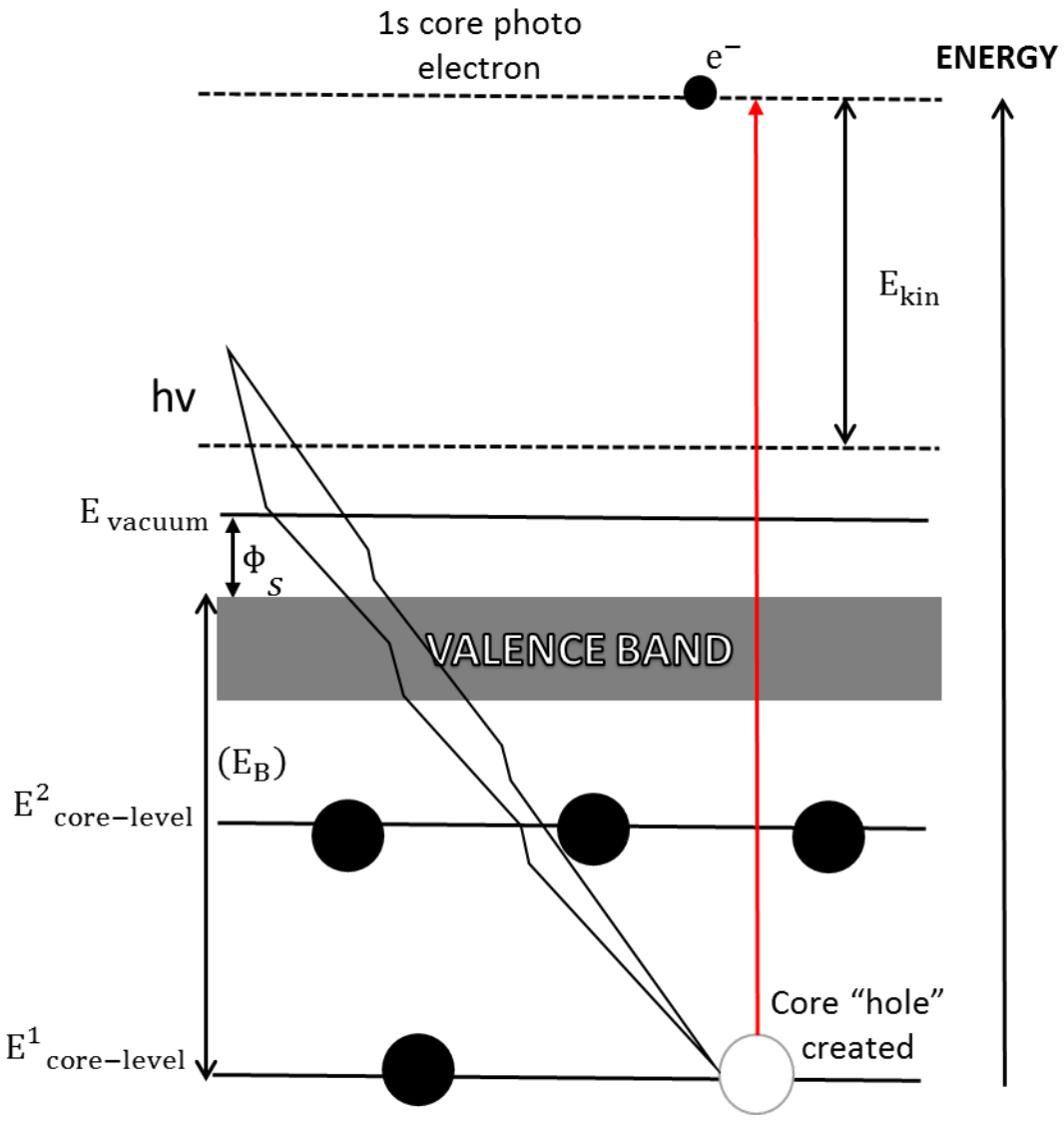

Figure 2.1: Graphical summary of the photoemission process. The figure was based on reference. 13.

The XPS experiment involves exposing the species to be studied to a beam of nearly mono-energetic photons with mean energy *hv* and then observing the resultant emission of

photoelectrons. The resultant photoelectron has a certain binding energy (E_B) below the Fermi level (shown in figure 2.1) and its kinetic energy is given by the photoelectric equation:

$$E_k = hv - E_b = hv - (E_b + \emptyset_s) \qquad (2.1)$$

In which $\emptyset_S$ is the work function of the sample and E_b is the binding energy relative to the vacuum level. There are three rudimentary properties of characterizing each emitted photoelectron, the direction of emission with respect to the sample, the kinetic energy and the exciting energy. For certain special experiments the direction of the spin is also considered. These three properties bring about the two basic types of measurements that are possible with photoemission.

The first type of measurement is the number of photoelectrons as a function of kinetic energy. This measurement produces an electron energy spectrum or energy distribution curve (EDC). The measurement is usually carried out at a fixed angle relative to both the sample and photon source. The second type involves angle resolved measurements which can be related to the axes fixed with respect to the specimen or the photon propagation direction. The kinetic energy distribution needs to be determined at each and every angle of the several angles of emissions used. The last measurement has to do with spin polarization or spin distribution of the photoelectron intensity. The specimen has to be magnetically polarized by an external field. This then allows for photoelectrons with one of the two possible spin orientations to be emitted more than the other. The relative number of spin up and spin down photoelectrons is then measured.[11]

Photoelectron emission (kinetic energy distribution measurements) can be divided into two types of measurements. The first type is valence band photoemission spectroscopy which is shown in figure 2.1 by the blue arrow. This technique probes levels occupied by electrons with low binding energies (near the Fermi edge). Orbitals in this region are delocalized; this results in valence electrons interacting more. The second measurement type is known as core-level photoemission spectroscopy and is shown by the red arrow in figure 2.1. This technique probes more strongly bound electrons with high binding energies. In this region orbitals are localized therefore this technique reflects the surroundings of individual atoms.[13]

2.2.2 Basic components for XPS measurements

The basic components that are used in XPS experiments consist of a photon source, an electron analyzer, the specimen to be studied, and a detection and control system. Each of the components will be discussed in detail below. Nowadays there are commercial sources of complete XPS spectrometer systems with various designs for the above mentioned components.

i. Photon source

X-ray tubes contain a heated-filament cathode from which emitted electrons are accelerated towards a solid anode (which is usually water cooled) over a potential of ~5-20 kV. This electron bombardment of the anode results in holes in the inner energy levels which are then filled by electrons from high energy levels emitting x-rays in the process.[9,11] A thin x-ray transmitting window is used to separate the excitation region and the specimen. The commonly used anode materials are Mg, Al and in some rare cases Na and Si. Each of these second row elements produce an x-ray spectrum dominated by a very intense, unresolved $K\alpha_1$-$K\alpha_2$ doublet. These result from the transitions of the type $2_{p_{3/2}} \rightarrow 1s$ and $2_{p_{1/2}} \rightarrow 1s$ respectively. The mean energies of the x-rays produced range from 1041 eV for Na $K\alpha_{1,2}$ to 1739 eV for Si $K\alpha_{1,2,}$ with Mg (1253 eV) and Al (1486 eV) mean energies lying in between the range. At these energies beryllium and aluminium windows of 10-20 nm are sufficient for use as separator between the specimen and the tube. The utilization of these anodes in XPS studies was first demonstrated by Henke and later by Siegbahn and his co-workers in higher resolution applications. Usually more than one x-ray line is emitted by an anode material and the energy width associated with various lines also varies significantly from one element to another.[9,11] Additional radiation consists of a continuous background of bremsstrahlung and satellites from $2_{p_{3/2}} \rightarrow 1s$ and $2_{p_{1/2}} \rightarrow 1s$ transitions in atoms that can be doubly, triply ionized etc. So photoemission spectra from non-monochromatized sources always exhibit a characteristic double peak with KE ~ 10 eV above the x-ray source. Analysis has been usually based on photoelectrons produced from $K\alpha_{1,2}$ peaks. Additional satellite generated peaks are only taken into consideration in studies involving weak photoelectron peaks.[11] if necessary, spectral features due to x-ray satellites can be numerically subtracted from spectra.

Monochromatized x-rays have been explored in order to achieve narrower excitation sources, which are generated by using Bragg's reflection from single crystals. Photoelectron peaks as narrow as 0.4 eV for Al Kα have been observed compared to 0.9 eV for non-monochromatized

sources. This eliminates bremsstrahlung and satellite lines. There is a significant loss of intensity in these reflections which is compensated by using high intensity x-ray tubes involving rotating anodes, monochromator systems with more than one anode and multichannel detector systems.[11]

ii. Specimen preparation

XPS spectra can be obtained from species in gaseous, liquid and solid form. Two factors are considered when preparing or handling the sample. The first factor is the pressure between the detector and the specimen must be $\leq 10^{-4}$ torr, so as to avoid excessive inelastic scattering during photoelectron traversal through the energy analyzer. The vacuum in the electron analyzer itself must be significantly higher, due to the high voltages that are present.[9] The second factor is the need to minimize or correct the positive potential build-up in the emitting region when insulating or poorly conducting samples are measured. This is due to loss of negative charge during the emission of photo-Auger and secondary electrons from the specimen. This can be achieved by a flux of low energy electrons emitted towards the specimen from a dedicated electron source. This may also lead to the opposite effect, a build-up of negative charge in the emitting region.[9, 11]

A net imbalance between input and output charge produces a charge potential V_c which varies throughout the specimen volume. This may result in an energy level shift from values consistent with situations where charging does not occur. Therefore if **r**, is defined as the spatial coordinate of the emission point within the specimen volume, and ${E_b}^v(k)^o$ and ${E_{kin}}^o$ are the binding energy and kinetic energy expected from emission from level k^o in the absence of charging respectively. Then the photoelectric equation can be rewritten as:

$$\begin{aligned} h\nu &= {E_b}^V(k,\boldsymbol{r}) + E_{kin}(\boldsymbol{r}) \\ &= {E_b}^v(k)^o + {E_{kin}}^o + V_c(\boldsymbol{r}) \end{aligned} \qquad (2.2)$$

If there is a significant difference between $V_c(\boldsymbol{r})$ and the typical instrumental resolution of ~ 0.1 eV (which can indeed occur in some instances) the measured binding energy ${E_b}^V(k,\boldsymbol{r})$ will be different from ${E_b}^v(k)^o$ and may result in peak broadening. Such effects can be minimized or corrected by carrying out studies on peak position versus x-ray flux. For solid specimens an electrical connection is made to the spectrometer as an attempt to minimize charging as well as to maintain a well-defined and fixed potential during photoemission.[11]

There are various ways of preparing solid specimens suitable for XPS studies and they are generally have an area of about 1 cm^2 or smaller. Machineable solids such as single crystals can be cut or cleaved into suitable shapes for mounting. The surface sensitivity of XPS requires the specimen region to be at pressures $\leq 10^{-9}$ torr so that the surface composition can be adequately controlled.[11]

iii. Electron energy analyzer

For the electron analyzer we will only look at the features relevant to XPS studies. In essence an electron analyzer should satisfy certain criteria. The analyzer ideally should have a resolution capability of $\Delta E_{kin}/E_{kin}$ ~ 0.01 % equivalent to 0.1 eV for 1000 eV electrons. Currently XPS spectrometers operate in the range of 0.01 to 0.10 %. The highest efficiency possible, which is the highest possible fraction of electrons leaving the sample that should be analyzed and detected, must be attained. There should be an unlimited physical access to the detection and sample region. This permits the use of various excitation sources, specimen geometries and detection systems. Last but not least the analyzer must be shielded from extraneous magnetic and electric fields. Electron analyzers have different designs but hemispherically shapes as shown in figure 2.2 are the commonly used ones.[11]

iv. Detection and control

Currently used detectors in XPS studies are based on continuous-dynode electron multipliers of the "channeltron" type. They consist of fine-bore lead doped glass tubes treated with hydrogen reduction at high temperature in order to leave the surface coated with a semiconducting material with high secondary electron emission power. The diameter of the inner tube varies from 1 mm down to 1 μm. A voltage of a few kV is applied to the ends of this tube and then a multiplication of the order of 10^6 to 10^8 is achieved by repeated collisions of electrons travelling inside the tube with the walls. Multipliers come in different configurations usually curved so as to minimize ion induced after-pulsing.

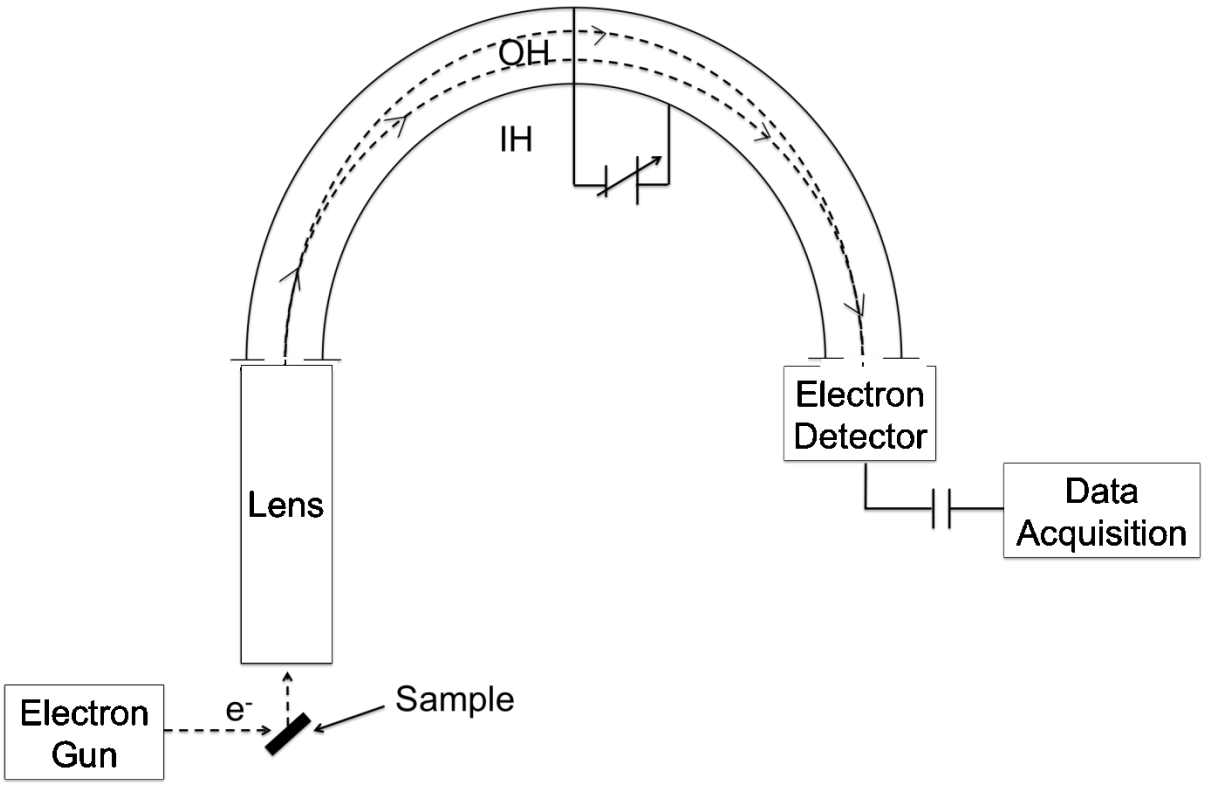

Figure 2.2: Schematic of an XPS spectrometer system illustrating the radiation source, electron energy analyzer, sample and detector. A hemispheric electron analyzer is used for the specific example shown here. The abbreviations OH and IH stand for outer and inner hemisphere respectively.

The schematic of the basic components discussed above is shown in figure 2.2. The figure illustrates the electron gun which produces electrons, the sample, lens which is used to focus incoming photoelectrons for increased number of electrons detected. A potential difference is applied to this analyzer as shown in figure 2.2 so that electrons with a small energy range difference can reach the detector. Then the detected information will transferred to the data acquisition system.

2.3 Temperature programmed adsorption (TPD)

The concept of the temperature programmed desorption technique is straightforward. It is a powerful technique based on studying desorption of molecules from a surface which is the most

fundamental and elementary surface kinetic process. This analysis can also be carried out under UHV conditions, as a large number of TPD experiments can be carried out at atmospheric pressures as well. The process involves exposing the surface in study to gaseous molecules. Exposure can be carried out in various ways but the commonly used method is backfilling the chamber with gaseous molecules to some predetermined pressure for a certain period of time (measured). Upon contact with the surface the molecules minimize their energy by adsorbing to the surface through physisorption, chemisorption or the formation of chemical bonds with the surface.[9] The surface temperature is then increased in a linear manner which gives adsorbed molecules enough energy to desorb from the surface. This results in an increase of partial pressures of the desorbing molecules which is measured using a mass spectrometer which detects the mass to charge ratio of the molecules.[14]

The following information is obtained from the TPD spectrum (which is partial pressure against temperature), the area under the peak is equivalent to the amount of the species or mass fragment that was adsorbed initially, and thus it gives information about the surface coverage.[15] The state of aggregation (molecular and dissociative) of the adsorbed species is obtained from the kinetics of desorption which in turn are obtained from the coverage dependence of desorption characteristics and the peak profile.[15] The enthalpy of adsorption is obtained from the peak position and it gives information on the strength of the bond between the surface and the adsorbate molecules. Thus TPD compliments other surface techniques and provides essential information such as surface kinetics and adsorption enthalpies.[14]

2.3.1 Basic experimental requirements

There are three basic requirements for performing TPD analysis, the heating system, method of monitoring temperature and a detector for monitoring the desorption of molecules from the surface.

i. Heating system

The first experimental requirement to perform TPD analysis is a method of heating in such a way that the equation below is obeyed i.e., that the heating rate is constant,

$$T(t) = T_o + \beta t \qquad (2.3)$$

where β is the heating rate, t the time, T_o initial sample temperature and $T(t)$ is the temperature at a given time period. Ideally the heating should be restricted to the sample only so as to avoid desorption from other surfaces such as the sample holder. This is achieved by employing the "resistive heating" method. In this method a wire is fixed to the edges of the sample and then current is passed through these wires so as to heat the sample by conduction.[9]

ii. Monitoring temperature

The temperature is monitored by spot-welding a thermocouple to the sample.

iii. Monitoring the desorbing molecules.

A quadrupole mass spectrometer is the commonly used type of spectrometer for TPD analysis mainly because it makes it easy to obtain direct information due to its sensitivity to the mass of measured molecules. During the analysis it is tuned to the mass of the desorbing molecules and is positioned close to the surface.

2.3.2 Basic principles

The main application of TPD is in measuring the kinetics of surface processes. Generally the heating rate in TPD analysis ranges from 1 to 100 $\mathrm{K.\,s^{-1}}$.[9] The most difficult part of TPD experiments is ensure that the molecules detected by the mass spectrometer are from the surface only. Some of these methods put in place to achieve this are the resistive heating and close positioning of the mass spectrometer. Another one is fitting a glass aperture on the ionization region of the mass spectrometer. If the glass aperture is not in place a "support" peak is observed at the beginning of the TPD measurement which is a consequence of the rapid desorption from the heating wires because it heats up faster than the sample.[14]

Increasing the surface temperature gives molecules sufficient thermal energy to break surface interactions and initiate desorption. Only one peak will be observed for a simple case where the activation energy for desorption is constant as a function of coverage for a certain adsorbate. The maximum temperature (T_P) and maximum desorption rate are related because the experiments are carried out in UHV which is being continually pumped. This may seem odd since desorption is an activated process with a rate constant (K_d) that obeys the Arrhenius dependency and should increase with temperature as in the equation below:

$$k_d = Ae^{\left(\frac{-Ed}{RT}\right)} \qquad (2.4)$$

where A is a pre-exponential factor and E_d is the activation energy of desorption.[16] The temperature according to equation 2.4 increases linearly but a maximum is reached since the temperature increased is coupled with a decrease in surface coverage. Therefore the observed desorption kinetics in TPD experiments are convolutions of these two factors. It is common practice to take TPD spectra in order of increasing coverage so that analysis may give information about relative coverage, strength of lateral adsorbate interactions and energy of desorption. The rate of desorption is given by the following relationship:

$$\frac{-dN}{dt} = k_d N^m \qquad (2.5)$$

where N is the number of adsorbed species, k_d is the rate constant for the desorption process and *m* is the order of the reaction.[16] After simplification the following equation results

$$\frac{dN}{dt} = \frac{dN}{dT} \times \frac{dT}{dt} = \frac{dN}{dT}\beta \qquad (2.6)$$

where $\beta = \frac{dT}{dt}$ is the heating rate. Thus equation 2.5 can be rewritten as:

$$\frac{-dN}{dt} = \frac{k_d}{\beta} N^m$$

and then substituting for k_d from equation 2.4:

$$\frac{-dN}{dt} = N^m \frac{A}{\beta} exp\left(\frac{-E_d}{RT}\right) \qquad (2.7)$$

For a case where $T = T_P$ (the thermal desorption peak) and

$$\frac{d^2N}{dT^2} = 0 \text{ (the rate desorption reaches a maximum)} \quad (2.8)$$

Therefore differentiating equation 2.7 with respect to *T* and equating to zero results in a general expression that relates T_P, E_d and N.

$$\frac{E_d}{RT_P{}^2} = \frac{A}{\beta} m N^{m-1} exp\left(\frac{-E_d}{RT_P}\right) \qquad (2.9)$$

For m = 1 (first-order desorption) the equation becomes:

$$\frac{E_d}{RT_P{}^2} = \frac{A}{\beta} exp\left(\frac{-E_d}{RT_P}\right) \qquad (2.10)$$

Since both β and T_p are experimentally measurable variables this allows for E_d to be evaluated as long as the pre-exponential factor A is known.[16] The pre-exponential factor for a first-order desorption reaction is assumed to be of the same order as the molecular vibrational frequency which is approximated to be $10^{13} s^{-1}$.[27] The evaluation of E_d is carried out using a trial and error method by initially guessing the value then iteratively refining it until the equality in equation 2.10 is satisfied. However there is a modified version of equation 2.10 that has been shown to be accurate for m = 1 and A/β between 10^8 and 10^{13} K^{-1}.

$$E_d = RT_P \left[\ln\left(\frac{AT_P}{\beta}\right) - 3.46\right] \qquad (2.11)$$

From equations 2.10 and 2.11 it is evident that the desorption peak is independent of the adsorbate coverage (the N term is absent).[9] The desorption peak maximum only increases in intensity with an increase in coverage but remains at a constant temperature. It is important to note that the above analysis takes into consideration certain assumptions. These assumptions include activation energy and pre-exponential factor being independent of coverage and that desorption occurs in a single step. For systems with complex reaction mechanisms the above equation would not hold and will result in an incorrect value of E_d.

In terms of the second-order desorption reactions where m = 2, equation 2.9 results in the following equation.

$$\frac{E_d}{RT_P{}^2} = \frac{2AN}{\beta} exp\left(\frac{-E_d}{RT_P}\right) \qquad (2.12)$$

From equation 2.12 it is evident that second-order desorption reactions are dependent on the coverages. Coverage (N) increases with a decrease in T_p for a fixed value of E_d. These desorption reactions are characterized by a shift of T_p to lower temperatures as function of increasing temperature but the peaks remain symmetrical. It is not the case for first-order desorption reactions peaks which are asymmetrical.[14]

For atomic adsorbates and simple molecular layers (e.g. CO on Ir(100) surface) where molecules do not interact strongly and the adsorption is intact, first order desorption kinetics are observed.[17]

Second order desorption is however observed for recombinative desorption processes (e.g. desorption of N atoms as N_2 from Ir(100) surface).[9,16] Multilayer systems usually obey zeroth order desorption kinetics. The maximum desorption temperature of zero order processes shifts to high temperature with an increase in coverage (thickness of the multilayer) without reaching saturation and the peaks are asymmetrical.[14]. The thermal desorption spectrum of multilayer systems consist of low temperature desorption peaks as a result of weakly bonded layers subsequent to the chemisorbed first layer.[9,16]

Chapter 3

Low Energy Electron Diffraction (LEED)

LEED is one of the oldest but most effective surface science techniques. The development of this technique is a consequence of atomic physics and quantum theory. There are two events that contributed to the development of LEED: the discovery of the electron beam by measuring the ratio of charge to electron mass by J.J Thompson in 1897 and the first LEED experiment performed by Davisson and Germer in 1927 using a Ni crystal and explained as diffraction from a crystallite.[18,19]

3.1.1 Basic Principles

LEED is a surface technique that uses a monochromatic electron beam with an energy that can be varied from 20 –1000 eV produced using an electron gun. These electrons then undergo diffraction from a sample, and the elastically backscattered (without energy loss) electrons are analyzed. The range (20 –500 eV) of these electrons gives them a characteristic inelastic mean free path (IMFP) of approximately 5 -14 Å, therefore they can only penetrate a few layers of the surface.[9] Another reason why they make good surface probes is because they possess de Broglie wavelength which is of the same order of magnitude as the interatomic spacing between atoms or molecules of the surface.[9] Thus they easily undergo diffraction if the surface atoms are arranged periodically. Figure 3.1 illustrates the conventional LEED apparatus used to perform experiments. The electron gun generates monochromatic electron beam in the range of 20 to 1000 eV which is then incident on the sample (electrical conductor) that is connected to ground to prevent charging. These incident electrons then undergo diffraction on the sample surface and are backscattered towards a series of concentric grids (Grid 1 to Grid 4 shown in figure 1). Grid 1 and 4 are earthed for different purposes. Grid 1 is the nearest and thus is earthed so as to ensure electrons travel in a “field free” region and grid 4 is earthed so that it screens out the high voltage from the phosphor screen. Grid 2 and 3 act as cut-off filters and they are held at a negative potential to ensure that only elastically scattered electrons reach the detector. The detector or

screen is held at a high voltage so that transmitted electrons can be accelerated to enough kinetic energy that will cause light emission from the coated fluorescent screen.

The light emitted from the screen is seen as a pattern of bright spots on a dark background, known as the LEED pattern. These LEED patterns can be viewed by eyes or with a video camera for quantitative studies. The LEED pattern represents the symmetry and crystalline order of the surface, the information that can be extracted from it is the long range structure of the surface, size of the unit cell (periodicity) and island size (from the spot profile).[15] Both qualitative and quantitative information can be obtained from LEED experiments.

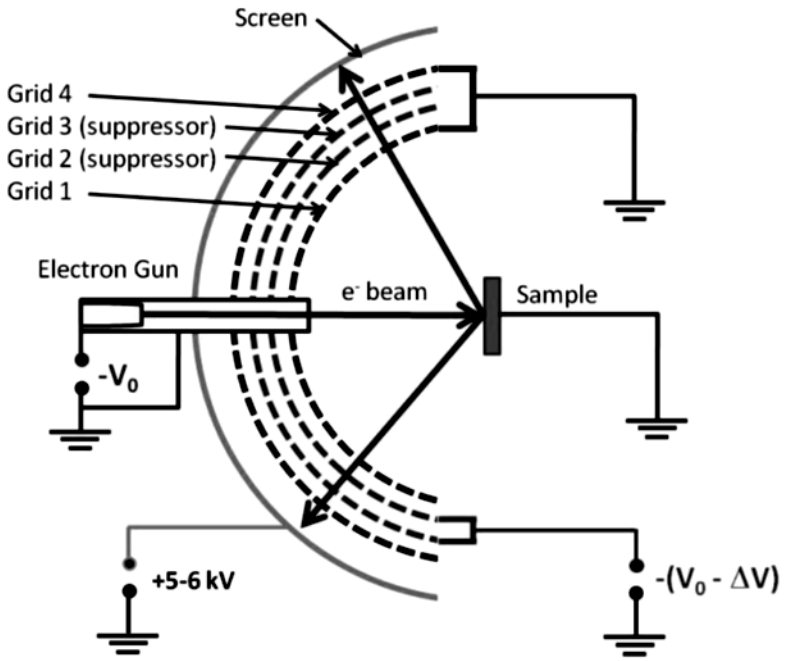

Figure 3.1: Schematic of a conventional LEED system. The figure was reproduced from reference 20.[20]

The superposition of the interference patterns of each individual particle results in a diffraction pattern in diffraction experiments. The interference patterns of real instruments are not all perfectly the same because they exhibit energy and angular spread.[19] This results to an instrumental broadening of the diffraction spots. The transfer width is the measure of this broadening effect.[21] It describes the length on a surface which would lead to the instrumental width of the diffraction spots. For a typical display type LEED instrument the coherence length

provided by the electron gun is of the order of 100 Å. Thus the domain size that can be analyzed is limited to about 100 Å (per dimension) by the instrument.[21] In addition the finite size of a coherently scattering object for example the finite size of a well ordered surface pattern can further broaden the spots. Therefore the analysis of spot width can be used to determine the size of ordered domains or islands.[19]

LEED patterns give qualitative information whereas quantitative information can be obtained by recording intensities of various diffracted spots as a function of the incident electron beam energy to produce the so called I-V curves (spot intensity vs kinetic energy).[9] The I-V curves provide accurate information on the position of atoms inside the unit cell (surface geometry), including the bond lengths and angles.[12]

3.1.2 The LEED pattern

The periodicity and the degree of order of the surface is the most direct information that can be obtained from LEED experiments. The information obtained from the analysis of the spot positions is the size, symmetry and rotational alignment of the substrate unit cell (and that of the adsorbate when present on the surface). A primitive unit cell is used to describe an ordered surface which is the simplest repeating unit. The whole array of the substrate can be constructed by repeated translation of the unit cell. Since low energy electrons do not penetrate into the bulk to experience 3-D periodicity the diffraction pattern is therefore determined using the lattice vectors $\overrightarrow{a_1}$ and $\overrightarrow{a_2}$. The reciprocal lattice vectors $\overrightarrow{a_1^*}$ and $\overrightarrow{a_2^*}$ are then defined using the 2-D Bragg's condition and they fulfill the following equations:

$$\overrightarrow{a_1^*} \cdot \overrightarrow{a_1} = \overrightarrow{a_2^*} \cdot \overrightarrow{a_2} = 2\pi \qquad (3.1)$$

$$\overrightarrow{a_1^*} \cdot \overrightarrow{a_2} = \overrightarrow{a_2^*} \cdot \overrightarrow{a_1} = 0 \qquad (3.2)$$

The sum integer multiples of $\overrightarrow{a_1^*}$ and $\overrightarrow{a_2^*}$ correspond to each diffraction spot in the pattern and the integers n_1 and n_2 are used to label the spots on the diffraction pattern.

$$n_1 \overrightarrow{a_1^*} + n_2 \overrightarrow{a_2^*} \qquad (3.3)$$

For a case where there are reconstructions or adsorbates on the surface a different periodicity is observed. This results in additional spots (superstructure) in the LEED pattern. Lattice vectors $\overrightarrow{b_1}$ and $\overrightarrow{b_2}$ are then used to define the superstructure (overlayer). These two vectors are defined as:

$$\overrightarrow{b_1} = m_{11}\overrightarrow{a_1} + m_{12}\overrightarrow{a_2}$$

$$\overrightarrow{b_2} = m_{21}\overrightarrow{a_1} + m_{22}\overrightarrow{a_2} \qquad (3.4)$$

where *m* is an integer.

The position and the indices of these additional spots can be calculated using the following formulae:

$$\overrightarrow{b_1^*} = (m_{11}m_{22} - m_{12}m_{21})^{-1}\left(m_{22}\overrightarrow{a_1^*} - m_{21}\overrightarrow{a_2^*}\right)$$

$$\overrightarrow{b_2^*} = (m_{11}m_{22} - m_{12}m_{21})^{-1}\left(m_{12}\overrightarrow{a_1^*} - m_{11}\overrightarrow{a_2^*}\right) \qquad (3.5)$$

There are two methods used to describe the periodicity of adsorbates or superstructures on the surface. These methods are known as the Woods and the matrix notation. The Woods notation is most suited for commensurate structures and it relates the overlayer structure to the substrate. The equation below describes the Woods notation in details.

$$M\ (hkl)\ \left(\frac{|b_1|}{|a_1|} \times \frac{|b_2|}{|a_2|}\right) - R\alpha - A \qquad (3.6)$$

where M is the chemical symbol of the substrate, (hkl) are the miller indices of the surface, $|b_1|$ and $|b_2|$ are the magnitudes of the surface overlayer net vectors, $|a_1|$ and $|a_2|$ are the magnitude of the substrate net vectors, α is the angle in degrees between the substrate and overlayer structure meshes (omitted if equal to zero) and A is the chemical symbol of the surface species.

The "matrix" notation, which is a more general method, is used to describe both commensurate and incommensurate overlayer structures. The initial step of the matrix notation involves defining the primitive vectors (b_1 and b_2) for the superstructure in terms of the linear combination of the primitive unit mesh vectors of the substrate (a_1 and a_2). The matrix notation defines the overlayer structure in terms of the substrate. In general the matrix notation is defined as:

$$b_1 = G_{11}a_1 + G_{12}a_2 \text{ and } b_2 = G_{21}a_1 + G_{22}a_2$$

$$\text{Hence } \begin{pmatrix} b_1 \\ b_2 \end{pmatrix} = \begin{pmatrix} G_{11} & G_{12} \\ G_{21} & G_{22} \end{pmatrix} \begin{pmatrix} a_1 \\ a_2 \end{pmatrix} \qquad (3.7)$$

and the matrix G defines the structure of the adsorbate, where G_{11}, G_{12}, G_{21} and G_{22} are constants. The determinant of the matrix G gives the coverages of the adsorbate,

$$\det G = [(G_{22}.G_{11}) - (G_{21}.G_{12})] \qquad (3.8)$$

3.2 CLEED program

3.2.1 Introduction

The CLEED (Cambridge Low Energy Electron Diffraction) program was written by G. Held in 1994 at Cambridge in United Kingdom. At that time the available LEED codes were FORTRAN based and they did not permit dynamical memory allocation. This meant the code had to be re-compiled and edited for every new surface structure studied. This made LEED calculations a tedious process. The main aim was to develop a program that will be user friendly, and could handle most single crystal surface structures without having to re-compile, and would determine most non-geometrical parameters such as beams to be used in calculations and distribution of atoms into layers. Thus the program will reduce the input to more or less only the surface geometry. The CLEED code was written based on the well-established layer doubling and combined space methods by Pendry[19] and Van Hove and Tong [22] respectively. The name initially came from the fact that the C programming language was used to write the code but has then later changed to Cambridge LEED.

3.2.2 Description of the CLEED program

There are different programs which can perform LEED calculations, and they all differ by theoretical methods used and the physical effects that are included at the interfaces. The CLEED program contains the full dynamical scattering theory implemented using algorithms developed by Pendry (layer doubling between atomic layers)[19] and van Hove and Tong (combined space method for layers with more than one atom per unit cell)[22,23] as mentioned above. The combined space method divides the layers of a crystal into groups. Wave functions are then used to

represent these different groups. Spherical wave representation is used to solve layers which have small interlayer distances with their neighbours and these form a group. The resulting waves of each group are then transformed into a plane wave representation. The multiple scattering between the groups and the other layers are solved with plane waves. This scheme is useful when for example; an overlayer is very close to the top substrate layer. The computation time of the plane wave representation method increases with decreasing the interlayer spacing and also convergence problems can be encountered.

The CLEED package consists of different programs that interact with each other during a structure calculation process. Figure 3.2 illustrates a general iteration process used in the CLEED package. There is a program (**cleed_nsym)** that calculates theoretical I-V curves and another program (**crfac**) evaluates the agreement of these theoretical I-V curves with the experimental I-V curves and then gives the results in terms of a reliability factor (R-factor) which is used to quantify the agreement between theoretical and experimental data. The R-factor is optimized through the variation of geometrical parameters and angles of incidence using a local search algorithm, (simplex algorithm).

The **csearch** program performs the structure optimization and it calls the **cleed_nsym** program within each step. It uses standard optimization algorithms such as the downhill simplex method, Powell's method, simulated annealing and the genetic algorithm which can be selected by the user in order to perform the search for the best fit geometry. While the first two algorithms are strictly downhill-oriented, i.e. will find only the nearest local R-factor minimum, the latter two algorithms should in principle provide a means of locating the global R-factor minimum within the given constraints, at the expense of many more search steps. Within each search step a set of geometrical parameters is chosen by the algorithm depending on the R-factor values achieved before and in accordance with user-specified symmetry constraints. The parameters are written to a file serving as an input for the LEED program whose output is then fed into the R-factor program in order to calculate an R-factor value for this parameter set.[20] The **cleed_nsym**

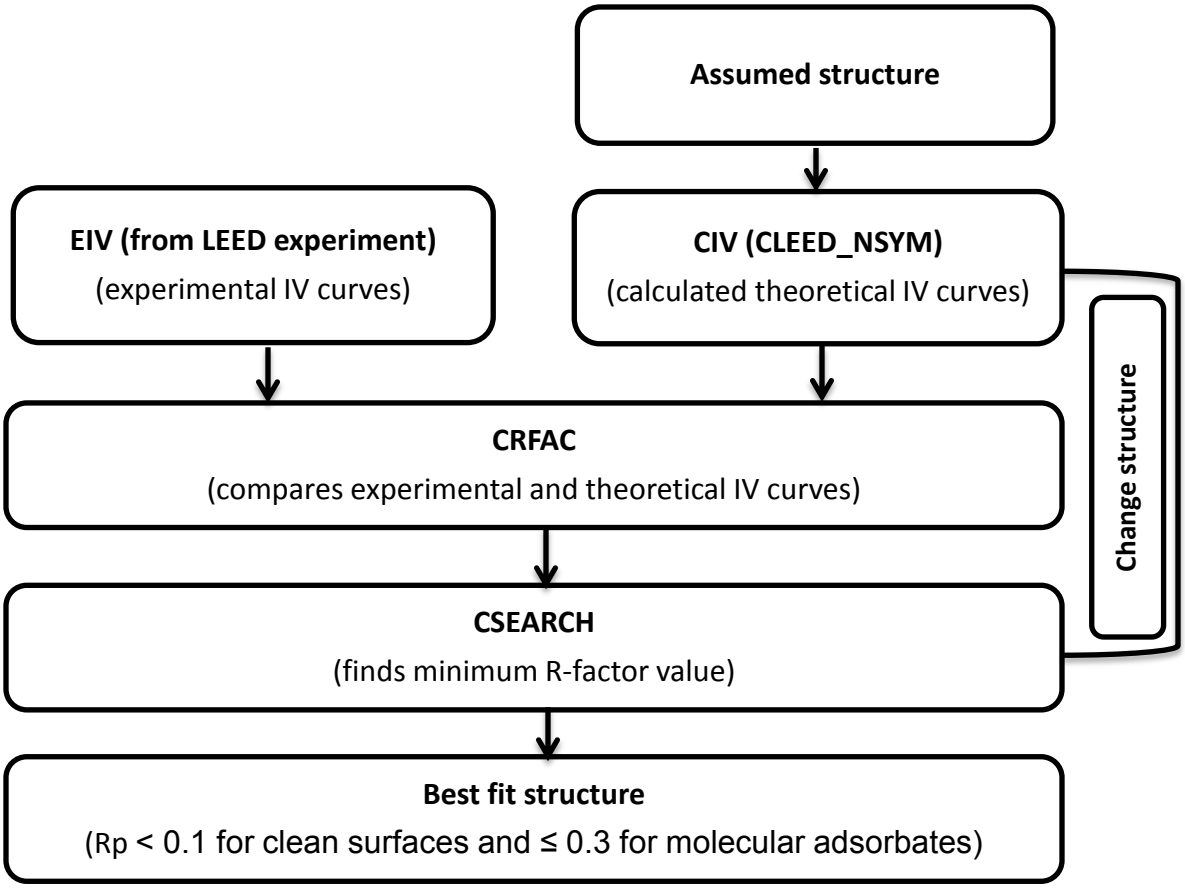

Figure 3.2: The iteration process used in the CLEED package to solve the surface crystal structure.

program calculates the theoretical I-V curves as mentioned before and then **crfac** program gives the results in terms of an R-factor for the calculated I-V curves as shown in figure 3.2. For each iteration, the geometrical parameters are chosen by the algorithm based on the previous R-factor values. At the end of the calculation **csearch** finds the minimum R-factor value as a function of the geometrical parameters optimized. The global search algorithms have not been tested sufficiently to be used indiscriminately in CLEED.

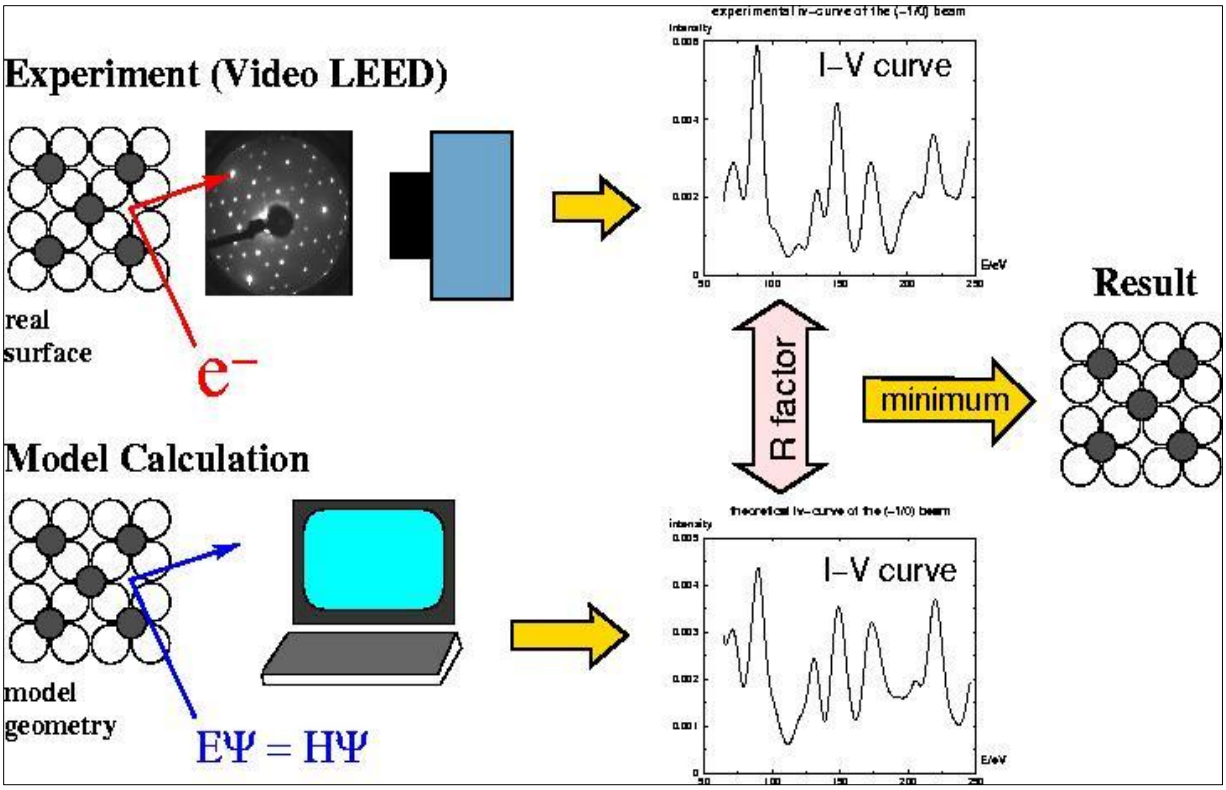

Figure 3.3: Schematic illustrating the "trial and error" method used in CLEED structural determination calculation. Figure reproduced from reference 24.[24]

Figure 3.3 gives the complete general process of CLEED calculations. LEED experiments are carried out, a LEED pattern is observed and then I-V curves are extracted. This is the experimental data that is then used. From the LEED pattern observed, a geometry is modelled using symmetry constraints from the LEED pattern and any additional information from other techniques. This is then fed to the CLEED program which does a search and outputs a best fit structure for that model. The best fit structure is then optimized by changing geometrical parameters. The Pendry's reliability factor is then used to quantify the comparison between the experimental and theoretical data. The model structure with the lowest R-factor means it fits the experimental data better therefore the structure has been solved.

3.2.3 Accuracy of the structure determination

As discussed a reliability factor is used to quantify the agreement between the experimentally and theoretically calculated I-V curves. The numerical results of this quantification are known as the R-factor. The reliability increases with a decrease in the R-factor value. There are several R-factors used for LEED calculations, the CLEED package uses the most commonly used factor which is the Pendry's factor (R_p). It is defined by the following equation:

$$R_P = \frac{\int (\gamma_e - \gamma_{th})^2 \, dE}{\int (\gamma_e^2 - \gamma_{th}^2) \, dE}$$

where γ is defined by:

$$\gamma_e = \frac{L}{1 + V_{oi}^2 L^2}$$

V_{oi} is the optical potential which is the imaginary part of inner potential in the order of 4 to 5 eV and L is the logarithmic derivative of I(E) (where I is the intensity) with respect to the energy, divided by I(E)

$$L = \frac{I'(E)}{I(E)}$$

Thus the R-factor is more sensitive to the shape of the I-V curves rather than their intensities. The R-factor has minimum and maximum values 0 and 2 respectively, where a value of 0 indicates perfect agreement and 2 perfect anti-correlations. For clean surfaces with lower miller indices values of 0.1 and for adsorbate covered surfaces values around between 0.2 and 0.3 represent a good agreement between theory and experiments.[19,18] In order to quantify the reliability of the R-factor the RR-factor is used:

$$RR = \sqrt{\frac{8V_{oi}}{\Delta E}}$$

Therefore the R-factor is well represented as: $R_P \pm R_P \times RR$.

3.3 CLEED modification

3.3.1 Multiple domains

The symmetry of the LEED experiment also includes the incoming electron beam. Therefore, off-normal incidence breaks the symmetry in most cases, except when the beam is exactly within a mirror plane. As a consequence, separate I-V calculations need to be performed for each rotation and/or mirror domain. A program was developed to consider the existence of multiple domains on the surface. It takes into account the number of the domains and calculates the I-V curves for each domain and averages them if they overlap in the reciprocal space. The new program created is called **c_dom** and it calls the **cleed_nsym** program for each domain. The program **c_dom** performs the appropriate number of I-V calculations and mixes the I-V curves of overlapping spots as necessary. For this purpose, the substrate symmetry has to be provided in through one of the input file known as the bulk file.

The actual programs used by **csearch** for calculating the I-V curves and the R-factor are specified through the environment variables and the addition of extra environmental variables makes it easy to expand the search to surfaces where multiple domains are present. The environment variable **CDOM LEED** specifies the program which is used to calculate the I-V curves for a multiple domains. The only extra input required for **c_dom**, in addition to the input for **cleed_nsym**, is the symmetry of the substrate. More precisely, we need to specify the two domains that generate new domains on the surface.

The **c_dom** program then generates a number of intermediate output _files:

<sifiso>.bul.d1, <project>.bul.d2, ... (one for each domain),

<sifiso>.res.d1, <project>.res.d2, ... (one for each domain),

<sifiso>.res.tmp, and

<sifiso>.res.out (containing the control output of the current LEED calculation).

The only output _file used by **csearch** is <sifiso>.res, which contains correctly averaged I-V curves of the spots of all domains generated by the specified symmetry operations in the input file.

3.4 CLEED calculations: NO adsorbed on Ir{100} and D-serine adsorbed on Cu{110}

The LEED experimental data (I-V curves) for the two system considered in this dissertation, NO on Ir{100} and D-serine on Cu{110} were obtained from the University of Cambridge and University of Reading respectively. The LEED experiment for NO on Ir{100} was carried out at a temperature of 200 K and 14 I-V curves each corresponding to spots of a (2×2) pattern were extracted with a cumulative energy range of 2262 eV (total energy of all the I-V curves extracted). The LEED pattern observed on the screen was $\mathrm{p}(2 \times 2)$.

The LEED experiment for the d-serine on Cu{110} system was carried out for two coverages 0.1 and 0.25 ML. The pattern that was obtained for both coverages was the same and is (-1 -2; 4 0). The unit cell of d-serine was made of 8 Cu atoms which doesn't share any symmetry with the substrate surface besides the 180 º rotation. The LEED calculations for the structure determination of the above mentioned systems are in chapter five and six respectively.

CHAPTER 4

4.1 Literature review

In heterogeneous catalysis, bond formation and breaking on the metal surface is essential. During the catalytic process, bond formation follows the adsorption of the gaseous molecules onto the surface of the metal. Thus, prior to the actual bond formation process, a complex interaction mechanism that involves the surface and the adsorbed molecules takes place, this involves attractive and repulsive forces. This complex mechanism can be explained using the potential energy surface (PES) model which summarizes the interactions between the surface atoms and the molecules.

4.1.1 Metal support interactions

The advantages of using supported metal catalysts have been long appreciated. The traditional way of constructing a metal support system in catalysis involves depositing the metal particles on a support material to increase surface area and thus enhancing reactivity. For a long period of time, supports were thought to be catalytically inert except for special cases such as in the bi-functional platinum-alumina catalysts used for petroleum reforming.[25] It was then discovered that, for some systems, the interaction between the support and the metal particles affects the properties of the metal particles such as the adsorption of CO or H_2 onto the surface.[26] This has been notably tested for platinum supported on titania (Pt/TiO_2), where it was shown that the introduction of metal-support interactions via a high temperature calcination step resulted in a decrease in the heat of adsorption of CO and H_2.[27] The decrease in the heat of adsorption of CO led to an increase in the rate of methanation.[28] This effect has been attributed to strong metal support interactions (SMSI). This effect could not however be confirmed for a Pd/ TiO_2 system.[29] Strong metal-support interactions have been shown to exist in various systems where the metal is dispersed on an inorganic oxide surface. A prerequisite is that the latter should be a transition metal oxide which upon activation will form reduced cations that will be exposed to the metal particles. Manifestation of the SMSI properties includes a profound change in

chemisorption properties of CO and H_2, alteration of catalytic properties for certain reactions and the formation of unusual metal particle structures visible in electron microscopy.

It has been shown that SMSI catalysts suppress H_2 and CO chemisorption thus the logical thinking was that this will also suppress the CO-H_2 synthesis reaction activity. Surprisingly, studies involving supported catalysts showed that Ni/TiO_2 has tenfold greater activity compared to Ni/Al_2O_3, Ni/SiO_2 and Ni/C.[30] These comparison studies were made based on a per gram basis since chemisorption suppression of CO and H_2 on Ni/TiO_2 system made it difficult to use assessment of the relative nickel surface areas. In addition to that the supported catalyst (Ni/TiO_2) system has higher selectivity for formation of products of high molecular weight and minimizes the formation of nickel carbonyls.[30] Similar results were found for Pt and Pd metals. Initially, studies of the suppression of CO and H_2 chemisorption studies were carried out at ambient temperature. Further studies went on to confirm that even under Fischer-Tropsch (FT) reaction conditions (high temperature) these properties are maintained. FT is a process in which the synthesis gases, CO and H_2 are catalytically converted into hydrocarbons and oxygenates via surface polymerization.[31] This relation between chemisorption and catalytic activity seems paradoxical. It shows that a low uptake of an adsorbate on the surface, which implies short lifetime on the surface does not necessarily mean that the lifetime is not insufficient for adsorbed species to react.[30] Thus a weakened surface-adsorbate interaction may be beneficial for some catalytic processes. It follows that CO-H_2 synthesis reaction is inversely affected by the excessive heat of adsorption of CO and most catalytic systems possessing SMSI-induced properties show similarly improved catalytic properties for this reaction.[30]

The SMSI has been ascribed to the formation of interfacial bonds between the (reducible) oxidic support and the (noble) metal crystallite.[32] The chemical nature of these bonds has been elucidated, but has been hypothesized to resemble the structure of the surface silicates, aluminates or titanates, which can also be formed during the preparation of the catalyst.[33] However these species are mostly generated when preparing catalysts during the calcination and the reduction steps as shown for the Co/SiO_2 system.[34]

Molecular orbital calculations produced a precise model to explain the nature of the interaction between the formed cation and the supported metal. This model shows that there is a transfer of a whole or partial electron from the cation to the supported metal atom. This results in a strong ionic bond between the negatively charged supported metal atoms and the corresponding surface cations. XPS studies done on Rh/TiO_2 showed a reversible chemical shift (ΔE_B = -0.2 ± 0.05 eV) for the Rh $3d_{5/2}$ peak indicating an electron transfer from Ti^{3+} to Rh. This validates the results from the molecular orbital calculations.[35]

The interaction of the oxidic support material to the metal is typically investigated using different types of supports e.g. Co is deposited on different supports such as TiO_2, SiO_2 and Al_2O_3. Then the activity of the catalyst (on different supports) is compared.[36,37] This method may however lead to a various number of different variables affecting the performance of the catalytically active material. Hence model systems were developed using the reverse catalyst principle and this principle has been extensively applied in surface science experiments.[37] These model systems are comprised of nano-sized metal oxide crystallites, which are modified with alkoxy compounds (tetra-ethoxy silane, tri-isopropoxide aluminium or titanium butanate), which are subsequently activated in hydrogen.[38] The alkoxy compounds are introduced to induce species mimicking the metal-support interactions. It has been shown for samples modified with tetra-ethoxy silane that the metal support interactions remain intact after reduction of the metal and reactants. Furthermore, it was shown that the modification leads to a significantly enhanced hydrogenation activity of the catalyst which is thought to be induced by the weakening of the CO adsorption strength. However, the direct observation of the influence of the SMSI due to the local formation of Me-O-Si bonds could not be measured.[38]

4.1.2 Studies of CO adsorption on Co(0001)

Surface science has been extensively employed in studying the chemisorption of CO on cubic (fcc and bcc) transition metals in the past but relatively less work has been done on hexagonal metals such as Co and Ru regardless of their effective catalytic role in the reduction of CO by hydrogen.[39] Recent efforts have been focused on studying Co compared to other metal catalysts (Ni and Fe) used in FT synthesis. This shift in focus is a consequence of the superior activity,

higher chain growth probability and low water gas shift activity of Co compared to these other metals. However Co is expensive with a cost that is more than that of Fe, thus optimal design of the Co catalyst is crucial for the efficient use of this metal.[39]

In terms of CO adsorption, Co is considered to occupy a special place in the periodic table, which is in between the two well-studied metals Fe and Ni. These two metals Fe and Ni adsorb CO dissociatively and molecularly respectively at room temperature.[39] For Co the dissociative and non-dissociative properties depend mostly on the surface planes of the crystal used. On defect free surfaces such as Co(0001) and Co(1010) CO adsorbs molecularly, while on the more open surfaces such as Co(1120), Co(1012) and polycrystalline Co it adsorbs dissociatively. It was discovered that for open surfaces dissociation of CO occurs as a competing channel for desorption.[40,41,42]

The hexagonally closed packed (0001) surface of Co is similar to the fcc (111) surface which then allows direct comparison with corresponding fcc transition-metal surfaces.[39] There are several studies that have been done on the chemisorption of CO on Co(0001) single crystal surfaces and they illustrate the influence of surface structure on the reactivity of CO. These studies were motivated by the fact that the adsorption of CO on to the Co surface is an essential primary step for FT synthesis. Most studies on the Co(0001) surface are carried out at temperatures below 673 K which is the temperature for the Co surface phase transition from hcp to fcc.[43,44,45]

LEED studies on the clean Co(0001) surface showed ordered (1×1) diffraction pattern. The characteristic six-fold symmetry (with spots of the hexagon that have similar intensities) produced by an hcp (0001) was observed visually from the LEED pattern.[43] This then confirmed that the structure of the metal obtained at room temperature was indeed hcp. CO was found to adsorb molecularly on the Co(0001) surface and formed three ordered overlayer structures which occurred at three different coverages and adsorption temperatures.[43,46] These overlayer structures are: $\left(\sqrt{3} \times \sqrt{3}\right)$-R30º-CO, $\left(\sqrt{7/3} \times \sqrt{7/3}\right)$-R109º-CO and $\left(\sqrt{2/3} \times \sqrt{2/3}\right)$-R30º-7CO.[46,47] In the $\left(\sqrt{3} \times \sqrt{3}\right) - R30°$ overlayer CO was found to adsorb on the on-top site, with the CO upright bonding through C. This then resulted in buckling in the top layer of Co with the Co

atoms beneath CO pulled outwards by 0.04 Å.[48,44] Core level and valence band photoemission spectroscopy measurements were in agreement with this LEED study.[44,49]

The surface pressure (sp) isotherms of the Co-CO system at a temperature range of 286 to 447 K were studied. It was proven that the adsorption of CO on the Co(0001) surface was molecular and reversible above 350 K. This was accomplished using the adsorption isotherms which were completely reversible above 350 K. For example, when the pressure of CO is decreased to minimal values the surface potential of the clean surface is restored.[50] XPS was also employed in characterizing the adsorbates, and the spectrum was recorded 15 minutes after the CO exposure. The O 1s and C 1s peaks appeared at binding energies of 531.8 eV and 285.8 eV respectively and they implies that CO is adsorbed molecularly on the Co surface.[49]

A fascinating study using CO as a probe molecule to investigate metal-metal interactions was done on a bimetallic system that involved Co and Pt surfaces. In this study Pt was deposited on a Co(0001) surface and the coverage of Pt was deduced using the intensity ratio of the Pt 4f to the Co 2p peaks from XPS with the assumption that there is a layer-by-layer growth. Images of the sample obtained from a scanning tunneling microscope (STM) confirmed this.[50] The coverage of Pt was examined up to 0.6 ML and it was found to grow as a monolayer of thick islands. X-ray and Ultra Violet (UV) photoemission spectroscopy, LEED and STM were then used as the characterization techniques for this study. The clean Co(0001) surface gave a (1 × 1) LEED pattern, with a six-fold symmetry which is expected for the hcp (0001) plane. At low CO exposures and a Pt coverage of 0.25 ML a $\left(\sqrt{3} \times \sqrt{3}\right) -$R30º LEED pattern was observed. At high CO exposures observations were made using XPS only mainly because the LEED patterns were sensitive to electron irradiation. At these high CO exposures it was noted that the O 1s intensity increases with an increase in Pt coverage which implies that CO is absorbed on Pt areas. The peak was situated at the binding energy of 532.6 eV (compared to the normal value of 531.8 eV). It was concluded that the increase in O 1s binding energy means that CO is being adsorbed on Pt areas only. Most importantly the CO had a local coverage of up to 0.33 ML and the Pt-Pt distance decreased compared to that of Pt(111) in the Pt-Co(0001) system.[43] Importantly the observed changes in the electronic properties of Pt due to the shortening of the Pt-Pt distance resulted in the change of the reactivity properties of Pt on Co(0001). This therefore

resulted in a decrease in the adsorption energy of CO. Thus the bimetallic system influenced the reactivity of CO.[50]

4.2 UHV chamber commissioning

4.2.1 Introduction

The first proposition of experiments to produce vacuum was in 1631 by Reneri of Leiden and the first recorded experiment to produce vacuum was in 1641 by Gamparo Berti when he was doing experiments using the water barometer.[51,52] Several years after the initial experiments the first vacuum pumps were invented by Otto von Guericke and that was the birth of vacuum history. The development of vacuum technology continued. In 1658 and 1659 Robert Boyle and Robert Hooke designed and built an improved pump and used a mercury manometer in a bell jar to measure the pressure. Their pump managed to reach a pressure of 6 Torr and this made Boyle the first scientist to design a pump combined with a pressure gauge. The pump designed by Boyle was a piston pump.[52]

The pumping capabilities of the pump were improved over a period of approximately hundred years but the design was unchanged. Figure 4.1 shows the development time scale of various pumps and gauges from 1660 to 1900. From figure 4.1 the solid piston pump dominated from 1850 to 1858 and then it was replaced by liquid piston till 1900. The mercury manometer gauge also dominated until 1873 where it was replaced by the McLeod gauge.[51,52] It can be observed from the graph that there was less activity and change in pressure value in the period from 1660 to 1850 compared to the period from 1850 to 1900.[51] The latter period resulted in a significant improvement in vacuum pressure. Further improvements in the vacuum technology are shown in figure 4.2 which is from 1900 to 1950. These improvements were dominated by Gaede and Langmuir in Germany and the USA respectively.[51] Both the liquid piston pump and McLeod gauges were changed during this period. The diffusion pump and triode ionization gauge were built. From the shape of the graph in figure 4.2 it is evident that the development of vacuum technology was rapid from 1900 to 1920, which can be attributed to an increased demand from vacuum-tube electronics and television manufacturing industry.[1]

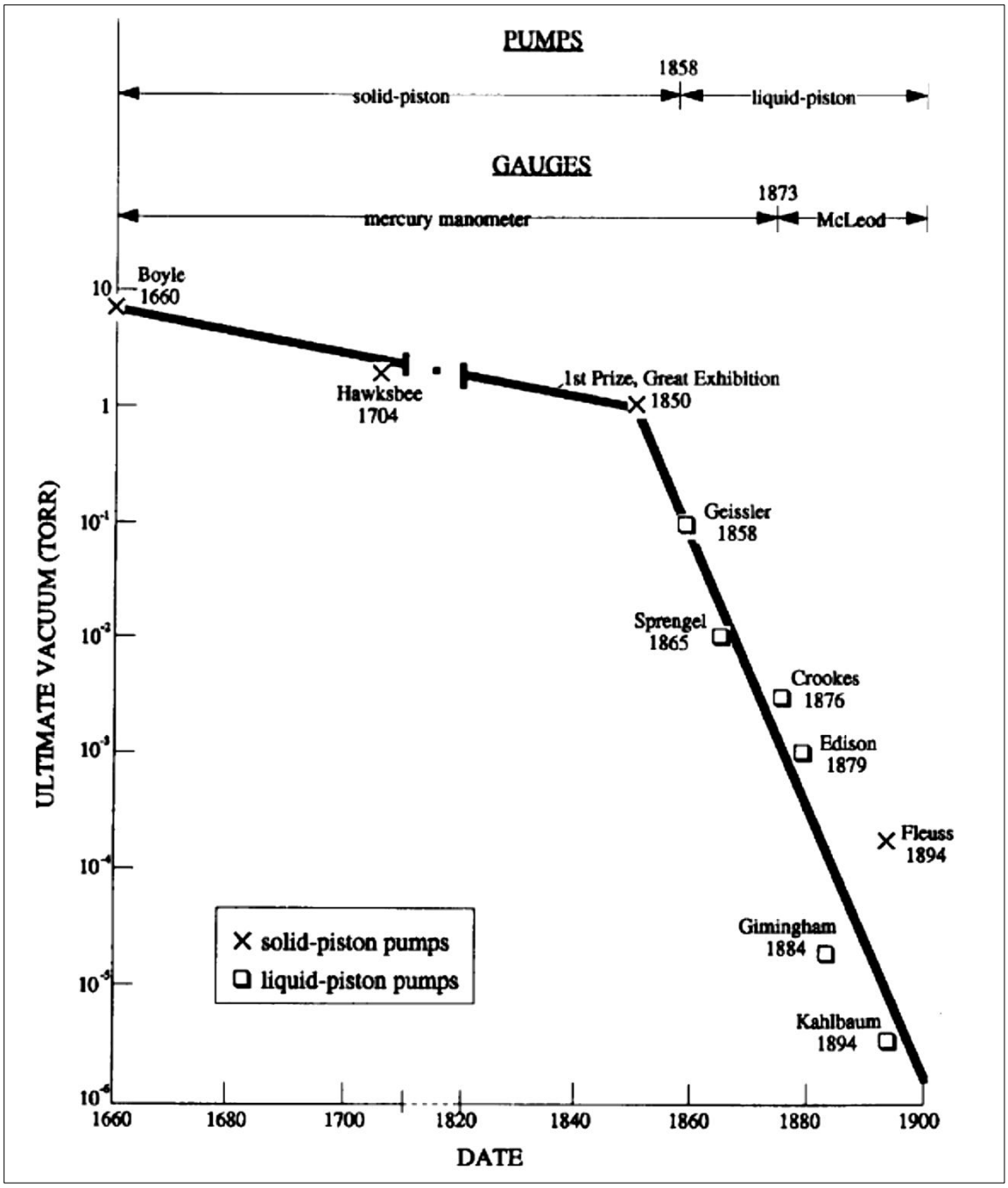

Figure 4.1: The vacuum development time scale from 1660 to 1900. Note that there is a break in the time scale. Figure reproduced from reference 51.

From 1920 to 1950 the vacuum pressure was limited to 10^{-8} Torr and it was assumed to be a failure of pumps rather than the gauges. It was later discovered that there was a limiting process in the gauges at lower pressures. By the late 1930's there was evidence that the hot cathode gauge failed to measure pressures below 10^{-8} Torr.[51]

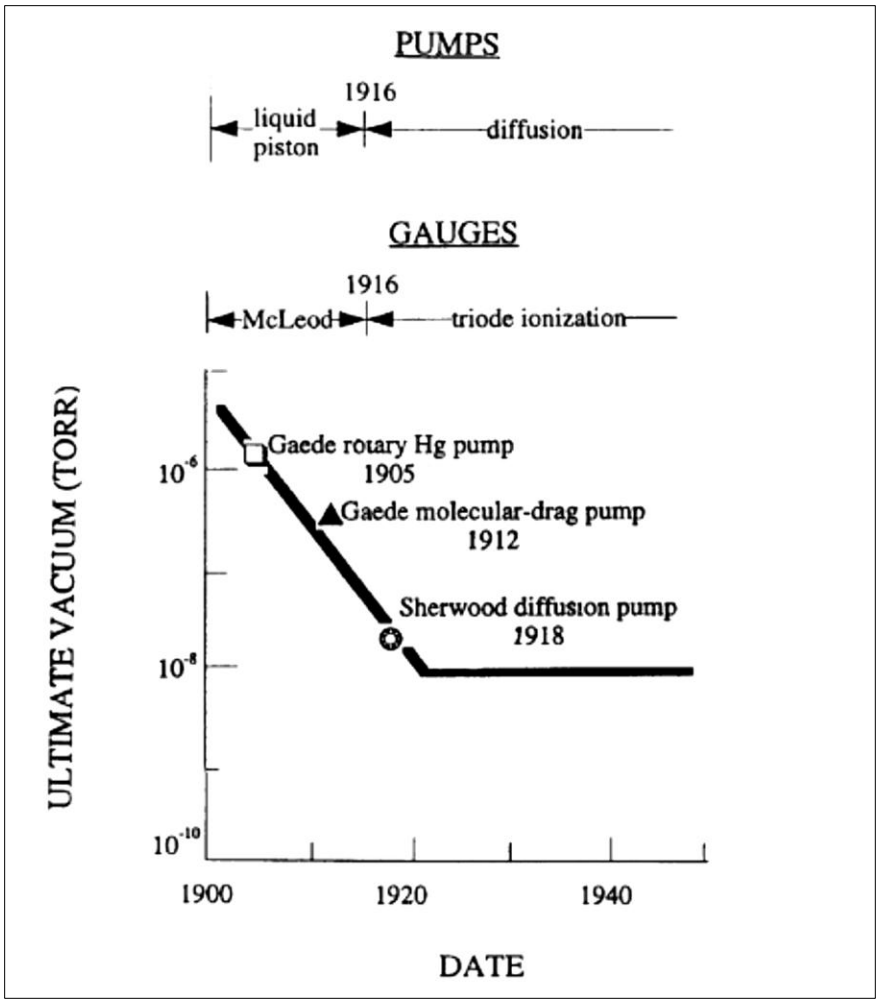

Figure 4.2: The vacuum development time scale from 1900 to 1950. Figure reproduced from reference 51.

It was in 1950 where the deadlock was broken, when the Bayard Alpert gauge was discovered and this led to ultra-high vacuum (UHV) as well as the modern era of vacuum technology. Industries such as vacuum-tube electronics and television drove the advancement in vacuum technology in the 1960's. By the mid 1960's the technology had grown significantly such that apparatus for generating UHV were readily available commercially.[1] These apparatus were combined with electron, ion and photon sources and used to measure the scattering of beams of these particles.

The importance of UHV in surface science experiments is significant. Under UHV conditions a clean surface becomes stable for a long period of time (hours) and this then makes it possible to characterize the composition, structure and study the reactions occurring on the surface. Thus

UHV is the heart of surface science. This chapter will be focused on commissioning a UHV chamber equipped with XPS apparatus, LEED and mass spectrometer for TPD.

4.2.2 Attaining UHV

The first step of commissioning the chamber was to attain UHV. The chamber is equipped with rotary, turbo, titanium sublimation and ion pumps. The mass spectrometer (MS) was used to find leaks on the chamber. A significant oxygen peak from the MS indicates when there is a leak. Helium gas is then used for leak testing because it contains the smallest gas molecules. Most importantly it is inert therefore it will not react with any of the materials inside the chamber. The MS is used to monitor the He pressure while spraying parts different parts of the chamber such as the flange shown in figure 4.3.

If a leak is located, the first action is to tighten the bolts on the flanges so that the knife edge cuts more deeply into the copper gasket. The copper gasket serves as the mechanical vacuum seal. If that does not close the leak the gasket shown in figure 4.3 is changed. In some instances the flange is also changed but it is always the last option when the two methods mentioned above fail to close the leak and this occurs when the knife edge itself is damaged. The above methods are repeated for different connections and flanges on the chamber until the oxygen peak decreases. This then means the leaks have been closed. The second step is to bake the chamber, including the ion pump. The UHV chamber is baked because rest gases such as water are adsorbed on the chamber walls and they have high vapour pressures that prevent the system to go to, into the UHV range. These gases desorb and are pumped away very slowly. Baking accelerates the process of pumping out these gases. The initial step of baking the chamber involves disconnecting all components from the chamber that cannot withstand high temperatures. This is followed by covering the chamber with foil as shown in figure 4.4 to prevent heat loss and then heat the chamber to the desired temperature.

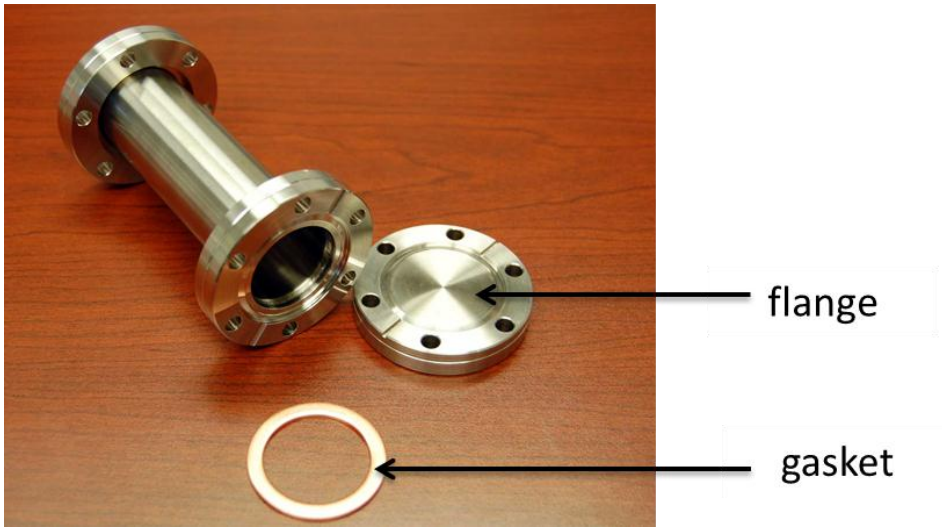

Figure 4.3: A picture showing a gasket and a flange which are parts used in a UHV chamber. Reproduced from reference 51.[53]

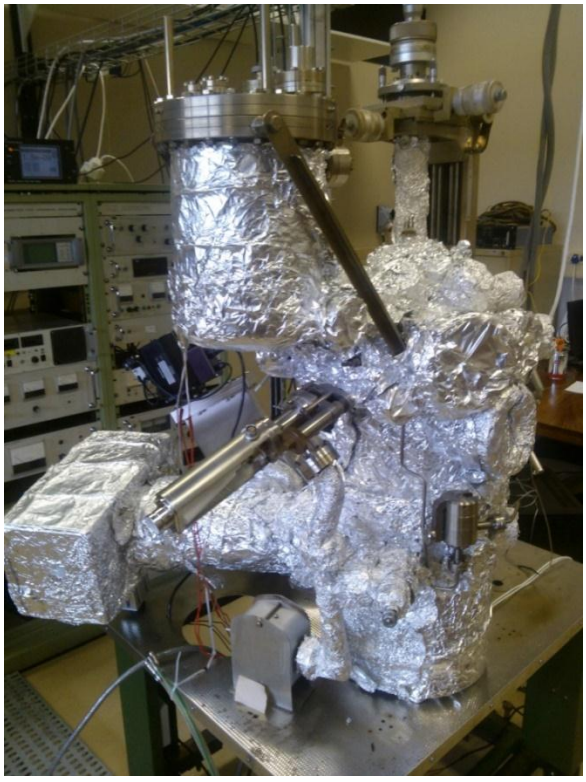

Figure 4.4: A picture of the UHV chamber wrapped with an aluminium foil during baking.

4.2.3 Commissioning and calibrating the XPS technique

The aim was to calibrate the XPS technique so that the results obtained are comparable to literature results. This was necessary as a new computer control had been implemented and the relationship between the control voltage sent to the electron analyzer and the electron energy detected had to be determined. A gold foil was the material that was used for the calibration of binding energy scale, mainly because it is one of the commonly used calibrants due to its strong XPS lines (peaks) and being a noble metal it is easy to clean and remains clean. Figure 4.5 shows the sample manipulator with the gold foil mounted. The reference binding energy values for the gold 4*f* peaks used for calibrations were 84.0 and 87.4 eV for $4f_{7/2}$ and $4f_{5/2}$ respectively.[54]

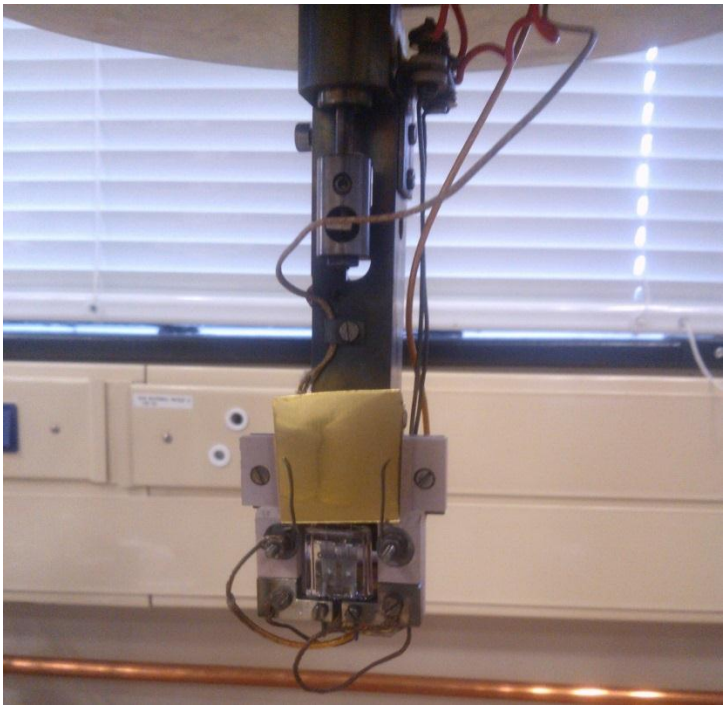

Figure 4.5: Illustration of the sample manipulator and the gold foil.

The initial step was to ensure that the electronics and the XPS computer program transfer information between each other accurately through the data acquisition instrument. XPS measurements of the gold foil were taken and it was noted that there is a random shift in the Au peaks after different runs. An example of the resultant shifts in the 4*f* Au peaks is illustrated in figure 4.6 and this was the case for each run meaning the peak positions changed with every run.

The example in figure 4.6 shows two runs which were taken at the same pass energy of 200 eV with a shift of approximately 2 eV. These shifts do not signify any chemical change in the Au foil because they are random. The figure also illustrates the low count rate of the runs.

The sample and analyzer grounding was improved after it was discovered that the electrical connections to ground in the lab were faulty. These must be grounded together for the electron energy detected to be related to the binding energy of the electron in the solid. Another problem was found to be in the electronics that control the electron analyzer. It was discovered that resistors and capacitors in these electronics had degraded and needed replacement.

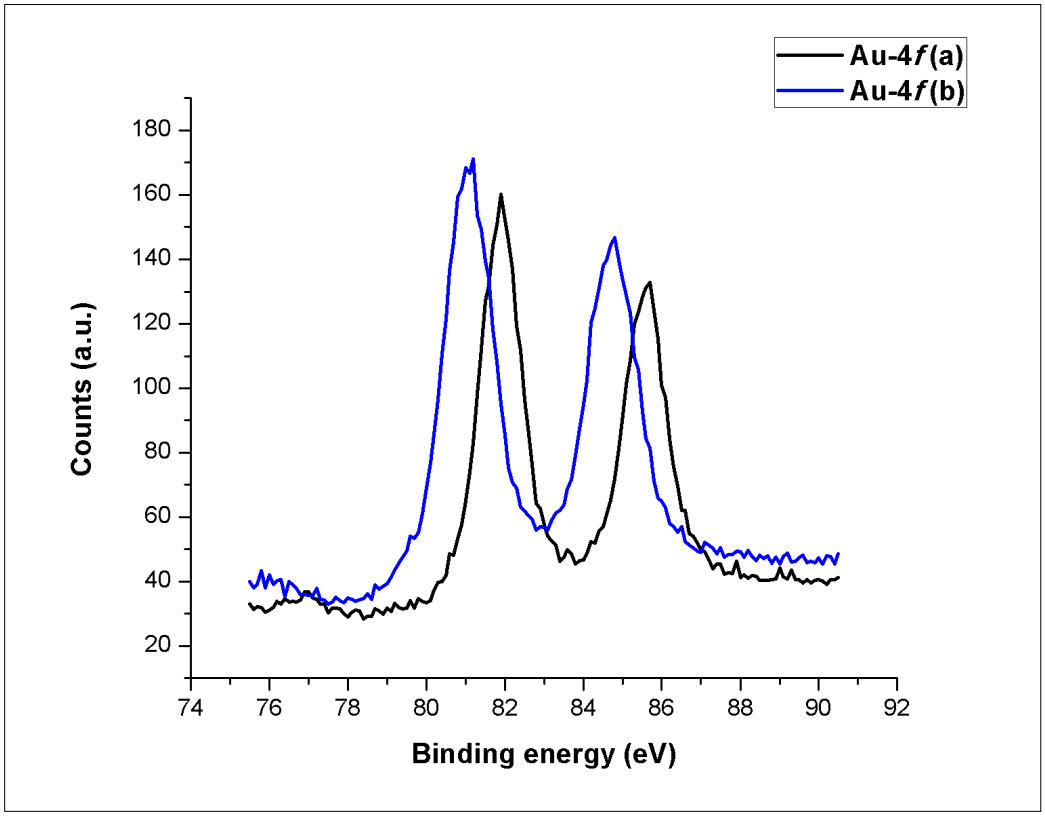

Figure 4.6: Spectrum of the Au 4*f* peaks at a pass energy of 200 eV, illustrating the shift in peak positions between spectra (a) and (b).

After components were replaced and the equipment well grounded, a significant improvement was observed. The calibration of the hemispheric analyzer and the X-ray source were optimized including the sample position. After a long quest the commissioning and the calibration of the XPS was achieved and it is illustrated in figure 4.7 which shows the Au 4*f* peaks. The peak

positions of the Au $4f_{5/2}$ and $4f_{7/2}$ are 83.3 and 86.9 eV respectively, compared to 84.0 and 87.4 from literature.[54] The difference in values between literature and experimental is not significant and the problem concerning shifting of the peaks is considered solved.

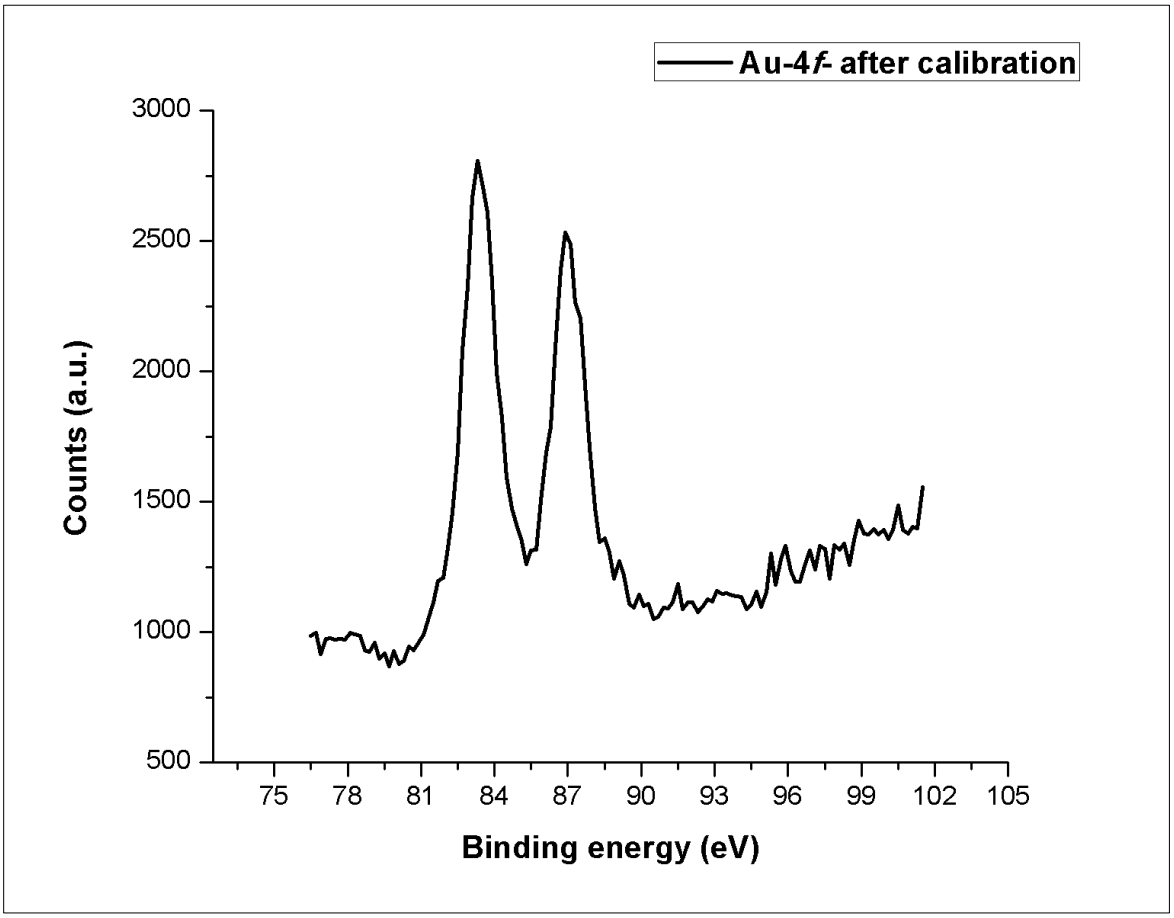

Figure 4.7: Spectrum of the Au 4*f* peaks at pass energy of 50 eV, after calibration. The peak positions are close to the literature values.[54]

In the process of calibrating the XPS technique the ion sputter gun used to clean the sample was also installed and calibrated. An ion sputter gun bombards the sample surface with high speed ions. A plasma is created by ionizing a sputtering gas, which is usually a heavy and inert gas. The commonly used gas is argon. The collision of ionized particles with the surface results in an energy transfer and then atoms are knocked off from the surface.

The Au foil was sputtered after calibration of the ion sputtering gun and the results are shown as an XPS spectrum in figure 4.8. Sputtering the Au foil mean the intensity of the 4*f* peaks must

increase because after removing the surface contamination we see more of the sample. The first and second peak increased by 2000 and 1500 counts respectively after sputtering the gold foil surface. Thus there is an increase of approximately 114.2 and 120% for peak one and two respectively in counts in figure 4.8 compared to the spectrum in figure 4.7. This means the sample was successfully sputtered and the ion sputtering gun is working.

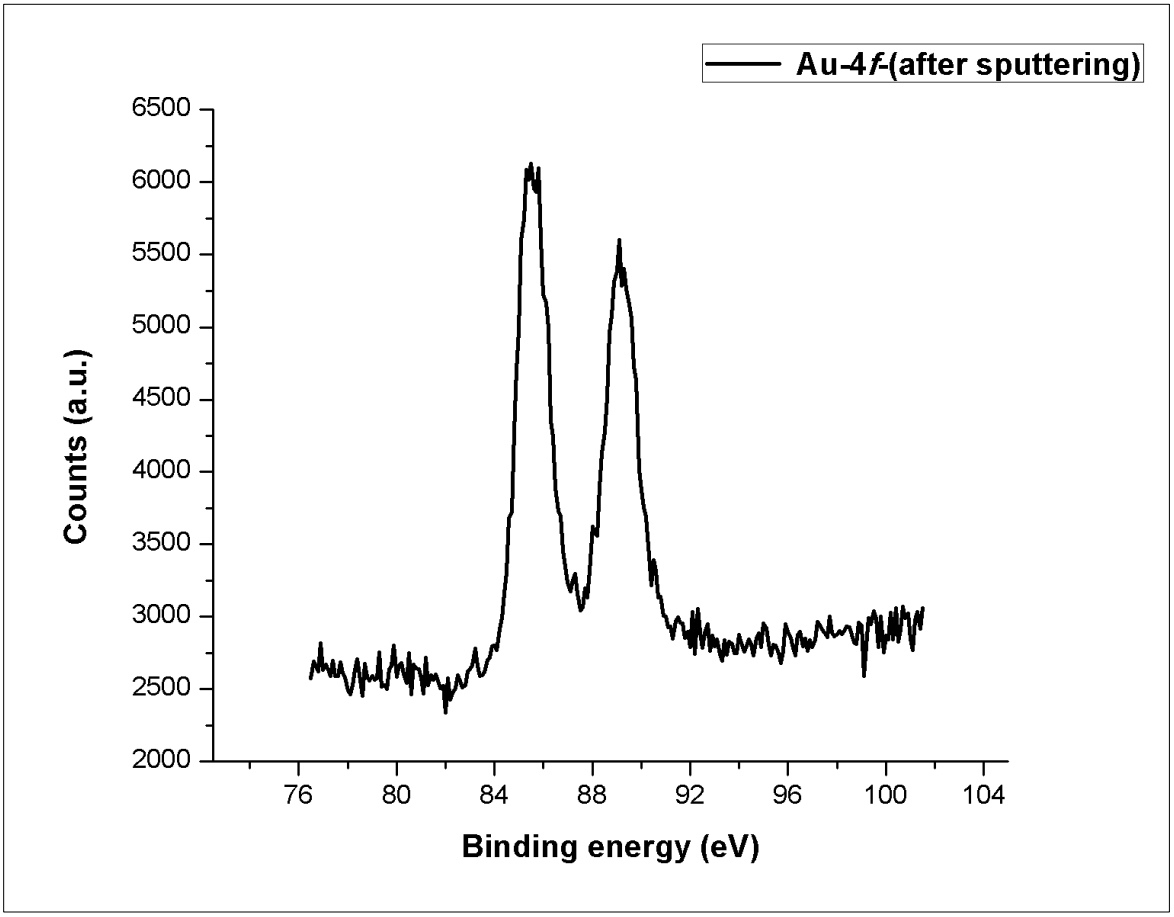

Figure 4.8: Spectrum of the Au 4*f* peaks at a pass energy of 50 eV, illustrating the increase in counts after sputtering the sample.

4.2.4 Commissioning the components for TPD.

To carry out TPD measurements you need a mass spectrometer, heating system and a computer program that will record the sample temperature and the partial pressure of the gas of interest simultaneously. The first step was to design and build a sample holder to hold the sample and

make it convenient to heat. The home-made sample holder shown in figure 4.9 was made from stainless steel metal and the Co{0001} crystal was mounted using tungsten wires.

The second step was to come up with a heating system to maximize the exclusive heating of the sample. This in return will result in almost exclusive desorption of molecule or atoms that are on the crystal surface to be then detected by the quadrupole mass spectrometer.

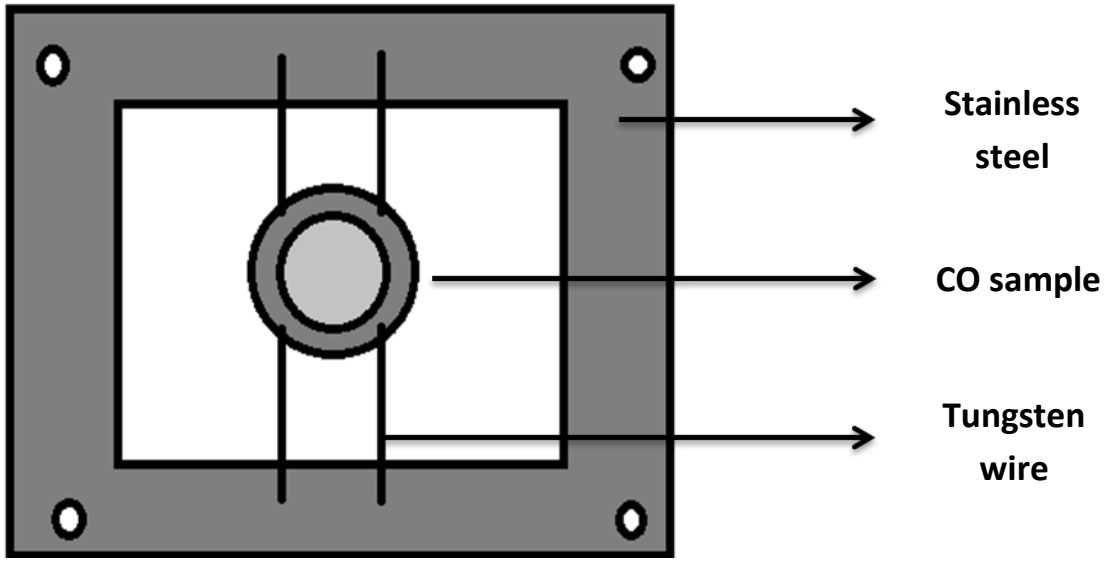

Figure 4.9: A schematic of the sample holder made from stainless steel and the Co{0001} crystal mounted using a tungsten wire.

Two heating methods were explored, heating by radiation and electron bombardment heating. The latter is an ideal heating method that maximizes heating of the sample exclusively. In this method a high voltage is applied on the sample making it positive. At a certain current the filament emits electrons. Then the positive sample accelerates them resulting in almost exclusive heating of the sample. This phenomenon is illustrated in figure 4.10. Sequential heating of this method is as follows: the filament current is increased and the temperature on the sample is monitored using an attached thermocouple. The flow of current on the sample is also monitored so as to determine at what temperature the flow of electrons starts to take place. At a certain current the filament produces enough electrons to allow measurement of current on to the sample. Ideally this process must occur at low temperature (this is the temperature due to

radiation from the filament) so that the electron bombardment heating can account for all the desorbed molecules on the surface. If the process occurs at slightly high temperatures some of the adsorbed molecules might have desorbed already while attaining the current that allows electron bombardment heating. The voltage applied to the sample is also varied which optimizes the acceleration of electron.

Table 1 shows tests run using the electron bombardment heating system. The lowest filament current that results in emission of electrons is 2.4 A and it was kept constant since the plan was to achieve emission of electrons at the lowest possible filament temperature. Nonetheless the sample temperature at the current of 2.4 A was 255 ºC which is quite high. At this temperature there is a possibility that some adsorbed molecules might have desorbed already even before the electrons heating process. The voltage applied was increased by a magnitude of 100 V at each step in order to observe the change in temperature and current due to the flow of electrons from the filament to the positively charged sample.

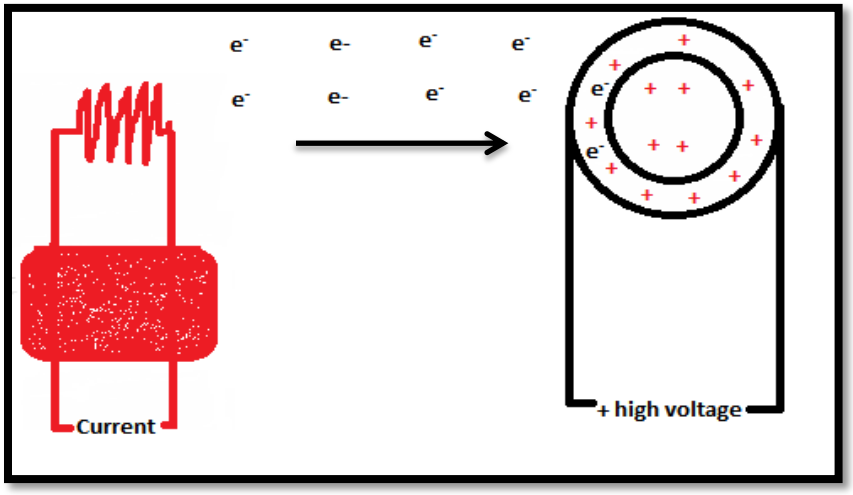

Figure 4.10: A schematic illustration of the concept of electron heating for TPD technique.

For both temperature and current a trend is observed as shown in table 1, where the change for the first 100 V increase is significant and the change decreases as the applied voltage is increased further. This is proposed to be due to the fact that the number of electrons produced by the filament does not change even though the number of electrons drawn by the positive sample increases with an increase in voltage. Eventually the saturation point will be reached and the temperature will only increase slightly due to increased electron energy. Another method we

tried was to use filaments with less power but the problem we encountered was that the minimum current needed for electron heating to occur is not reached thus we used a 100 Watt filament.

In the second heating method, which is heating by radiation, it is a challenge to heat the sample exclusively without getting desorption peaks from other parts of the chamber other than the sample. A way of increasing the ability to heat the sample exclusively was put in place. The idea put in place was to insert a shield that will be place between the filament and the sample so as to shield the heating of the sample and this is illustrated in figure 4.11(a). The shield was made using stainless steel. Then the radiation from the filament can first desorb the molecule from the surroundings without heating the sample, because we are interested in desorption of adsorbed molecules from the sample not the rest of the chamber.

Table 1: Electron heating method tests at the lowest filament current that produces a flow of current.

	Filament current (A)	Voltage applied (V)	Current drawn (mA)	Sample temperature (ºC)
Test 1	2.4	100	15	255
Test 2	2.4	200	38	310
Test 3	2.4	300	50	361
Test 4	2.4	400	60	382

The heating of the sample with and without the shield was compared at four different filament currents. The results were recorded and are shown in table 2. Results show that using the shield decreased the amount of heat that reaches the sample by a notable amount. For all the filament currents the sample temperature when the shield was in place is lower than the lowest sample temperature observed for the electron heating method. Therefore the heating by radiation method is better than the electron heating method. the

Table 2: Heating by radiation method sample temperatures, with and without the shield in place, at four different filament currents.

Filament current (A)	Sample temperature (ºC)	
	No shield	Shield in place
2	197	22
2.4	291	103
2.8	334	137
3.4	474	179

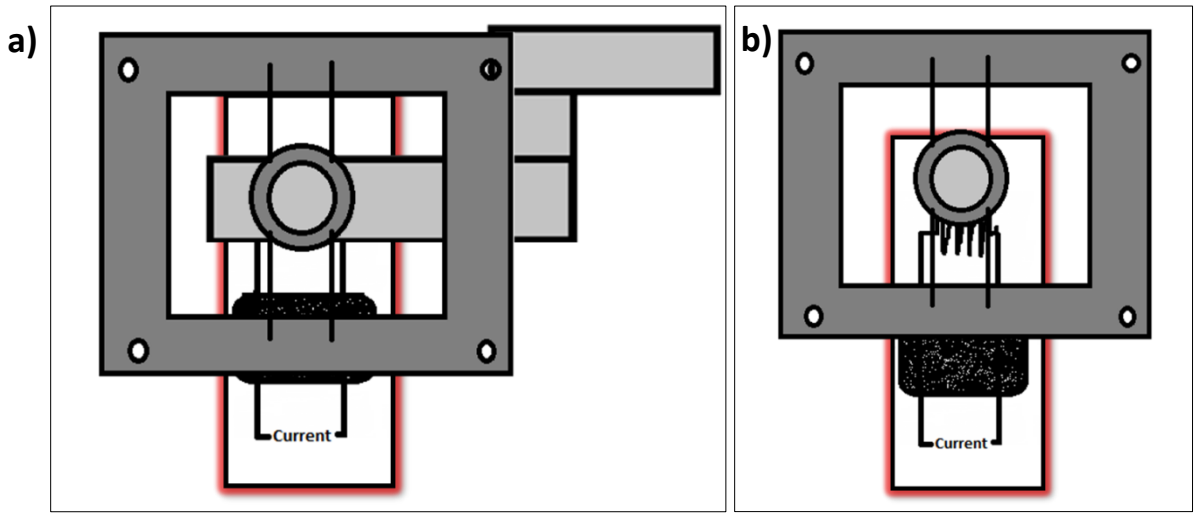

Figure 4.11: The schematic illustration of a) a shield in place between the sample holder and the filament b) the filament and sample without the shield.

In conclusion between the two methods discussed above heating by radiation gave us better results compared to the electron heating method. Even though electron heating is an ideal method it did not yield desired results, because electron heating occurs at high temperatures compared to the minimum temperature needed for our desorption studies.

4.2.4.1 Testing the heating by radiation method for TPD analysis

The reliability and ability of the heating by radiation method was tested by adsorbing carbon monoxide (CO) gas on the surface of the Co{0001} crystal. The Co{0001} surface was first cleaned by Ar sputtering but the cleanliness of the surface was not checked. The base pressure of

the chamber and CO partial pressure were 5.4×10^{-10} and 1.3×10^{-9} Torr respectively. The base pressure of CO was recorded after heating the sample (current of 2.7 A = 394 ºC) so as to pump out the CO that is adsorbed on the crystal surface and surrounding surfaces (such as sample holder and sample manipulator). The sample was then allowed to cool to room temperature. The CO gas line or valve was opened to a pressure of 2.2×10^{-7} Torr for approximately 5 seconds with an aim of approximating one Langmuir ($1\ L = 10^{-6}\ Torr.s^{-1}$) and then closed. The CO partial pressure measured using the MS increased to 3.6×10^{-6} Torr in the process.

The filament was then heated with a current of 2.7 A which heated the sample to 166 ºC with the shield in place. The CO partial pressure then increased to a maximum of 4.0×10^{-8} Torr from 2.0×10^{-9} Torr after closing the CO gas line. This increase in CO is from the surrounding surface because from literature the desorption peak of CO on a Co surface is around 580 K (306 ºC).[55] The shield was then removed and the sample temperature increased to 435 ºC and the CO pressure to 6.5×10^{-8} Torr. This means that approximately 2.5×10^{-8} Torr of CO desorbed from the Co surface. The test showed that the heating by radiation method will work for TPD analysis. The last component is to finish writing a computer program that will collect temperature readings from the thermocouple and correlated them to pressure reading from the quadrupole MS. Other than that the calibration of components used for TPD analysis is complete.

4.2.5 Commissioning other components of the chamber.

A glass doser was built for the aluminium tri-sec-butoxide molecule. The doser was connected to a valve and then to the chamber as shown in figure 4.13. The glass doser was tested by opening the valve and the fragments of aluminium tri-sec-butoxide molecule were visible on the MS. This was used as way to determine whether the molecule can be dosed on the Co surface using the pressure difference between the doser and the chamber. The test was carried out and the results are shown in figure 4.14 the spectrum on the left. The results were compared to literature which is the spectrum on the right in figure 4.13. Even though the literature spectrum was taken under nitrogen it is still comparable to our results. The pronounced similarities of the two spectrums are the three clusters of peaks at mass of approximately 11 to 21, 25 to 32 and 40 to

50. This result of the test showed that introducing the aluminium tri-sec-butoxide molecule using the pressure differential into the chamber is possible without the need to heat the doser.[56]

In conclusion UHV conditions (3.0×10^{-10} Torr) were achieved. The XPS, TPD components and the glass doser for introducing the aluminium tri-sec-butoxide were commissioned and calibrated. The LEED was installed and tested but not commissioned as yet. Therefore the commissioning of the UHV chamber was successful with a few outstanding details such as the computer program for TPD analysis. The LEED was also installed and it was functioning but it was not commissioned and calibrated as yet.

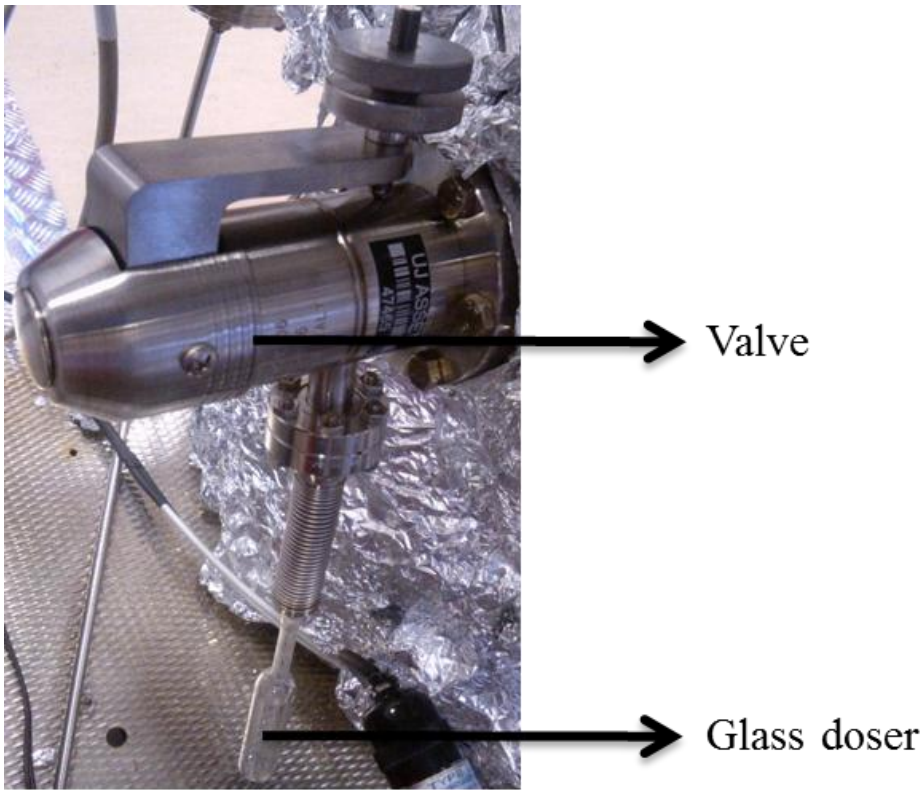

Figure 4.12: A picture showing the home-made glass doser and a valve connected to the chamber.

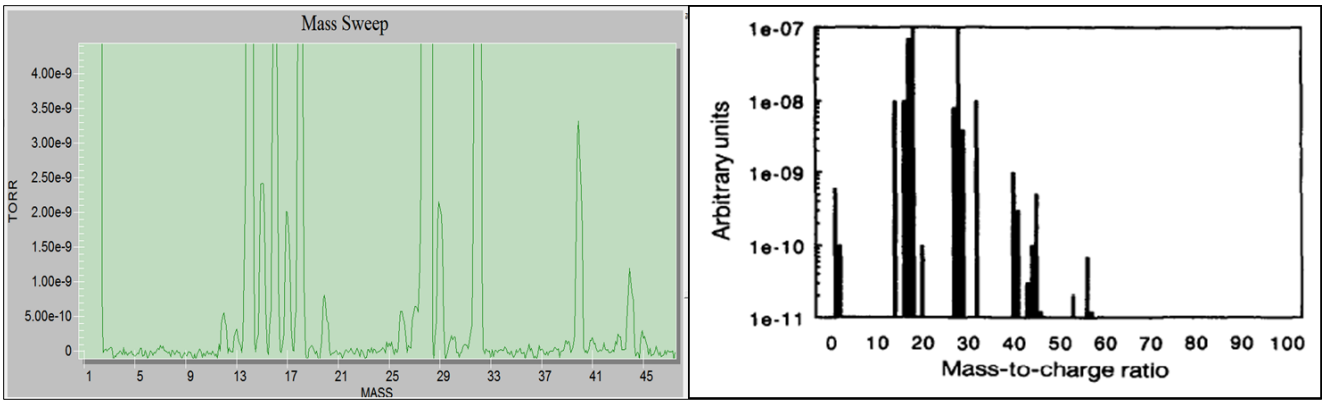

Figure 4.13: Mass spectra of fragments of aluminium tri-sec-butoxide, (left) from our doser test and compared to literature results (right).

4.4 Future work

The aim of commissioning the UHV chamber was to study the effect of mimicking metal-support interaction on Co{0001} surface. With the focus on alumina type interactions, and these will be made by adsorbing aluminium tri-sec-butoxide on the Co (0001) single crystal surface.CO will be used as probe molecule to investigate the influence of the presence of species mimicking the metal-support interactions.

As a result of time constraints and the unexpected prolonged process of commissioning the UHV chamber the study was not carried out. The main reason for the prolonged commissioning process was the fact that most of the components of the chamber were old and fragile so working with them was a major challenge and some them needed to be repaired or replaced. Nonetheless the UHV commissioning process was taken as an important part of the project and it was successful. So the future work would be to continue and carry out the study as mentioned above.

CHAPTER 5

NO on Ir{100}

5.1 Introduction

Nitrogen monoxide (NO) is a colourless and odourless compound produced from reacting oxygen and nitrogen gases at high temperatures. This reaction is endothermic and is commonly found in car exhaust during the combustion of hydrocarbons. NO is part of a group of compounds known as nitrogen oxides which include nitrogen dioxide (NO_2). At high concentrations these compounds cause harm to the plant life.[57] These compounds also contribute to the formation of acid rain and ground layer ozone. Even though these compound harm the environment there are no cases about them having an effect on human health.[57] Iridium is a transition metal that is part of the platinum group. It is a very hard, brittle and silver-like. It is the second densest element and also the most corrosion resistant element even at high temperatures.[58]

The adsorption of molecules on metal surface is an active area of research in the field of heterogeneous catalysis due to its application in various technological processes. Due to environmental issues discussed above, there is a need for conversion of NO from a car exhaust into N_2 which is less harmful. Several studies have been done to determine which metal reduces NO effectively. It was discovered that Ir is the most promising metal to reduce NO to N_2 under oxidative conditions.[59] Iridium is a transition metal that is part of the platinum group. It is a very hard, brittle and silver-like. It is the second densest element and also the most corrosion resistant element even at high temperatures.[58] The low index Ir{100} surface has interesting properties. The Ir{100}-(1×1) phase like Pt{100} undergoes hexagonal reconstruction to a stable (1×5) phase. This reconstruction can be lifted by adsorbing adsorbates such as CO and NO.[60] The (1×5) phase is denser than the (1×1) by 20% therefore there is a change in reactivity when moving from one phase to the other.[61] This phenomenon is known as structure sensitivity in

heterogeneous catalysis and it is important for molecular-level understanding of NO interaction with Ir{100} surface.[61]

5.2 Literature review

There are several studies that were done on NO adsorbed Ir{100} previously but they did not give the exact structure of the NO dissociated on the Ir{100} surface. Studies done by Gardener et al. using reflective absorption infra-red spectroscopy (RAIRS) and LEED showed that NO adsorbs molecularly at low temperatures.[59] It was discovered that on the (1×1) phase NO adsorbs dissociatively at temperatures above 300 K and the LEED pattern changes from (1×1) to $p(2 \times 2)$ to indicate that a new overlayer is formed. As the NO coverage is increased changes on the RAIRS peaks were observed and a streak on the LEED spots at positions $(1/2, 1/6)$ developed.[59] The saturated overlayer was heated and a desorption pattern was observed with atomic oxygen and nitrogen as desorbing molecules. At a temperature of 300 K there were no IR N-O stretch peaks observed which implied dissociation of NO on the Ir{100} surface. Above 400 K the LEED pattern showed a $p(2 \times 1)$ pattern overlayer which was due to the presence of oxygen on the surface. Therefore the change in the LEED pattern (from (1×1) to $p(2 \times 2)$) observed and the disappearance of NO stretch vibrational modes, both imply dissociation of NO at temperatures above 300 K.[59] The (1×5) Ir{100} phase NO adsorbed molecularly at all temperature which reveals the less reactivity of the hexagonal closed packed (hcp) phase compared to the (1×1) phase.[59]

Khatua et al. used RAIRS and DFT to study adsorption of NO on Ir{100} at 95 K.[61] They studied both the (1×5) and (1×1) phases of Ir{100}. On the latter phase, from RAIRS they observed NO peaks at lower coverages which implied a non-dissociative adsorption of NO on the (1×1) surface. DFT results showed that at 0.2 ML the bridge site is the most stable adsorption for NO and at 0.5 ML, a $c(2 \times 2)$ adsorption overlayer was observed with the NO molecule still on the bridge adsorption site.[61] This study confirmed the results from the Gardener et al study that the non-dissociative adsorption of NO on Ir{100} occurs at low temperatures.

Erikat et al. used DFT to study the molecular dissociation of NO on Ir{100} surface.[62] This study showed that the most stable adsorption sites for N and O after the dissociation of NO are hollow

and bridge site respectively. The results of this study were in agreement with those by Khatua et al. about the stable adsorption site of the NO molecule on the surface, which is the bridge site. The study also revealed that the bending of NO is the initial step in the dissociation process due to the back donation of the *d* band of Ir to $2\pi^*$ of NO orbital which then weakens the bonding.[62]

Another insightful study was on O_2 adsorbed on Ir{100} surface. Johnson and colleagues used a combination of DFT and LEED to show that O_2 dissociates on the (1×1) surface of Ir{100} into atomic O. This then forms a $p(1 \times 2)$ overlayer structure with adsorption on a bridge site on the Ir surface, this is unusual based on previous studies where oxygen generally occupies a four-fold hollow site on fcc (100) surfaces.[63] DFT calculations confirmed that a bridge site adsorption is the most stable adsorption site for O on Ir{100} and that even at low coverages, O always form small islands of $p(1 \times 2)$ periodicity. The above mentioned overlayer of O on Ir{100} is stabilized by row pairing of the first layer iridium atoms, which moved by a total of 0.15 Å towards each other. This surface reconstruction played a significant role in stabilizing the rather unusual configuration of oxygen.[63]

5.3 Results and discussions

The aim of the study is to use the experimental I-V curves obtained from the University of Cambridge of NO adsorbed on Ir{100}-(1×1) and determine the surface structure using the CLEED program. The NO exposure is 0.4 L at 300 K and the LEED measurements were taken at 200 K. A $p(2 \times 2)$ LEED pattern was observed which is shown in figure 5.1 and 14 I-V curves each corresponding to spots of a (2×2) pattern were extracted with a cumulative energy range of 2262 eV(total energy of the I-V curves). In figure 5.1, the schematic on the right is a (2×2) diffraction pattern drawn using LEEDpat program. The larger or brighter spots in figure 5.1 are due to the superposition of diffraction spots by the metal surface and adsorbates (integral order spots) and the remaining spot are due to the adsorbates only (fractional order spots).

The LEED calculations were performed using the CLEED program, written by Georg Held.[20] The CLEED program performs a fully dynamical calculation at every step of the search using the downhill simplex algorithm as explained in chapter 3. For both the clean surface and NO adsorbed on Ir{100} calculations, the scattering from the bulk was calculated using the Pendry's

layer doubling method and the bulk interlayer spacing used was 1.916 Å.[19] The iridium, oxygen and nitrogen phase shifts were obtained from Held et al.[64] Non-geometrical parameters consisted of Debye temperature of 420 K for iridium. In order to properly represent the scattering by iridium atoms and achieve convergence, it was necessary to use l_{max} = 10, while only $l_{\max}$ = 8 was necessary for oxygen and nitrogen. The l_{max} parameter is used to allocate memory requirements to each atom from a list of Clebsh-Gordan coefficients used for atom scattering in the calculation. [20]

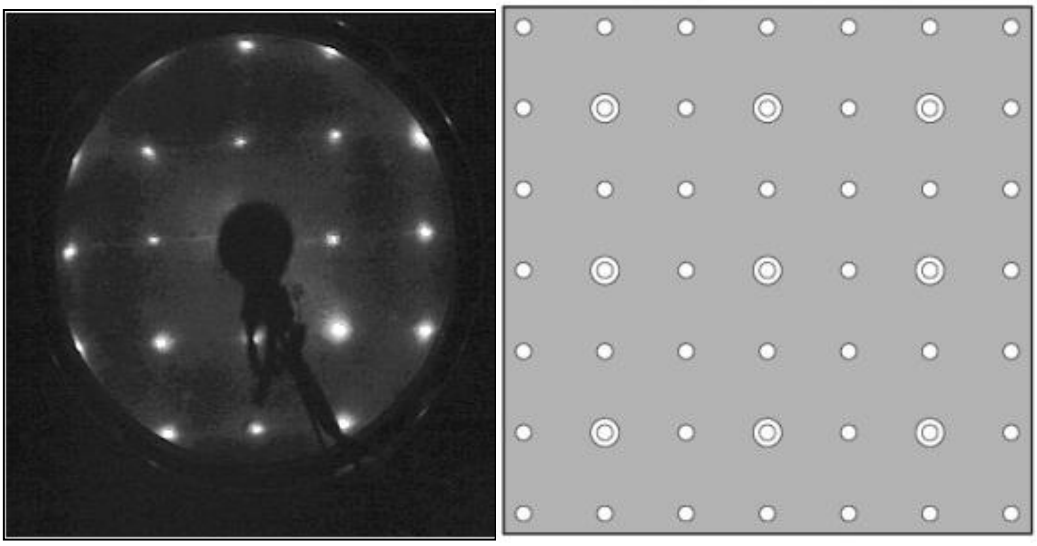

Figure 5.1: (a) image observed during LEED experiments at 120 eV and (b) a pattern drawn using LEEDpat program of a (2×2) diffraction pattern.

The uncertainties for each structural parameter were calculated using Pendry's method[19] where the uncertainty of a parameter p is defined in terms in of an *RR-factor*:

$$\Delta p = |p_1 - p_0| \cdot \sqrt{\frac{RR \cdot R_{(P_0)}}{R(p_1) - R(p_0)}},$$

where p_1 is the value of parameter p for the perturbed structure and p_0 is the value of p for the optimized structure. A distance of 0.1 Å between p_0 and p_1 was used for all parameters as is common practice.

5.3.1 Clean surface structure of Ir{100}-(1×1)

The CLEED calculation for the clean iridium (1×1) surface was performed using experimental I-V curves collected in the energy range of 40-300 eV and then after averaging the equivalent spots the total energy range was 780 eV. In the search only the first three layers of Ir were relaxed. The initial run was performed using the bulk value of 0.0363 as the vibrational amplitude and this value was used for all three layers. The R-factor obtained was 0.19 ± 0.04 which was good but for a clean surface we expect an R-factor ≤ 0.2. The vibrational amplitude to the top most layer iridium layer was changed while keeping the vibrational amplitude of rest constant. The vibrational amplitude that gave the best R-factor value of 0.17 ± 0.03 was 0.06 Å.

Table 5.1: Parameters for the best fit structure of Ir{100} clean surface compared with previous structural studies; spacings d_{12} , d_{23} , and d_{34} are defined in Figure 1.

	$\mathbf{d_{12}}$	$\mathbf{d_{23}}$	$\mathbf{d_{34}}$	**R-factor**
LEED, this work	1.84 ± 0.03	1.92 ± 0.03	1.92 ± 0.04	0.17
	(-3.9%)	(0.16%)	(-0.30%)	
LEED, Reference 6	1.83 ± 0.03	1.94 ± 0.03	1.91 ± 0.03	0.12
	(-4.5%)	(1.3%)	(-0.3%)	
DFT, Reference 60[60]	-6.6%	0.0%	n/a	n/a

Figure 5.2 shows the side view model of the Ir{100} structure and while figure 5.3 is a graph of the I-V curves comparing the calculated (dashed) and experimental (solid) spectra respectively. From the I-V curves it is seen that the calculated spectra fits the data very well. The CLEED calculations are sensitive to the shape of the peaks rather than the intensity and this is reflected in the individual R-factor for each beam (diffraction spot). The parameters shown in figure 5.2 (the side view of the clean (1×1) phase) are given in table 1. The distance between the first and second layer was found to contract by 3.96% which is in good agreement with the previous results from LEED and DFT studies.[63,60] The distances between the second and third layer as well as the third layer and the bulk were found to relax to smaller extent too. These two distances between the layers showed the expansion and contraction of 0.16% and 0.30%, respectively. The

Ir{100}-(1×1) surface display oscillatory relaxation which is usually observed for high symmetry planes of most clean metal surfaces.

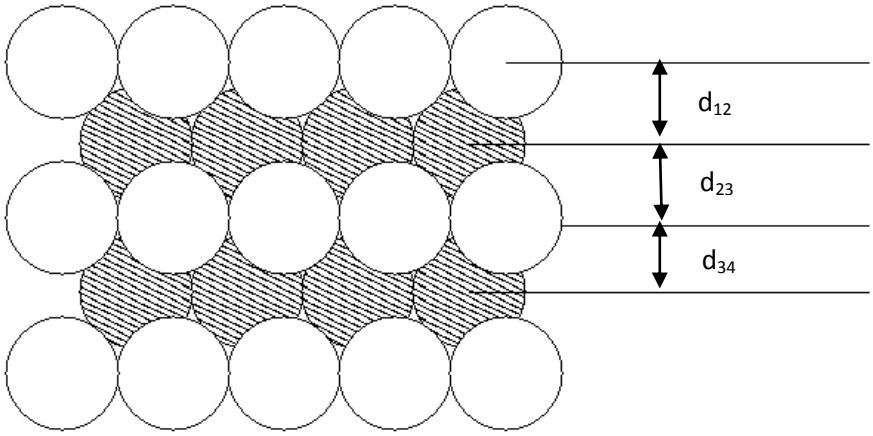

Figure 5.2: Side view of the schematic structure of Ir{100} clean surface.

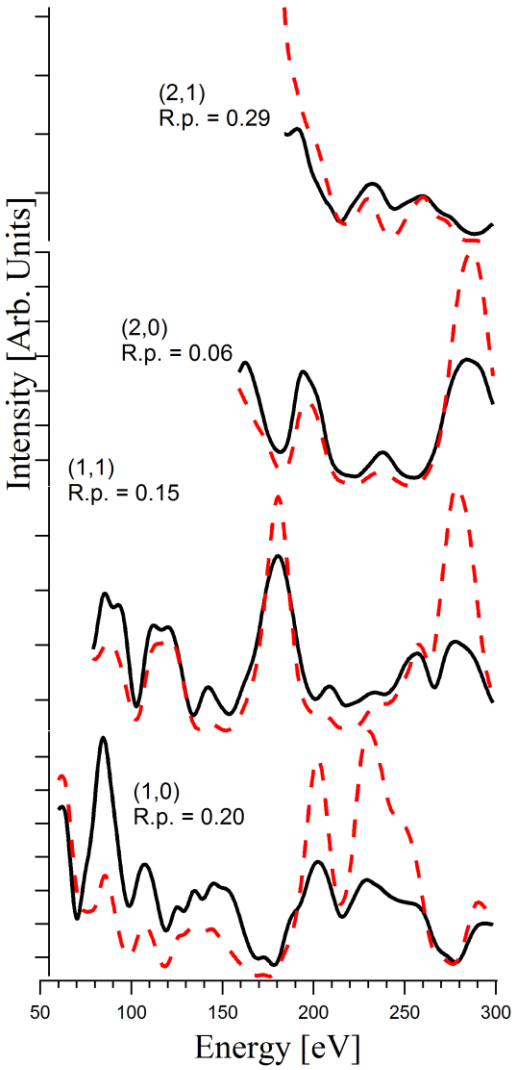

Figure 5.3: Comparison of experimental (solid lines) and theoretical (dashed lines) I-V curves for the structure of clean Ir{100} shown in figure 5.2. These curves represent the spots of a (1×1) Ir{100} surface.

5.3.2 NO on Ir{100}

Initially we considered two configurations of NO dissociation on the Ir{100} surface, phase mixing: where nitrogen and oxygen dissociate and share the same unit cell to give a resultant $p(2 \times 2)$ overlayer and phase separation; where nitrogen and oxygen form two different overlayer structures on the surface that result in an overall $p(2 \times 2)$ overlayer.

5.3.2.1 Phase mixing calculations

The preliminary searches were carried out to determine the possible adsorption site for nitrogen and oxygen for phase mixing. The four possible adsorption site are shown in figure 5.4 where configuration A is for an atop site, configuration B and C is for bridge site and configuration D is for hollow adsorption site. The two bridge site configurations differ in that in configuration B the nitrogen and oxygen atoms don't share an iridium atom while in configuration C they do. The search assumed an ideal bulk terminated substrate and nitrogen, oxygen and iridium atomic radii of 0.65, 0.60 and 1.35 Å respectively. Only the vertical parameters were varied and in each search a four-fold symmetry was maintained to further speed up the calculations. The minimum R-factor values for configurations considered were 0.70, 0.74, 0.75 and 0.71 respectively as shown in table 2. The atop site has the lowest value but it is still too high, because for atomic adsorbates we expect an R-factor of < 0.30 for the correct structure. This result therefore discards the phase mixing assumption.

Table 5.2: The R-factor values of results for phase mixing calculations with 7 parameter each and the error bar was 11 % for these calculations.

Configuration	R-factor
A	0.70
B	0.74
C	0.75
D	0.71

5.3.2.1 Phase separation calculations

The next step was to explore the phase separation idea where the oxygen and nitrogen atoms form $p(1 \times 2)$ and $c(2 \times 2)$ overlayer structures respectively. These two overlayers then result in a $p(2 \times 2)$ LEED pattern; this is explained in figure 5.5. For oxygen only the $p(1 \times 2)$ overlayer structure on a bridge site was considered, because in literature it was proven that oxygen adsorbs on a bridge site on an Ir{100} surface even at very low coverages.[63] In fact it

was shown by Lerotholi et al that at coverages less than 0.5 ML oxygen will form small $p(1 \times 2)$ islands on the Ir{100} surface.[17] The model of this surface structure is shown in figure 5.6. In the case of nitrogen two overlayer structure were considered, which are $p(2 \times 2)$ and $c(2 \times 2)$. A superposition of both these patterns with a $p(1 \times 2)$ will give a $p(2 \times 2)$ diffraction pattern as shown in figure 5.5. Figure 5.5 gives a detailed illustration of how a combination of a (2×1) and a $c(2 \times 2)$ results in a (2×2)LEED pattern. For both overlayer structures calculations were performed for atop, bridge and hollow adsorption site

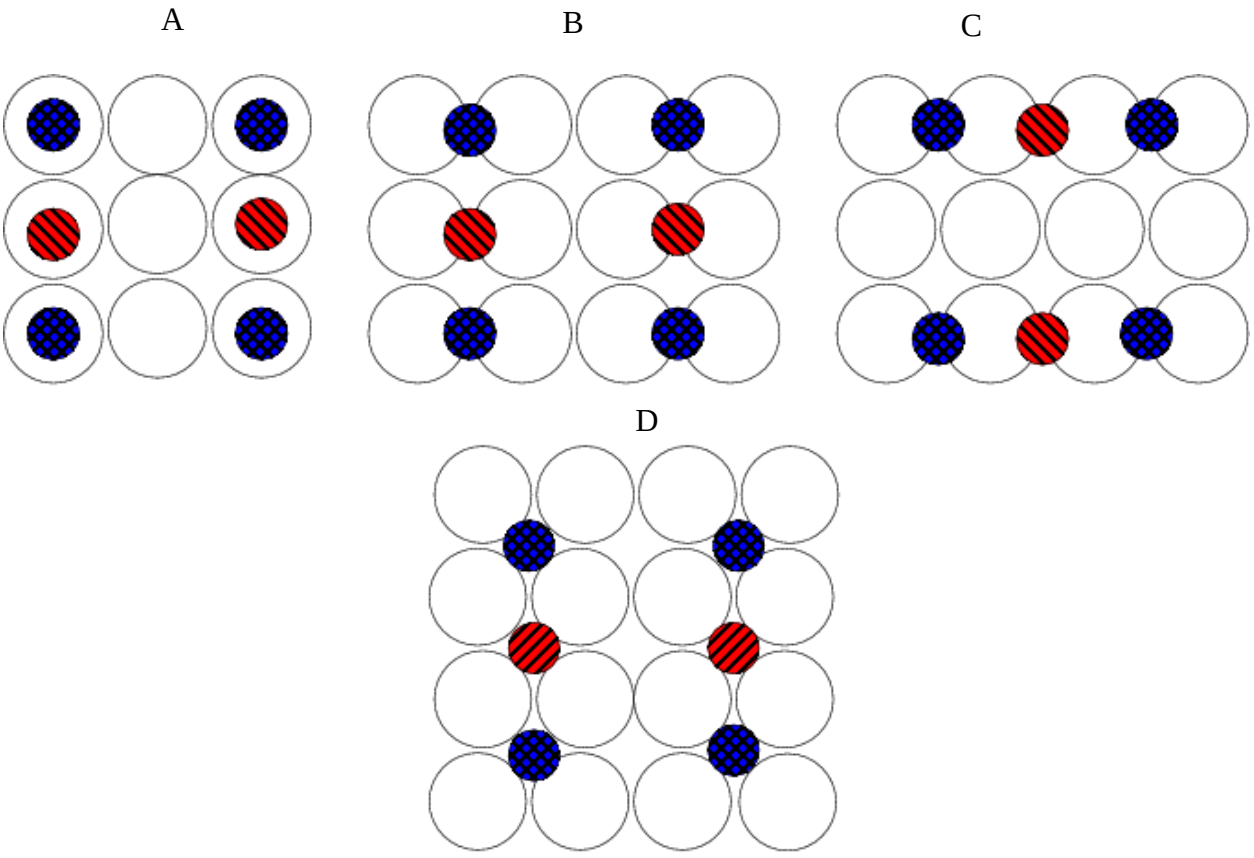

Figure 5.4: Possible configurations of phase mixing for dissociated NO on Ir{100}, where in configuration A atoms are adsorbed on an atop site, B and C on a bridge site and D on a hollow site. The red and blue spheres are oxygen and nitrogen respectively.

5.3.2.1 Calculations for oxygen only

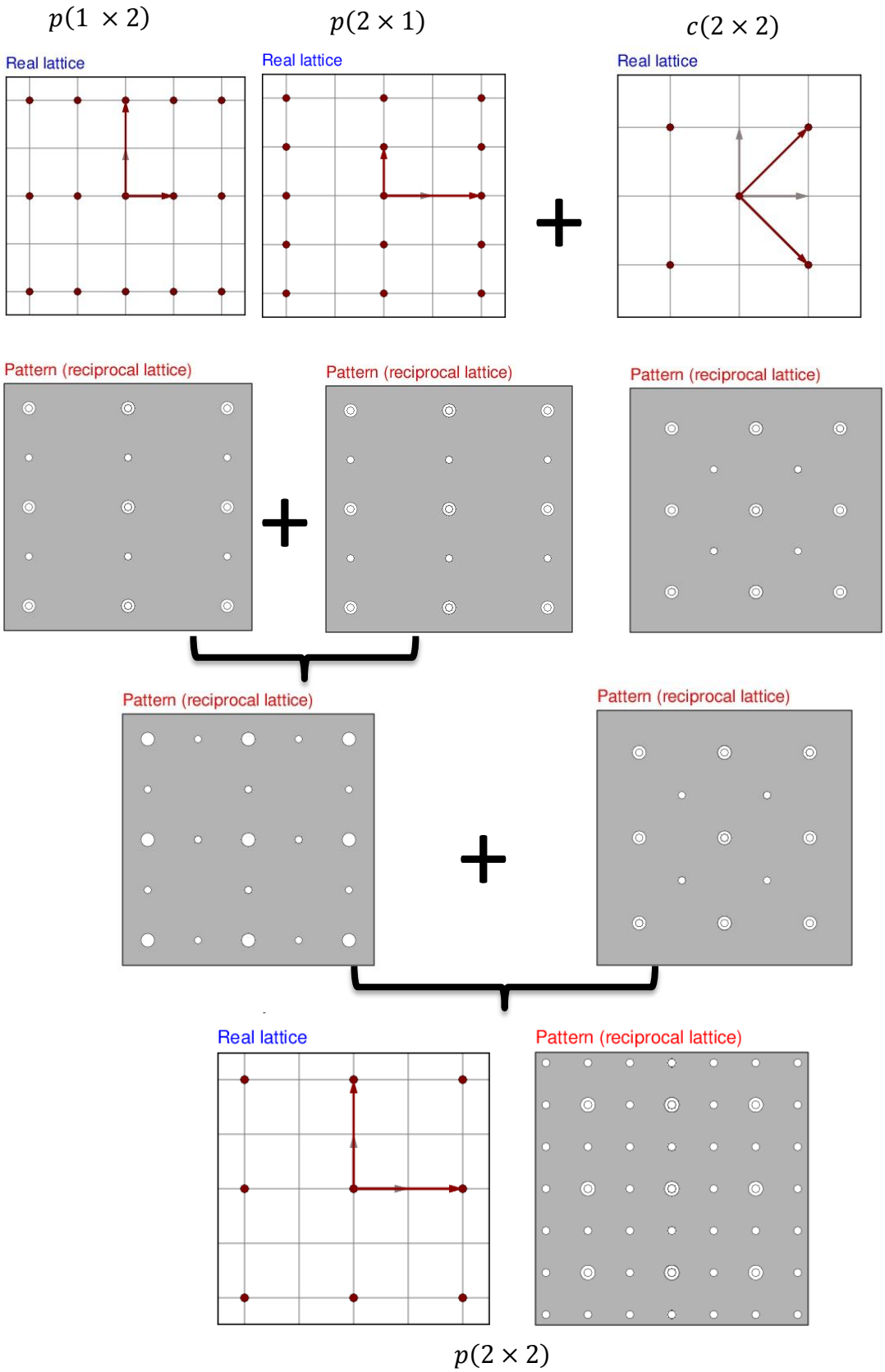

Figure 5.5: A schematic of LEED patterns in real and reciprocal space; showing that combining a $p(1 \times 2)$ (left) and $c(2 \times 2)$ (right) results in a $p(2 \times 2)$ (bottom).

The preliminary searches for oxygen only adsorbed on the Ir{100} surface we performed over z parameters and variation of the vibrational amplitudes. Only experimental I-V curves of integral spots and fractional spots from a (1×2) overlayer were used in these calculations. The lowest R-factor value obtained was 0.36 and this result was in good agreement with results obtained previously by Jonhson et al. of 0.33.[63] The calculations were refined by performing the xyz optimization and then relaxing the second layer of Ir.

Further refinement included introducing row pairing shown in figure 5.6 to the first layer of Ir (stabilized the bridge site in the $p(1 \times 2)$ structure). The lowest R-factor value obtained was 0.24 ± 0.03. The side view of the overlayer structure of oxygen on the bridge site is shown in figure 5.7 and the parameters in table 3. The corresponding comparison of theoretical and experimental I-V curves are shown in figure 5.8.

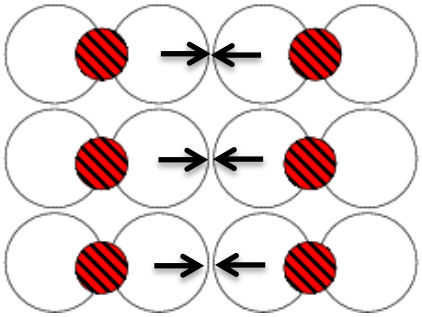

Figure 5.6: Schematic top view of oxygen adsorbed on a bridge site of Ir{100} surface in a $p(1 \times 2)$ overlayer. The arrows indicate the direction of the row pairing reconstruction.

From table 3 we can see that the distance between Ir and O atom is comparable to the previous values obtained from the study by Johnson et al.[63] The first iridium interlayer spacing contracted by 0.1% compared to the bulk terminated structure which indicates that oxygen causes the interlayer spacing to expand in comparison to the clean surface structure. The interlayer spacing of the second-to-third layer is 1.93 ± 0.03, which is well within the experimental error, and is essentially the same as the bulk interlayer spacing.

The most significant feature of the oxygen overlayer is the row pairing in the Ir top layer. The movement of Ir atoms was 0.07 Å for this study which is comparable to the value from Johnson et al which was 0.08 Å from both LEED and DFT studies.[63] This reconstruction of the surface Ir atoms seems to have a huge effect over the overlayer structure obtained. Row pairing is only permitted on Ir atoms that do not share an oxygen atom. Previous studies has shown that there is an increase in bond energy on forming the $p(1 \times 2)$ structure which is attributed to the row pairing reconstruction.[63]

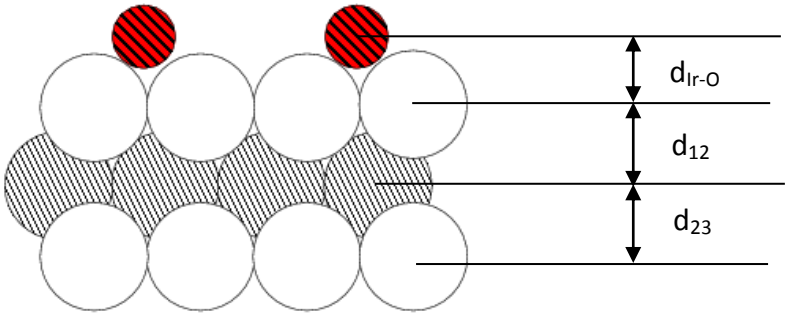

Figure 5.7: Side view of the schematic structure of O on Ir{100} surface.

Table 5.3: Parameters for the best fit structure for O on Ir{100} surface compared with previous structural studies; spacings $d_{\text{Ir-O}}$, d_{12}, and d_{23} are defined in Figure 7.

	d_{Ir-O}	**d_{12}**	**d_{23}**	**R-factor**
This work	1.280 ± 0.04	1.892 ± 0.04 (-0.1%)	1.936 ± 0.03 (1.0%)	0.247
Reference 6 (LEED)	1.301± 0.034	1.898 ± 0.027 (-0.9%)	1.914 ± 0.034 (0.01%)	0.179
Reference 6 (DFT)	1.307	1.931 (-0.4%)	n/a	n/a

The results confirms the theory we had that during phase separation, oxygen from the dissociated NO, adsorbs in a similar manner on the iridium surface as in the case of oxygen adsorbed on Ir{100} surface alone.

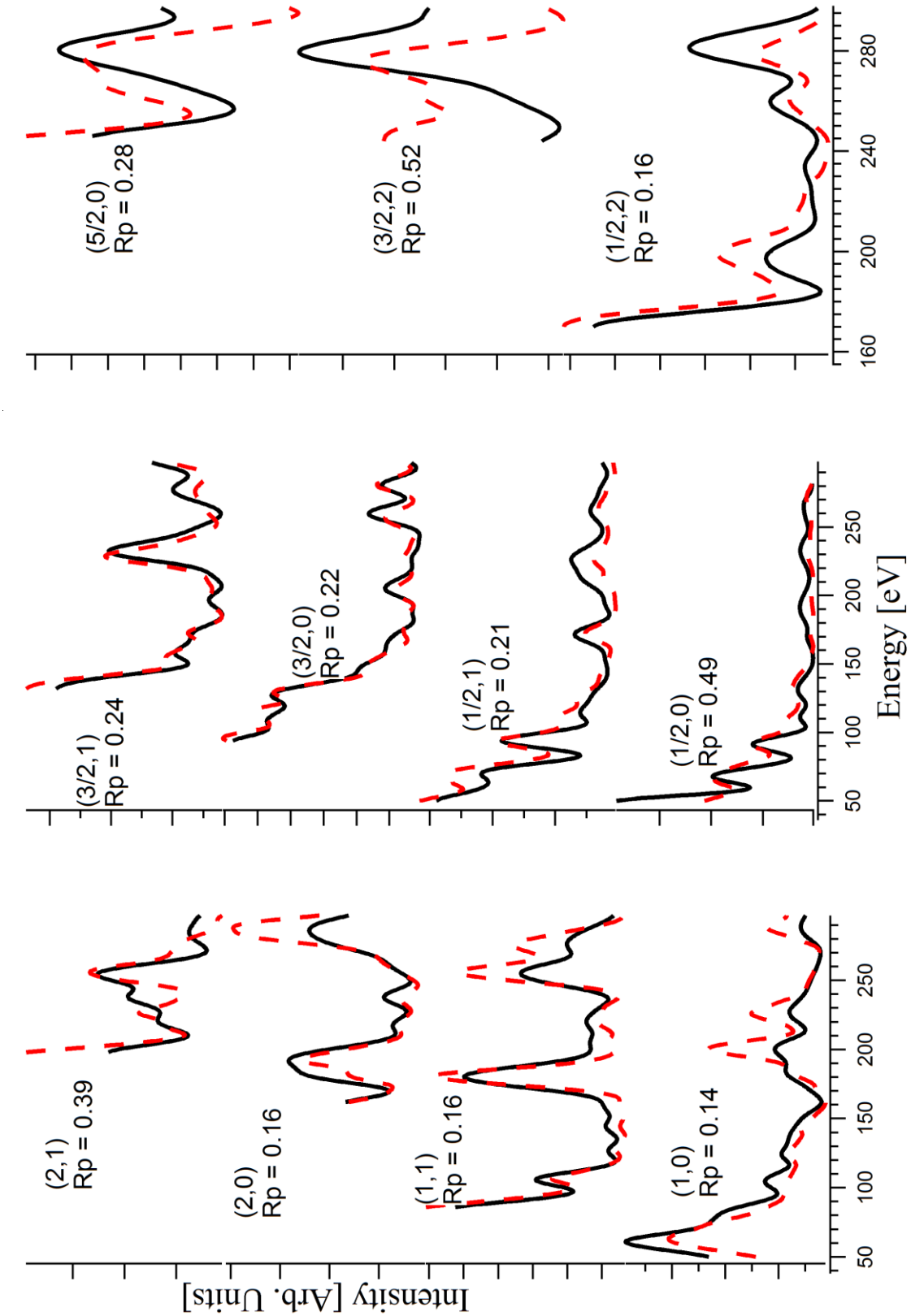

Figure 5.8: Comparison of experimental (solid lines) and theoretical (dashed lines) I-V curves for the structure of O on Ir{100} shown in figure 5.7.

5.3.2.2 Calculations for N only

In this case we did not have information about the overlayer structure that nitrogen forms on the surface of Ir{100}. Thus we had to run calculation using the possible configurations which are shown in figure 5.9. We ran calculations for nitrogen adsorbed on atop, bridge and hollow site for both $p(2 \times 2)$ and $c(2 \times 2)$ overlayer structures. The initial searches were performed over the z parameter and variation of the vibrational amplitudes.

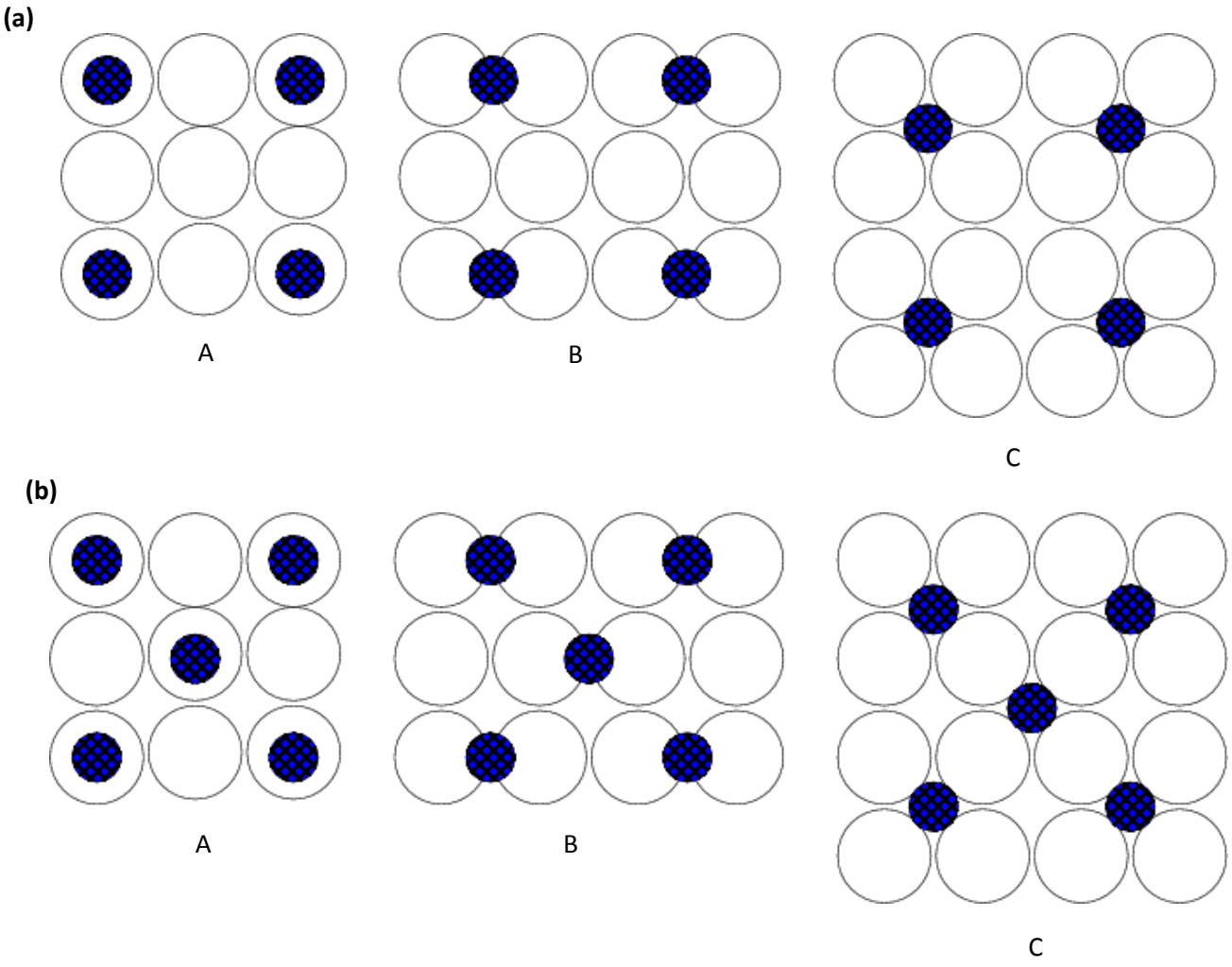

Figure 5.9: Possible configurations of N on Ir{100} for: (a) $p(2 \times 2)$ and (b) $c(2 \times 2)$ overlayers.

Table 5.4: The summary of N only calculations for $p(2 \times 2)$ and $c(2 \times 2)$ with error bars of 11% and 16% respectively

Configurations	$p(2 \times 2)$	$c(2 \times 2)$
A	0.68	0.60
B	0.53	0.42
C	0.72	0.39

The lowest R-factor values obtained for these searches were: 0.68, 0.53 and 0.72 for atop, bridge and hollow site respectively. For the $c(2 \times 2)$ overlayer structure the lowest R-factor values were: 0.60, 0.42 and 0.39 for atop, bridge and hollow site respectively. The results are summarized in table 3. The adsorption on nitrogen on the hollow sites fits the data well and comparing its R-factor to results for the $p(2 \times 2)$ overlayer structure we can see that there is a significant difference. So the next step was to refine the calculation to obtain a better R-factor value.

The calculation for the hollow site which had to lowest R-factor in the preliminary searches was further refined by xyz optimization for nitrogen and the first layer of iridium and variation of the vibrational amplitude. The lowest R-factor value obtained was 0.38 ± 0.06. Further refinements of the calculation were relaxing the second layer and changing the vibrational amplitude. These refinements resulted in a R-factor value of 0.37 ± 0.06; the corresponding side view model and theoretical I-V curves are compared with experimental I-V curves are given in figure 5.10 and 5.11 respectively.

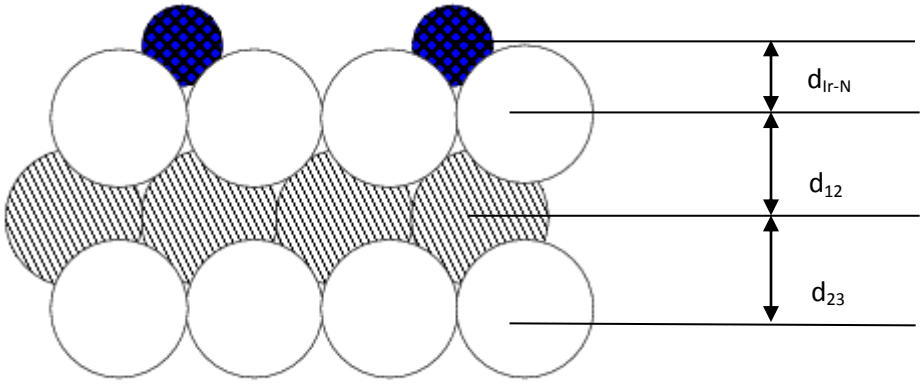

Figure 5.10: Side view of the schematic structure of N on Ir{100} surface.

Table 5.5: Parameters for the best fit structure for O on Ir{100} surface compared with previous structural studies; spacing's $d_{\text{Ir-O}}$, d_{12} , and d_{23} are defined in Figure 11.

	$\mathbf{d_{Ir\text{-}N}}$	$\mathbf{d_{12}}$	$\mathbf{d_{23}}$	**R-factor**
This work (LEED)	0.402 ± 0.050	1.912 ± 0.050 (-0.21%)	1.913 ± 0.040 (-0.15%)	0.37

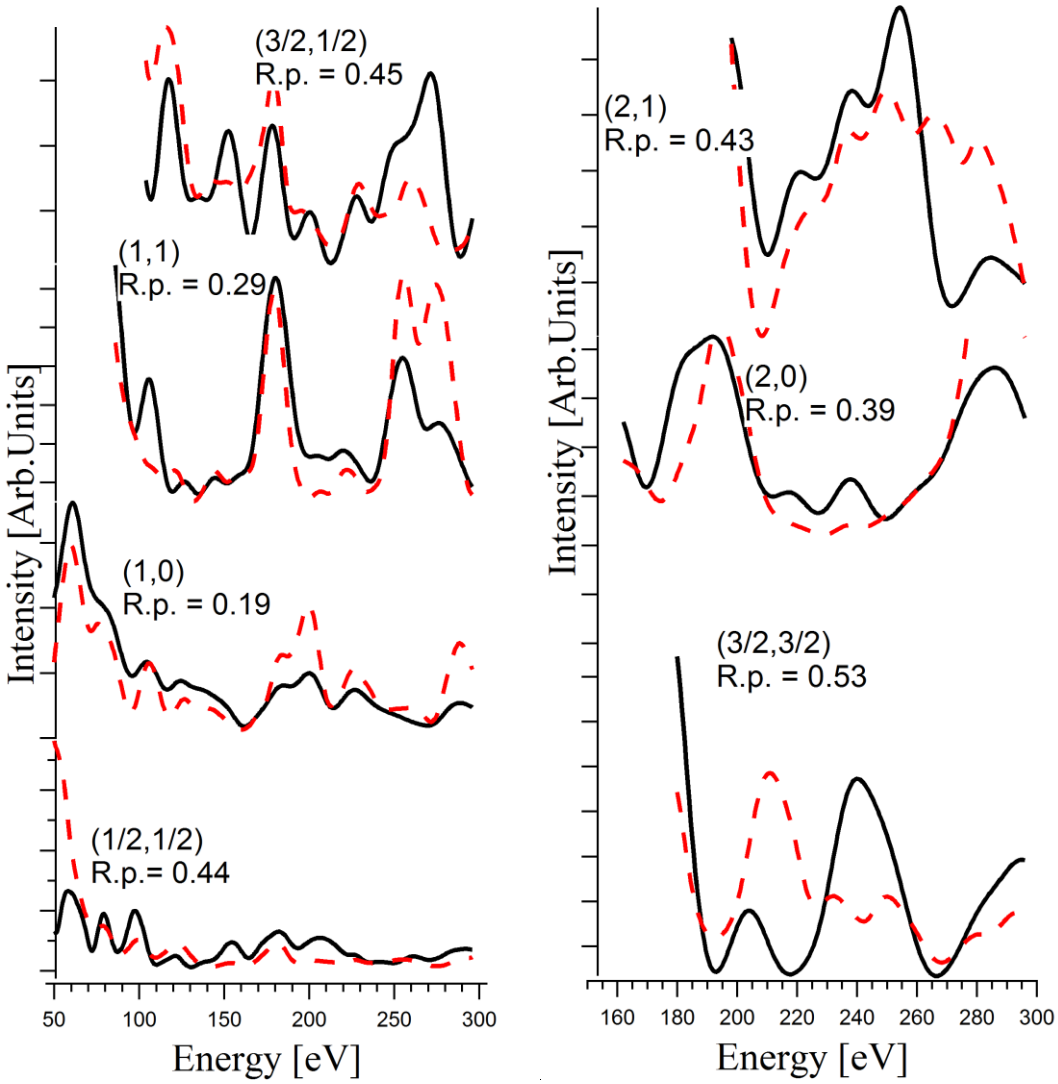

Figure 5.11: Comparison of experimental (solid lines) and theoretical (dashed lines) I-V curves for the structure of N on Ir{100} shown in figure 5.10.

Table 4 shows the parameters for the structure in figure 5.10. The interlayer distance from first-to-second layer and from second-to-third layer are within the experimental error, and is not that different from the bulk terminating structure interlayer spacing. This means that nitrogen results in an expansion of 3.71% in the interlayer spacing between the first and the second layer compared to the clean surface structure.

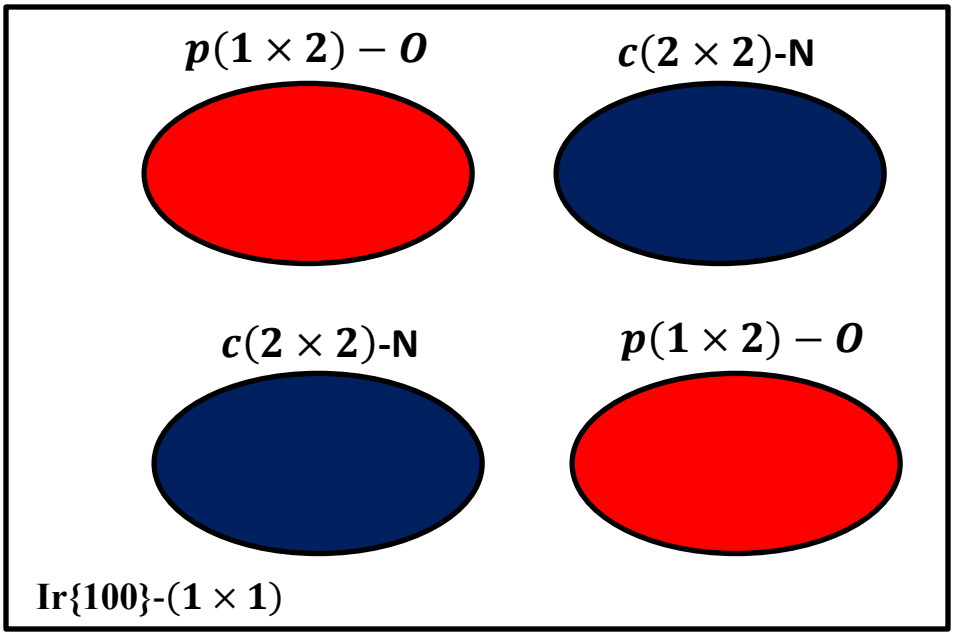

Figure 5.12: A schematic of the islands formed when NO dissociates on Ir{100}-(1×1) surface at 300 K.

What we think is happening on the surface at 300 K, is that NO adsorbs on the Ir{100}-(1×1) surface it dissociates to nitrogen and oxygen, which then separate and form islands as illustrated in figure 5.12. Each island of N and O formed is bigger than 100 Å, because the LEED pattern observed from the experiment has sharp spots, which is indicative of islands that are greater than the transfer width of the LEED instrument. Nitrogen forms $c(2 \times 2)$ islands with N adsorbing on hollow site. And oxygen forms $p(1 \times 2)$ islands with O adsorbing on bridge site. Oxygen behaves as predicted by DFT calculations by Johnson et al and experimentally observed by Lerotholi et al.[17,63] Even at low coverages O prefers forming islands of $p(1 \times 2)$ instead of less dense ordered patterns like a $p(2 \times 2)$.

A program (**c_dom)** which accounts for multiple domains written by Georg Held and discussed in details in chapter 3 was also used for the LEED calculations. The program performs the

appropriate calculations and mixes the I-V curves of the overlapping spots as necessary. The program then produces an output file with correctly averaged I-V curves of the spots of all domains. This program was used for our system and the preliminary results gave an R-factor of 0.38 with an error bar of 11% for a combination of $c(2 \times 2) - N$ and $p(1 \times 2) - O$ islands. This program is work in progress as it has some bugs that need to be sorted out.

5.4 Conclusions

It was found that phase separation fits the experimental data better than phase mixing configuration. The results showed that oxygen and nitrogen form $p(1 \times 2)$ overlayer and $c(2 \times 2)$ on a bridge and hollow adsorption site respectively. These two overlayer when combined result in a $p(2 \times 2)$ overlayer as shown in figure 5.5 above, which is the same overlayer observed during LEED experiments. Reconstruction on the Ir surface stabilized the nitrogen and oxygen structures on the surface. The aim of the study was achieve, which was to determine the structure of dissociated NO on Ir{100} at 200 K.

CHAPTER 6

D-serine on Cu{110}

6.1 Introduction

Bioinorganic interfaces have stimulated great interest in different fields ranging from bio-mineralization, catalysis, nanotechnology to medicine. Amino acids are the commonly used biological molecules for modifying metal interfaces.[65] Amino acids are building blocks of proteins, so studying the manner at which they adsorb on metal surfaces can yield information that can be used to construct sensors and other devices of the same nature.[65] This then broadens the number of their potential applications. Amino acids modify the metal surfaces by introducing chirality onto the surface. Chirality modification can be expressed in one of two ways which are either through a direct enantioselective interaction between adsorbed molecules using molecular recognition or through a global modification of the entire surface by inducing chiral reconstruction or forming molecular superstructures.[66] Therefore the structure, local order and conformation of these biological molecules upon adsorption dictate their interaction with incoming species.[66,67]

The surface science approach for studying and understanding the interactions involved in these biological molecules with inorganic surfaces systems has been developing. Studying the model systems of these biological molecules has provided some insight on how they interact with the metal surfaces.[67] Surface science techniques that have been successful in studying biological systems are DFT, LEED (including CLEED), XPS, RAIRS and STM.[67,68] In spite of the increasing interest in amino acid/ inorganic metal systems and the applications based on them, only a few of these systems have been studied so far. Most work has been on glycine adsorbed on Cu{110} mainly because glycine is the smallest amino acid and is achiral.[67] The logic here is to employ the "bottom-up" approach where simple chiral amino acids are studied first then followed by the more sophisticated amino acids.

The significance of studying chiral molecules adsorbed on metal surfaces is more evident in heterogeneous enantioselective catalysis.[69] This type of catalysis involves using chiral molecules

to modify conventional transition metal catalysts such that one product enantiomer is preferred over the other one by stereo-directing the reactants in the transition state. This is an important process for the pharmaceutical industry because most of their products are chiral. The undesired enantiomers of the products most times have opposite effects compared to the desired enantiomer thus it is important and cost effective to produce the correct enantiomer.

The aim of this study was to use information from DFT calculations as a benchmark for determining the structure of D-serine on Cu{110} surface using the CLEED program. The LEED experimental data and DFT calculations prior to this were obtained from the University of Reading in the United Kingdom (UK).

6.2 D-serine

An organic acid which contains one or more amino (NH_2) substituents may be classified as an amino acid. There are only 20 common amino acids from a vast variety of compounds that are building blocks of proteins. These 20 amino acids are also known as α amino acids, consisting of a base amino group ($-NH_2$), an acidic carboxyl group ($-COO^-$) and an organic side chain which is unique to each α amino acid. These three groups are attached to a tetrahedral bonded carbon atom called an α carbon with hydrogen being the fourth atom bonded to this carbon atom. The relative arrangement of the carboxyl and the amino group where either or both can be involved in forming bonds with the surface, account for the common properties of α amino acids. The physical and chemical properties unique to these amino acids are due to the chemical properties of the side chain.[70]

Glycine and alanine are the two simplest amino acids which contain hydrogen and a methyl group as their side chains respectively. Serine differs from the two simplest amino acids by a hydroxyl (-OH) group side chain as illustrated in figure 6.1. The hydroxyl group of serine is at a β-position in addition to the carboxylic and amino groups. The hydroxyl group of serine makes it a polar α amino acid. It is a naturally occurring amino acid but only the L-serine enantiomer occurs naturally. Serine is a chiral molecule, meaning that its mirror image is not superimposable by any translation or rotation and it has two enantiomers L and D shown in figure 6.1.[70]

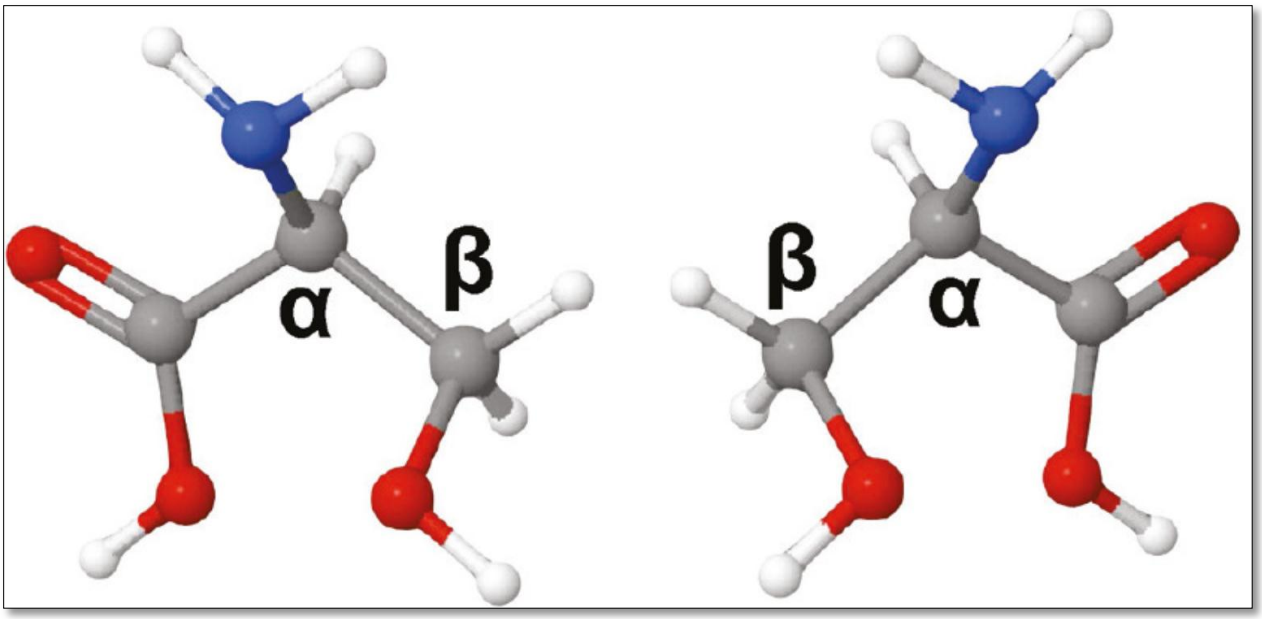

Figure 6.1: Molecular structure models of L and D serine, left and right respectively. The figure was reproduced from reference 68.[68]

These two enantiomers have identical chemical properties except when reacting with asymmetric molecules or polarized light. Our study will focus on the d-serine enantiomer.

6.3 Literature review on D-serine on Cu{110}

Establishing molecular-level understanding of enantioselective and chiral resolution at the organic-inorganic interfaces has been a key challenge in the field of heterogeneous catalysis. A few amino acid adsorption studies have been done on several metal single crystal surfaces including gold, platinum group metals, nickel and copper. The largest study has been on copper mainly because these amino acids form ordered superstructures and adsorb in a well-defined manner which renders them good model systems to be studied using different surface science techniques.[68]

Small amino acids such as glycine and alanine usually adsorb on Cu{110} in their anionic form at room temperature and the anionic form is due to the deprotonated carboxyl group.[71,72] The common structures formed by these amino acids on Cu{110} surface are $p(3 \times 2)$ or $p(4 \times 2)$. There are a few studies that have been reported on serine adsorbed on metal surfaces. Raval and

Barlow reported an ordered LEED pattern for a single coverage of L-serine on Cu{110}, when annealed at 400 K.[67] From their results they suggested that the H-bonding involving the β hydroxyl group has an effect on the ordering of molecules on the surface. Scanning Tunneling Microscopy (STM) studies of L-serine on Cu{110) done by Iwai et al showed "peanut shaped" dimers. Iwai and colleagues suggested the usual bonding to the substrate is through the N of the amino group and the O of the carboxyl group. They further suggested that the dimers form H-bonds between the NH_2 and COO^- groups of the molecules with opposite orientation.[73]

Eralp and colleagues studied the adsorption properties and intermolecular interactions of a L, D and racemic mixture of serine on Cu{100}. They observed the formation of enantiopure dimers for all adsorbate compositions even for the racemic mixture. Serine was adsorbed in its anionic form. Studies of the system using Near-edge X-ray Adsorption Fine Structure (NEXAFS) were used to determine the orientation of the hydroxyl group and they confirm that dimerization occurs through H-bonding interactions.[68] These then resulted in the formation of long-range ordered islands with global chiral superstructures which exhibited the same periodicity for all coverages. The racemic mixture was separated into enantiopure islands with the corresponding superstructures. The same LEED pattern was obtained for both low and high coverages of L and D serine which was (-1 -2; 4 0) and (-1 +2: 4 0) respectively.[68] The results were in agreement with the findings by Raval and Barlow.[74] The superstructure unit cell comprised of eight surface Cu atoms which do not share any symmetry with the Cu{110} surface other than a 180 º rotation. The racemic mixture produced a LEED pattern which was a superposition of the two enantiomer's LEED patterns, with the spots where they overlap stronger than the others. Overall, the study showed that chirality for the system was expressed in three levels: the orientation of the homochiral dimers, the superstructures lattice formed by the dimers and the growth anisotropy of small islands determined using STM.[68]

6.4 Experimental and calculation methods

The experiments that provided the experimental I-V curves were carried out in an ultrahigh vacuum chamber equipped with sputter gun, quadrupole mass spectrometer for TPD measurements and low-current micro channel-plate (MCP) LEED instrument. The sample temperature was measured through a thermocouple attached to the sample holder plates. Serine

was deposited from a glass tube placed in a stainless steel crucible, which was heated to 403 K. The evaporator was mounted behind a gate valve allowing control of the deposition. LEED images were recorded using the MCP-LEED in combination with a standard Video-LEED acquisition system. The MCP-LEED was used because of the electron beam sensitivity of d-serine. The spot intensities were extracted from the LEED images using the MKIV program, which determines the positions of all spots simultaneously and records their intensities even if they cannot be resolved from the background. The total cumulative energy of the extracted spots was 554 eV.[18]

The structure determination was performed using the "CLEED" program. The agreement between the experimental and theoretical I-V curves was quantified using Pendry's R-factor and the error limits for the determined parameters were calculated using the RR-factor method. The hydrogen atoms were ignored in the LEED calculations as is common practice because hydrogen is small thus it does not scatter electrons very well. The Debye temperature was kept at the bulk value (343 K) for all Cu atoms, which corresponds to a radial root mean square (rms) displacement of 0.03 Å. For the O, N and C atoms constant rms displacement values of 0.40 Å were used.

6.5 Results and discussions

The chemistry group at the University of Reading ran DFT calculations of the monomer and dimer d-serine model systems and from their results we managed to find the most suitable models for our CLEED calculation. There were eight models that were developed and run using DFT, of those eight models three of them had the lowest energy which implies the most stable systems. The three lowest energy DFT structures that were used as a starting point for our CLEED calculations are #000, #001 and #005. Their description is just numbers given to the different DFT calculations they bear no significance. Figure 6.2 illustrates the three models considered in our study and the manner at which they bond to the Cu{110} surface and based on theoretical conditions implemented on the DFT calculations.

These three models differ by the interaction between the d-serine molecules and the atoms that bond with the Cu{110} surface. In model #000 the d-serine dimers do not interact with each other. The d-serine molecules are just adsorbed on the Cu{110} surface. In model #001 the

starting geometry (geometry in model #000) was changed with the aim of encouraging intra-molecular H-bonding within the d-serine molecule and for model #005 the geometry is similar to that of #001 but the d-serine molecules are on the opposite corners of the unit cell. The d-serine molecule

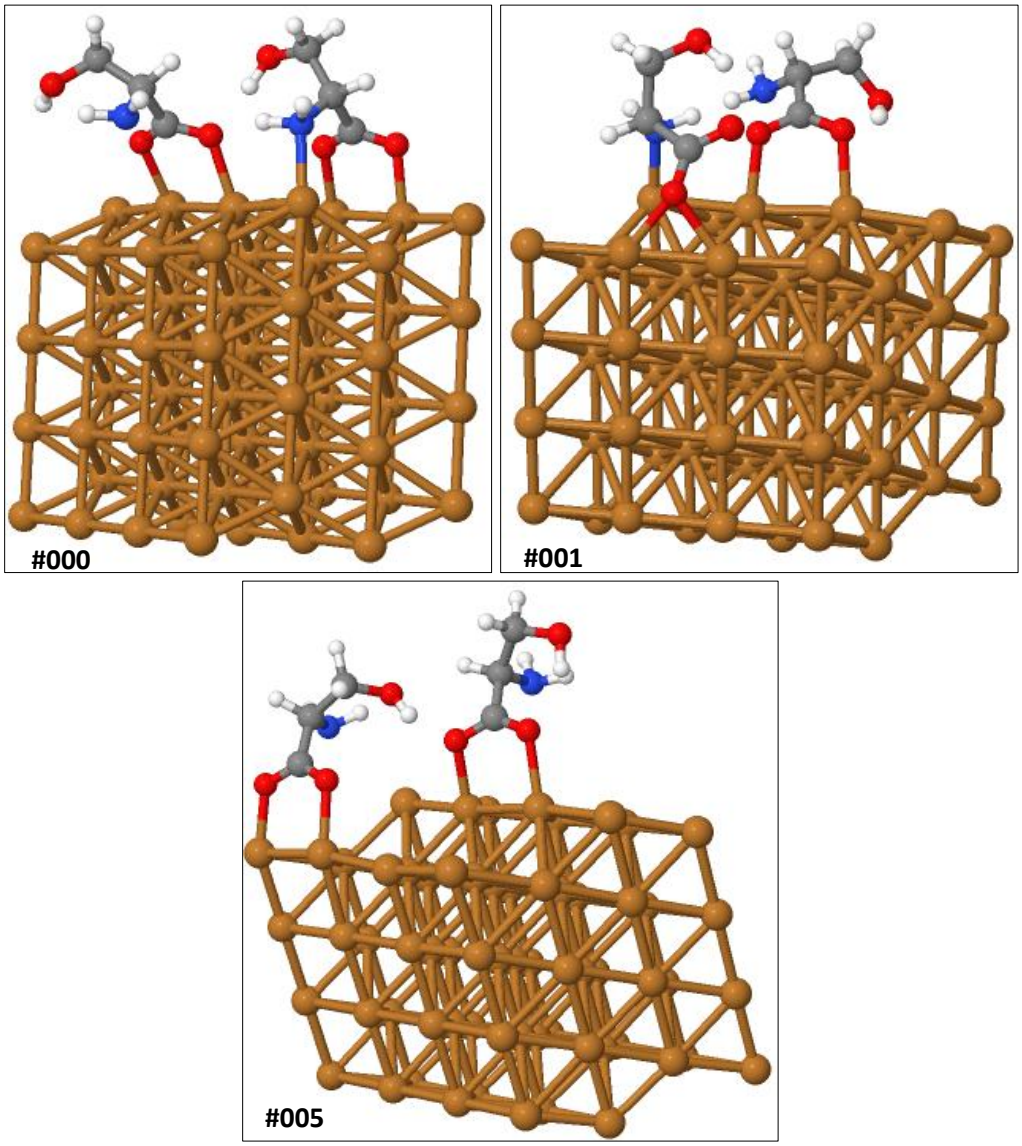

Figure 6.2: The molecular structure of the three models with the lowest energy adsorbed on Cu{110}.

bonds to the surface using the two oxygens of the carboxylate group and the nitrogen of the amino group for structure #000 and #001 in general. The manner at which the two molecules in a unit cell form bonds differs though. For structure #000 one molecule forms bonds using the two

oxygens only while the other molecules bond with two oxygens and nitrogen. In structure #001 one molecule forms two single bonds using one oxygen and nitrogen while the other uses the two oxygens only. For structure #005 both molecules bond to the surface using the carboxylate group oxygens only.

6.5.1 Clean Cu{110} surface

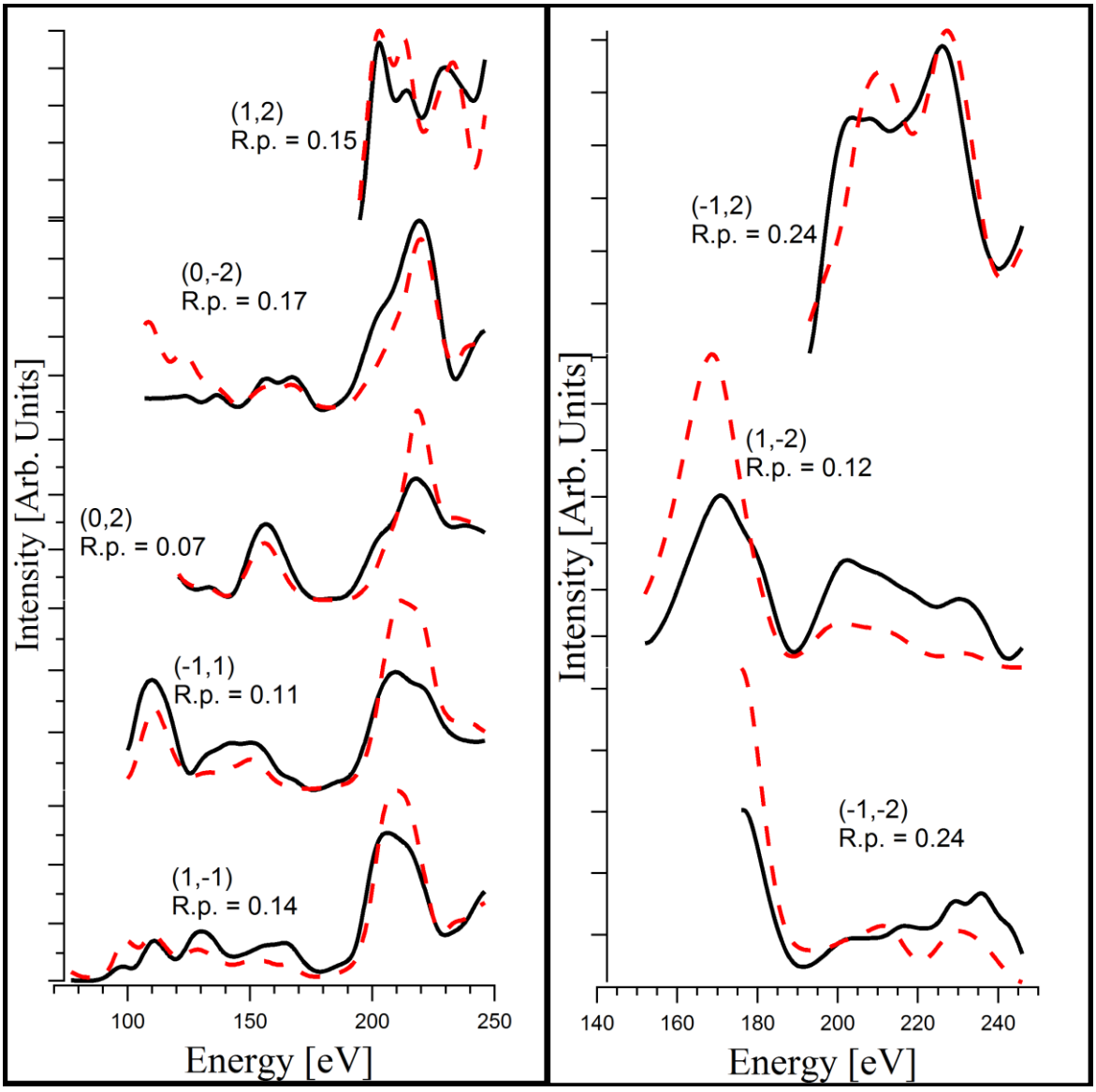

Figure 6.3: Comparison of experimental (solid lines) and theoretical (dashed lines) I-V curves for the structure of Cu{110} shown in figure 6.4.

The initial CLEED calculations was done on the clean Cu{110} surface to confirm the phase using experimental LEED data obtained from the University of Reading. For the clean Cu{110} surface and for d-serine on Cu{110} the scattering from the bulk was calculated using Pendry's layer doubling method, with a bulk interlayer spacing of 1.27 Å. The copper phase shifts were obtained from Held et al.[20]

For the calculation of the clean Cu{110} surface an R-factor of 0.15 ± 0.02 was obtained which is very good since the rule is for a clean metal the R-factor must be less than 0.2. The I-V curves of the Cu{110} spots in figure 6.3 reflect the results obtained. The RR-factor for this calculation was 0.14 and the best value was from the calculation where the three layers of Cu were allowed to relax. The I-V curves show that the theoretical model and the experimental data are in good agreement thus the Cu phase used in the LEED experiment is appropriate. The low R-factor implies that the experimental data is of high quality.

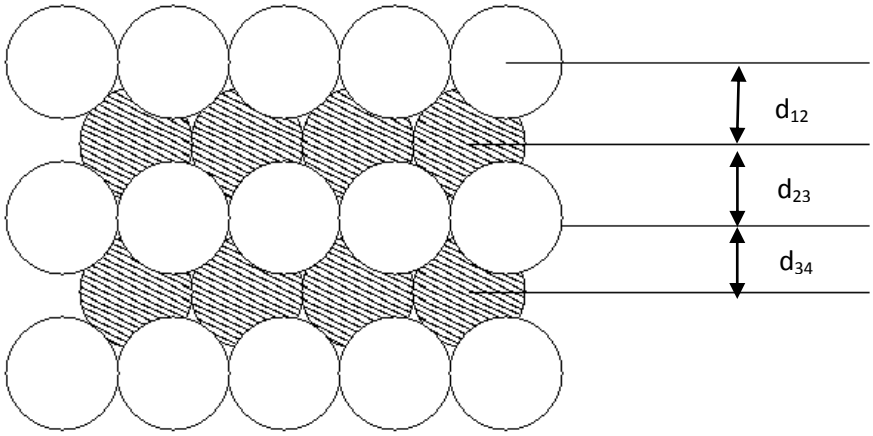

Figure 6.4: Side view of the schematic structure of Cu{110} clean surface.

Table 1: Parameters for the best fit structure of Cu{110} clean surface compared with previous structure Figure 6.4 shows the side view model of the Cu{110} clean structure and the parameters are given in table 1. A first layer contraction of 5.03% was found, which is comparable to previous LEED calculations.[75] The second interlayer spacing expanded by 3.03%, which is not larger compared to 0.43% from literature while the third interlayer spacing shows a contraction of 0.72% with no results were reported in literature. The results of our study are comparable to the previous results with a small difference in the expansion percentage

between the second and third layer. This might due to the sensitivity of the CLEED program to the movement in the z direction.

Table 6.1: Parameters for the best fit structure of Cu{110} clean surface compared with previous structural studies; spacings d_{12} , d_{23} , and d_{34} are defined in Figure 6.4.

	d_{12} (Å)	**d_{23} (Å)**	**d_{34} (Å)**	**R-factor**
LEED this work	1.21 ± 0.03	1.31 ± 0.02	1.28 ± 0.02	0.15 ± 0.02
Expansion or contraction (%)	- 5.04	3.03	0.72	
LEED ref. [76] **Expansion or contraction (%)**	-5.0	0.43	n/a	

6.5.2 D-serine adsorbed on Cu{110}

The unit cell of d-serine adsorbed on Cu{110}comprised of eight Cu atoms and two d-serine molecules as shown in figure 6.5 and these are all the atoms in the CLEED calculation. The figure also shows the growth directions of domains w_2. This model was used to compile the input file for our calculations using coordinates from the DFT calculations. The initial searches (optimization A) that were run for the three models #000, #001 and #005 shown in figure 6.2 were over z parameters only for both the d-serine molecules and the Cu atoms. Each of the d-serine molecules in a unit cell were moved using one parameter. The Cu atoms in a layer were also moved using one parameter. The significance of the latter process was to optimize the bond lengths between the Cu surface and the d-serine molecules. As well as determining the structure that models the experimental data well. The surface layer mean-square vibrational amplitude of the d-serine molecules was 0.10 and 0.03 for Cu atoms. This parameter is used to control the vibration of atoms. The values for this initial searches were 0.62 ± 0.15, 0.50 ± 0.13 and 0.52 ± 0.13 for structures #000, #001 and #005 respectively. From the results obtained, structure #001 model the experimental data better compared to the other two structures even though the R-factor

values are still very high. The number of parameter for these initial searches was four. Therefore the searches were well within the general rule of 1 parameter per 100 eV of the cumulative energy (which is 554 eV).The surface layer mean-square vibrational amplitude of all d-serine was enhanced by increasing it from 0.10 to 0.16.

We then continued to optimize the searches with the aim of decreasing the R-factor and determining the structure that fits the experimental data better. For all three structures the search was further optimized (optimization B) by moving the x, y, z coordinates of all d-serine atoms, and then moving z coordinates of all first layer atoms of Cu separately and moved the atoms of the second with one parameter. The number of parameters for these searches increased to 15, which was a lot considering the cumulative energy we have. The R-factor values for this initial searches were 0.50 ± 0.12, 0.47 ± 0.11 and 0.49 ± 0.12 for #000, #001 and #005 respectively. The results still show that structure #001 models the experimental data better compared to the other two structures.

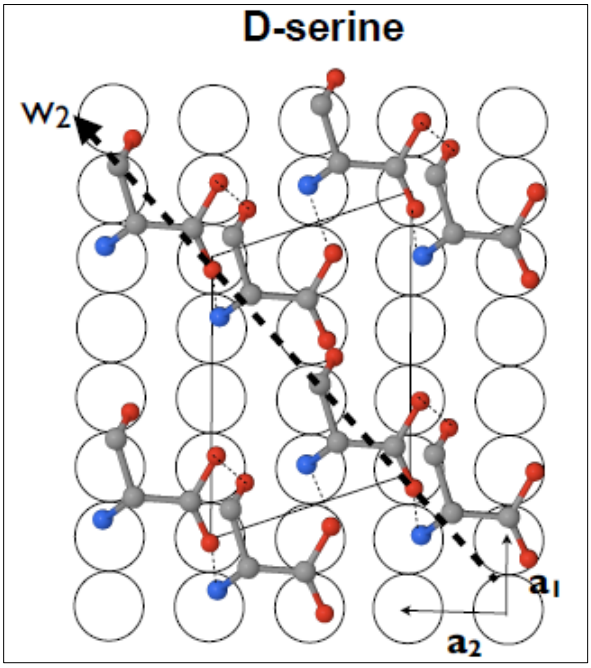

Figure 6.5: Schematic models of d-serine adsorbed on Cu{110} surface unit cell with the growth direction domains w_2 and substrate vectors a_1 and a_2. (b) mimicked row pairing reconstruction on the d-serine unit cell. Figure reproduced from reference 68.

The next step was to continue optimizing (optimization C) structures #000, #001 and #005. Therefore angle search was introduced to the calculations and the lowest values obtained were 0.42 ± 0.10, 0.47 ± 0.12 and 0.48 ± 0.12. The number of parameters for these three searches was 17, which is again high given our cumulative energy. It was then evident from the results obtained that structure #001 models the experimental data better than structure #000 and #005.

The next step was to continue optimizing (optimization D) the three structures further and try to decrease the value. The first parameter to be optimized further was the vibrational amplitudes of the d-serine atoms. The most suitable values were found to be 0.125, 0.14 and 0.160 for C, N, and O respectively. We then introduced reconstruction on the first layer of Cu. This was achieved by pairing atoms in a row and the idea came from the row pairing reconstruction usually found on 100 surfaces. Figure 6.6 illustrates how this reconstruction was achieved by moving the Cu atoms along the y-axis toward each other. Introducing the reconstruction was a trial and error process, with the notion that most of the times adsorbates tend to introduce reconstruction on the surface. Specifically introducing this reconstruction was based on the fact that all systems adsorb with oxygen and from literature, it has been shown to stabilize oxygen on iridium surfaces so the thought was to try it on copper too.[63] The lowest values obtained were 0.51 ± 0.12, 0.40 ± 0.09 and 0.65 ± 0.56.

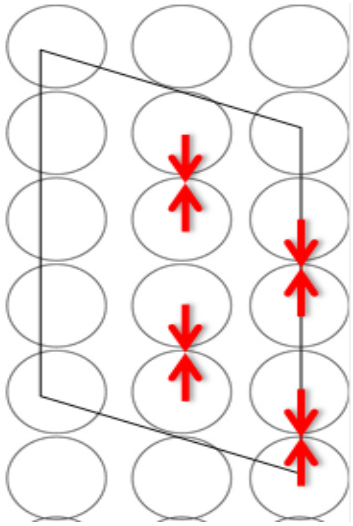

Figure 6.6: Schematic of the Cu atoms in a unit cell and an illustration of the reconstruction introduced in the optimization of structure #001 where the atoms in a row are paired.

Table 6.2: The summary of all optimization results and the RR values are included, which gives the error bar of the calculations.

Optimization	Number of parameters	#000	#001	#005	RR.
A	4	0.62	0.52	0.52	24 %
B	15	0.50	0.47	0.49	24%
C	17	0.42	0.48	0.47	25%
D	15	0.51	0.41	0.65	25 %
E	17	0.67	0.37	0.64	24 %

The last optimization (optimization E) in our calculations was to optimize the angle search and the most suitable values for θ (theta) and Φ phi were 1.0 and 10.0 respectively. The lowest value after all the above optimizations were 0.67 ± 0.16, 0.37 ± 0.09 and 0.64 ± 0.16 for structure #000, #001 and #005 respectively. The results for all optimizations carried out are summarized in table 2 and details of all these searches are given in the appendix section.

From results above structure #001 fits the experimental data better but the R-factor value is not good enough since we need a value > 0.2 and < 0.3. Figure 6.7 shows the comparison of experimental and theoretical I-V curves of d-serine on Cu{110}structure (#001), which reflects the R-factor value obtained. From the I-V curves it is seen that integral order spots have low individual R-factors which is because they are superpositions of diffraction from the metal as well as d-serine adsorbate. On the other hand fractional order spots are only due to diffraction from d-serine only and that explains the higher individual R-factor values compared to integral order spots.

We could not optimize the calculation further than the above because the cumulative energy of the experimental I-V curves is 554 eV, which is not enough. The cumulative energy is not enough because as mentioned before there is a rule where you need at least 100 eV per parameter.

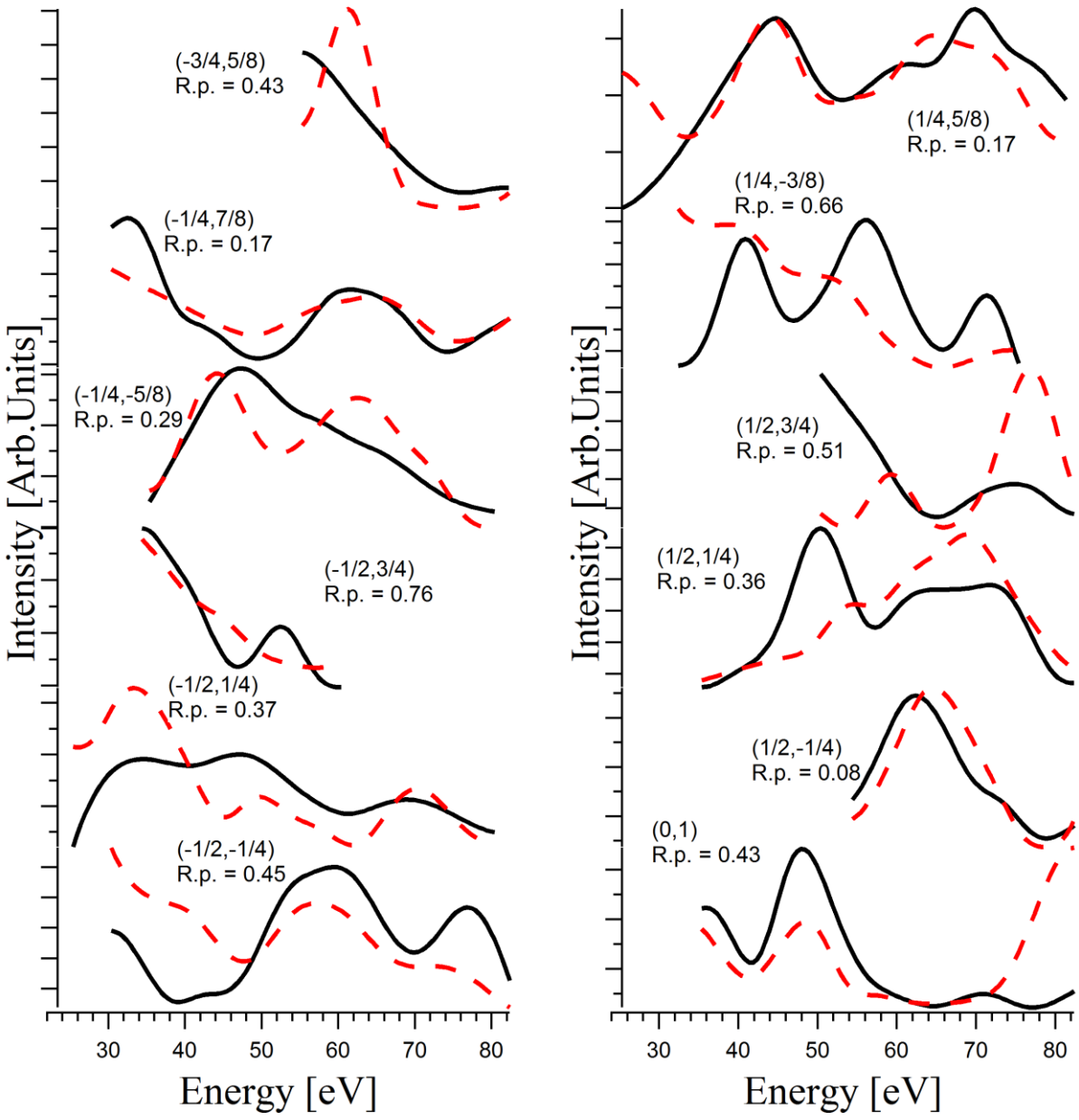

Figure 6.7: Comparison of experimental (solid lines) and theoretical (dashed lines) I-V curves for the structure of d-serine on Cu{110} .

If the latter rule is not obeyed the quality of the calculation decreases. This was a significant limitation for our calculations because for a large molecule such as d-serine, the number of parameters increases (up to 17 parameters) thus we need more experimental I-V curves so as to increase the cumulative energy and accommodate the number of parameters used in the

calculation, because high cumulative energy will allow for better quality calculations and results. More cumulative energy will allow an increase in parameters that are varied in a calculation thus improving the accuracy and reliability of the analysis.

The d-serine system has a big unit cell, and therefore as seen above there are a lot of parameters to optimize during the calculations. This was the main challenge faced in this study, which led to a need for additional experimental data, which we ended up not being able to acquire. Another challenge was the difficulty of extracting experimental I-V curves because most spots are close to each other in the LEED pattern. This makes it difficult to track the spots accurately when extracting I-V curves. It must be noted that the I-V curves used in our calculations were extracted manually as explained in the introduction. Figure 6.8 shows $p(2 \times 2)$ and (-1 +2: 4 0) (pattern for d-serine on Cu{110}) LEED patterns to illustrate the difference in distances between the spots for the two patterns. The figure shows how close the spots are in (-1 +2: 4 0) LEED pattern compared to the $p(2 \times 2)$ used for the NO on Ir{100} system.

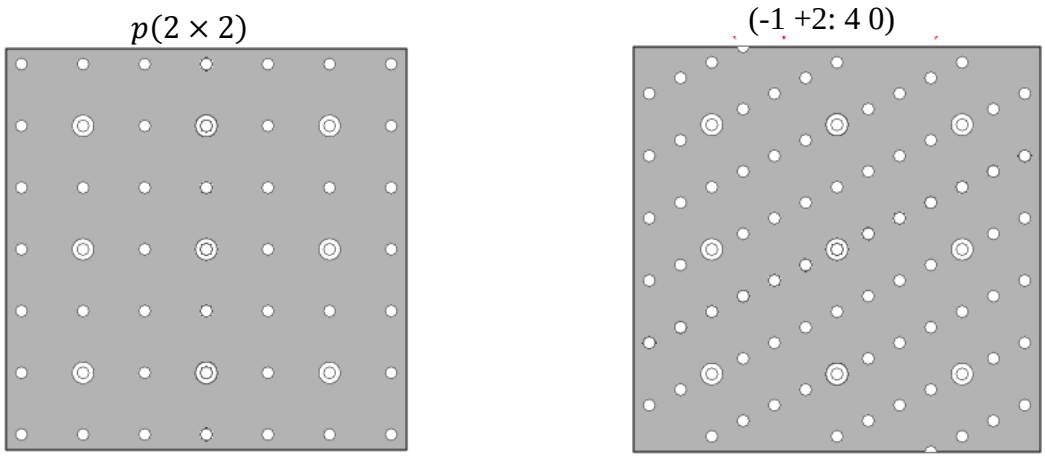

Figure 6.8: A schematic showing $p(2 \times 2)$ and (-1 +2: 4 0) LEED patterns, to illustrate how close to each other spots are in the (-1 +2: 4 0) compared to the $p(2 \times 2)$ LEED pattern.

6.5.2.1 Conclusions and future work

In conclusion we successfully managed to determine the best d-serine structure between structures #000, #001 and #005 from the DFT calculation. Structure #001 fitted the experimental data better and we also managed to optimize the R-factor to 0.37 ± 0.09 which was the best result obtained but the R-factor is still high. The result is within the error bar given due to the

low cumulative energy of the I-V curves used. The model structure #001 bonds with the Cu surface using two oxygens of the carboxylate group and the nitrogen of the amino group. The same result was obtained by Eralp et al.[68] The results obtained imply that d-serine molecules adsorbed on Cu{110} surface favour intra molecular bonding. Similar results were observed from the Eralp et al study also where intra-dimer hydrogen-bonding was observed between β-OH and NH_2 groups and the two oxygen atoms of the same carboxylate group.[68] The study also mentioned that both the intra-dimer and inter-dimer bonds are equally important in stabilizing the d-serine structure on the Cu{110} surface. Future work would be to obtain more experimental I-V curves so as to increase our cumulative energy and then optimize our calculations to a desired R-factor value less than 0.3. This additional data set will be collected at several angles of incidence of the electron beam with respect to the sample in order to increase the energy range. A similar approach was applied on a study of glycine adsorbed on Pd{111} surface and conclusive results were obtained.[18]

Appendix

Tables below contain information both for phase mixing and phase separation for the NO on Ir{100} system.

Table A.1 Mixed phase N+O

ATOM	**Ir(100)-p(2x2)-N+O (atop)**			
	X		**X**	
N	0.000	N	0.000	N
O	2.705	O	2.705	O
First Layer				
Ir (1)	0.000	Ir (1)	0.000	Ir (1)
Ir (2)	2.705	Ir (2)	2.705	Ir (2)
Ir(3)	0.000	Ir(3)	0.000	Ir(3)
Ir(4)	2.705	Ir(4)	2.705	Ir(4)
Second Layer				
Ir (A)	1.352	Ir (A)	1.352	Ir (A)
Ir (B)	4.057	Ir (B)	4.057	Ir (B)
Ir (C)	1.352	Ir (C)	1.352	Ir (C)
Ir (D)	4.057	Ir (D)	4.057	Ir (D)
Bulk				
Ir (I)	0.000	Ir (I)	0.000	Ir (I)
Ir (II)	1.352	Ir (II)	1.352	Ir (II)
Rp		0.7045		
RR		0.116692		

Model	**R.p**	**RR**	**dr 1**
2	0.7068	0.116979	0.042
3	0.761411	0.116979	0.080
4	0.762403	0.116979	0.0120 AND 0.080
5	0.751931	0.117141	0.120
6	0.780797	0.117141	0.030

ATOM	**Ir(100)-p(2x2)-N+O (bridge)**			
	X	**Y**	**Z**	

N	0.000	0.000	5.310	
O	2.705	0.000	5.241	
First Layer				
Ir (1)	0.000	0.000	3.832	
Ir (2)	2.705	0.000	3.832	
Ir(3)	0.000	2.705	3.832	
Ir(4)	2.705	2.705	3.832	
Second Layer				
Ir (A)	1.352	1.352	1.916	
Ir (B)	4.057	1.352	1.916	
Ir (C)	1.352	4.057	1.916	
Ir (D)	4.057	4.057	1.916	
Bulk				
Ir (I)	0.000	0.000	0.000	
Ir (II)	1.352	1.352	-1.916	
Rp		0.740652		
RR		0.117291		

Model	**R.p**	**RR**	**dr 1**
2	0.752115	0.117292	0.042
3	0.746022	0.117292	0.050
4	0.751351	0.117292	0.080
5	0.784754	0.117292	0.120

ATOM	**Ir(100)-p(2x2)-N+O (hollow)**			
	X	**Y**	**Z**	
N	0.000	0.000	4.423	
O	2.705	0.000	4.354	
First Layer				
Ir (1)	0.000	0.000	3.832	
Ir (2)	2.705	0.000	3.832	
Ir(3)	0.000	2.705	3.832	
Ir(4)	2.705	2.705	3.832	
Second Layer				
Ir (A)	1.352	1.352	1.916	
Ir (B)	4.057	1.352	1.916	
Ir (C)	1.352	4.057	1.916	
Ir (D)	4.057	4.057	1.916	
Bulk				
Ir (I)	0.000	0.000	0.000	
Ir (II)	1.352	1.352	-1.916	

Rp	0.712097
RR	0.117091

Model	**R.p**	**RR**	**dr 1**
1	0.761510	0.118262	0.042
2	0.785039	0.116979	0.050
3	0.714225	0.119283	0.060
5	0.748213	0.117292	0.080

Table A.2 Phase Separation N only c(2x2)

ATOM	**Ir(100)-c(2x2)-N (atop)**			
	X	**Y**	**Z**	
N	0.000	0.000	5.802	
First Layer				
Ir (1)	0.000	0.000	3.832	
Ir (2)	0.000	2.705	3.832	
Second Layer				
Ir (A)	-1.352	1.352	1.916	
Ir (B)	1.352	1.352	1.916	
Bulk				
Ir (I)	0.000	0.000	0.000	
Ir (II)	1.352	1.352	-1.916	
Rp		0.601075		
RR		0.160402		

Model	**R.p**	**RR**	**dr 1**
1	0.622283	0.160502	0.042
2	0.616549	0.160663	0.060
4	0.6025	0.160132	0.120

Model 5.12

ATOM	**Ir(100)-c(2x2)-N (hollow)**			
	X	**Y**	**Z**	dr1
N	0.000	0.000	4.423	0.120
First Layer				
Ir (1)	0.000	0.000	3.832	0.042

Ir (2)	0.000	2.705	3.832	0.042
Second Layer				
Ir (A)	-1.352	1.352	1.916	0.042
Ir (B)	1.352	1.352	1.916	0.042
Bulk				
Ir (I)	0.000	0.000	0.000	0.042
Ir (II)	1.352	1.352	-1.916	0.042
Rp		0.372552		
RR		0.160402		

ATOM	**Ir(100)-c(2x2)-N (bridge)**			
	X	**Y**	**Z**	
N	0.000	0.000	5.310	
First Layer				
Ir (1)	0.000	0.000	3.832	
Ir (2)	0.000	2.705	3.832	
Second Layer				
Ir (A)	-1.352	1.352	1.916	
Ir (B)	1.352	1.352	1.916	
Bulk				
Ir (I)	0.000	0.000	0.000	
Ir (II)	1.352	1.352	-1.916	
Rp		0.420926		
RR		0.160402		

Model	**R.p**	**RR**	**dr 1**
1	0.478205	0.162351	0.042
2	0.597584	0.160401	0.060
3	0.479367	0.160333	0.120
4.1	0.460761	0.160250	0.080
5	0.477937	0.160023	0.050

Table A.3 Phase separation p(2x2)

ATOM	Ir(100)-p(2x2)-N (atop)			
	X	**Y**	**Z**	
N	0.000	0.000	5.802	
First Layer				
Ir (1)	0.000	0.000	3.832	
Ir (2)	2.705	0.000	3.832	
Ir(3)	0.000	2.705	3.832	
Ir(4)	2.705	2.705	3.832	
Second Layer				
Ir (A)	1.352	1.352	1.916	
Ir (B)	4.057	1.352	1.916	
Ir (C)	1.352	4.057	1.916	
Ir (D)	4.057	4.057	1.916	
Bulk				
Ir (I)	0.000	0.000	0.000	
Ir (II)	1.352	1.352	-1.916	
Rp		0.686168		
RR		0.116692		

Model	R.p	RR	dr 1
1	0.707361	0.118262	0.042
2	0.704471	0.118431	0.050
3	0.707131	0.118262	0.060
4	0.721970	0.118095	0.080

ATOM	Ir(100)-p(2x2)-N (bridge)			
	X	**Y**	**Z**	
N	0.000	0.000	5.310	
First Layer				
Ir (1)	0.000	0.000	3.832	
Ir (2)	2.705	0.000	3.832	
Ir(3)	0.000	2.705	3.832	
Ir(4)	2.705	2.705	3.832	
Second Layer				
Ir (A)	1.352	1.352	1.916	
Ir (B)	4.057	1.352	1.916	
Ir (C)	1.352	4.057	1.916	
Ir (D)	4.057	4.057	1.916	
Bulk				
Ir (I)	0.000	0.000	0.000	

Ir (II)	1.352	1.352	-1.916	
Rp		0.534595		
RR		0.117762		

Model	**R.p**	**RR**	**dr 1**
1	0.688272	0.117267	0.042
2	0.689968	0.117104	0.050
3	0.680006	0.117762	0.080
5	0.690243	0.117141	0.030
6	0.699340	0.116979	0.020

ATOM	**Ir(100)-p(2x2)-N (hollow)**			
	X	**Y**	**Z**	
N	0.000	0.000	4.423	
First Layer				
Ir (1)	0.000	0.000	3.832	
Ir (2)	2.705	0.000	3.832	
Ir(3)	0.000	2.705	3.832	
Ir(4)	2.705	2.705	3.832	
Second Layer				
Ir (A)	1.352	1.352	1.916	
Ir (B)	4.057	1.352	1.916	
Ir (C)	1.352	4.057	1.916	
Ir (D)	4.057	4.057	1.916	
Bulk				
Ir (I)	0.000	0.000	0.000	
Ir (II)	1.352	1.352	-1.916	
Rp		0.728127		
RR		0.118095		

Model	**R.p**	**RR**	**dr 1**
1	0.747850	0.118431	0.042
2	0.739728	0.118600	0.050
3	0.737281	0.118431	0.060
4	0.732098	0.118431	0.080

Table A.4 Phase separation p(2x1) O

ATOM	**Ir(100)-p(2x1)-O (bridge)**			
	X	**Y**	**Z**	dr1
O	0.000	0.000	5.098	0.08

First Layer				
Ir (1)	1.352	0.000	3.832	0.042
Ir (2)	4.057	2.705	3.832	0.042
Second Layer				
Ir (A)	0.000	1.352	1.916	0.038
Ir (B)	2.705	1.352	1.916	0.038
Bulk				
Ir (I)	1.352	0.000	0.000	
Ir (II)	0.000	1.352	-1.916	
Rp		0.246976		
RR		0.134459		

Model	**R.p**	**RR**	**dr 1**
1	0.416547	0.134840	0.042
2	0.394808	0.134649	0.050
3	0.385336	0.134269	0.060
3.1	0.289595	0.134269	0.10
3.2	0.247251	0.134364	0.08
4	0.369932	0.134459	0.108
5	0.820273	0.136697	0.108 (Evah's best fit)
6	0.855588	0.133780	0.108 (Evah's best fit and moved x coordinates)
7	0.369487	0.134269	0.10

D-serine on Cu{110}

Table A.5: A summary of the DFT calculation with description and the total energy of each model ran.

# Calculation	Description	Total Energy (eV)
000	D-Serine Dimer on optimized Cu{110} slab	-80704.998
001	D-Serine Dimer on optimized Cu{110} slab - starting geometry change to encourage intra molecular H bonding	-80705.085
002	D-Serine Dimer on optimized Cu{110} slab - starting geometry with NH2 group facing each other	-80704.832
005	D-Serine Dimer on optimized Cu{110} slab as in #001 with molecules at opposite corners of unit cell	-80705.092
008	D-Serine Dimer on optimized Cu{110} slab as in #001 with molecules at opposite corners of unit cell with one molecule oriented along the diagonal of 4 neighbouring Cu atoms	-80704.834
009	D-Serine Dimer on optimized Cu{110} slab with molecules lying side by side	-80705.325
010	D-Serine Dimer on optimized Cu{110} slab, starting geometry based on optimum monomer geometry	-80704.572
011	D-Serine Dimer on optimized Cu{110} slab, starting geometry based on optimum monomer geometry	-80704.861

From table 1 it is evident that calculation #000, #001 and #005 had the lowest energies which are the three models we used in our CLEED calculations.

Table A.6: Summary of CLEED program calculations for structure #001. The d-serine structure with the lowest R-factor of the three structures used from DFT calculations.

Structure #001					
Search no.	R.p.	RR.	energy overlap	dr 1 (vibrational amplitude	Comments
1	0.50463	0.25135	506.5	0.145	used 0.145 vib.amp for all serine molecules
2	0.52208	0.24795	520.6	0.16	
3	0.47726	0.25324	499	0.160 and 0.14	vib.amp of 0.16 for all serine atoms excluding N which was 0.14
4	0.57642	0.2448	534 (shift 3.5)	0.060 nd 0.040	0.060 for all serine atoms except N which is 0.040
5	0.59053	0.2448	534 (shift 3.5)	0.063 and 0.043	0.063 for all serine atoms except N which is 0.043
6	0.58408	0.24001	555.5 (-1.0)	0.04 and 0.06	
7	0.52699	0.24143	549	0.08 and 0.10	
8	0.46674	0.25223	503	0.140 and 0.160	
9	0.45994	0.25135	506	0.140 and 0.160	1st O
10	0.44695	0.25135	506	0.140 and 0.160	2nd O
11	0.41681	0.25135	506.5	0.140 and 0.160	3rd O
12	0.42474	0.25135	506.5	0.140 and 0.160	1st and 3rd O
13	0.42538	0.25135	506.5	0.140 and 0.160	2nd and 3rd O
14	0.45616	0.25135	506.5	0.140 and 0.160	1st and 2nd O
15	0.42418	0.25135	506.5	0.10, 0.140 and 0.160	C, O 3RD and N
16	0.40996	0.25135	506.5	0.120, 0.140 and 0.160	C, O 3RD and N
17	0.4109	0.2513	506.5	0.130, 0.140 and	

	5	5		0.160	
18	0.40983	0.25135	506.5	0.125, 0.140 and 0.160	
18.1	0.40893	0.25135	506.5	0.125, 0.140 and 0.160	angle search 2.96 and 295.96
18.2	0.42126	0.25049	510	0.125, 0.140 and 0.160	angle search 0.50 and 1.0
18.3	0.41179	0.25049	510	0.125, 0.140 and 0.160	angle search 1.0 and 5.0
18.4	0.4114	0.25135	506.5	0.125, 0.140 and 0.160	no angle search 8 parameters
18.5	0.41053	0.25135	506.5	0.125, 0.140 and 0.160	angle search 3.96 and 295.7
18.6	0.38827	0.25135	506.5 (shift 8.0)	0.125, 0.140 and 0.160	row pairng in the first layer
18.7	0.38806	0.25135	506.5 (shift 8.0)	0.125, 0.140 and 0.160	reconstruction in the first layer and angle search (3.96, 295.96)
18.8	0.37715	0.25049	510 (shift 7.5)	0.125, 0.140 and 0.160	reconstruction in the first layer and angle search (1.0, 5.0)
18.9	0.37103	0.25049	510 (shift 7.5)	0.125, 0.140 and 0.160	reconstruction in the first layer and angle search (1.0, 10.0)
18.10	0.37715	0.25049	510 (shift 7.5)	0.125, 0.140 and 0.160	reconstruction in the first layer and angle search (1, 5)
18.11	0.37524	0.25049	510 (shift 7.5)	0.125, 0.140 and 0.160	reconstruction in the first layer and angle search (1.5, 8)
18.12	0.3769	0.25049	510 (shift 7.5)	0.125, 0.140 and 0.160	reconstruction in the first layer and angle search (1.74, -59.34)
18.13	0.38387	0.25049	510 (shift 7.5)	0.125, 0.140 and 0.160	reconstruciont in the first layer and angle search (1.0, 20.0)
18.14	0.41226	0.25049	510 (shift 7.5)	0.125, 0.140 and 0.160	reconstruction in the first layer and angle search (1.0, 30.0)
18.15	0.37475	0.25135	506.5	0.125, 0.140 and 0.160	reconstruction in the firs layer and angle search (1.0, 15.0)
18.16	0.3839	0.25135	506.5	0.125, 0.140 and 0.160	reconstruction in the firs layer and angle search (1.75, -60.0)

References

(1) Duke, C. B. The Birth and Evolution of Surface Science: Child of the Union of Science and Technology. *Proc. Natl. Acad. Sci. U. S. A.* **2003**, *100* (7), 3858–3864.

(2) Somorjai, G. A. Modern Surface Science and Surface Technologies: An Introduction. *Chem. Rev.* **1996**, *96* (4), 1223–1236.

(3) Titmuss. S, Wander. A, King. D. Reconstruction of Clean and Adsorbate-Covered Metal Surfaces. *Chem. Rev.* **1996**, *96* (4), 1291–1306.

(4) Ammer. C, M. A. van Hove, S. Y. T. Surface Crystallography by LEED Springer Series in Chemical Physics,. *Krist. und Tech.* **1979**, *14* (12), 1520–1520.

(5) Woodruff, D. P.; Delchar, T. A. *Modern Techniques of Surface Science*; Cambridge University Press, **1994**.

(6) Somorjai, G. A. The Surface Science of Heterogeneous Catalysis. *Surf. Sci.* **1994**, *299–300*, 849–866.

(7) Bonzel, H. . The Role of Surface Science Experiments in Understanding Heterogeneous Catalysis. *Surf. Sci.* **1977**, *68*, 236–258.

(8) Goodman, D. W. Model Studies in Catalysis Using Surface Science Probes. *Chem. Rev.* **1995**, *95* (3), 523–536.

(9) Attard, G.; Barnes, C. *Surfaces (Oxford Chemistry Primer)*; Oxford University Press, **1998**.

(10) Masel, R. I. *Principles of Adsorption and Reaction on Solid Surfaces*, 1st ed.; John Wiley & Sons: New York, Toronto, **1996**.

(11) Brundle, C.R, Baker, A. D. *Electron Spectroscopy: Theory, Techniques and Application*, 2nd ed.; Academic Press: London. New York, San Francisco, **1978**.

(12) Niemantsverdriet, J. W. *Spectroscopy in Catalysis: An Introduction*, Third.; Wiley-VCH: Weinheim, **2007**.

(13) Ramsvik, T. Surface Science Studies of Cobalt and Rhodium Single Crystal Surfaces. Thesis, University of Trondheim, **2001**.

(14) Schroeder, S.; Gottfried, M. Temperature-Programmed Desorption (TPD) Thermal Desorption Spectroscopy (TDS). *Userpage.Chemie.Fu-Berlin.De* **2002**, 1–22.

(15) Woodruff, D. P.; Delchar, T. A. *Modern Techniques of Surface Science*; Cambridge University Press: Cambridge, **1994**.

(16) Redhead, P. A. Thermal Desorption of Gases. *Vacuum* **1962**, *12* (4), 203–211.

(17) Lerotholi, T. J.; Held, G.; King, D. A. Phase Mixing and Phase Separation Accompanying the Catalytic Oxidation of CO on Ir{1 0 0}. *Surf. Sci.* **2007**, *601* (5), 1285–1295.

(18) Zheleva, Z. V. Surface Crystallography of Complex and Disordered Surfaces. Thesis,

University of Reading, **2007**.

(19) Pendry, J. B. *Low Energy Electron Diffraction: The Theory and Its Application to Determination of Surface Structure*; Academic Press, **1974**.

(20) Held, G. An Introduction to CLEED Structural Analysis by LEED. Cambridge University Press: Reading, UK 2015, pp 1–108.

(21) Starke, U.; Pendry, J. B.; Heinz, K. Diffuse Low-Energy Electron Diffraction. *Surf. Sci.* **1996**, *52* (2), 53–24.

(22) van Hove, M. A.; Tong, S. Y. *Surface Crystallography by LEED: Theory, Computation and Structural Results*; Springer Science & Business Media, **2012**.

(23) Vitos, L.; Ruban, A. V.; Skriver, H. L.; Kollár, J. The Surface Energy of Metals. *Surf. Sci.* **1998**, *411*, 186–202.

(24) Held, G. Surface Structure Summer School Presentation. Belo Horizonte **2013**.

(25) Hayfield, P. C. S. Platinised Titanium Electrodes for Cathodic Protection. *Platin. Met. Rev.* **1983**, *27* (1), 2–8.

(26) Tauster, S. J.; Fung, S. C.; Garten, R. L. Strong Metal-Support Interactions. Group 8 Noble Metals Supported on Ti02. *J. Am. Chem. Soc.* **1978**, *1*.

(27) Vannice, A.; Chou, P. Heats of Adsorption of H2 and CO on a Pd/TiO2 "S.M.S.I."(Strong Metal Support Interaction) Catalyst. *J. Chem. Soc. Chem. Commun.* **1984**, *23* (23), 1590–1591.

(28) Vannice, M. A.; Hasselbring, L. C.; Sen, B. Metal-Support Effects on H2 and CO Heats of Adsorption on TiO2- Supported Platinum. *J. Phys. Chem. C* **1985**, *89*, 2972–2973.

(29) Vannice, M. A.; Sudhakar, C. A Model for the Metal-Support Effect Enhancing CO Hydrogenation Rates over Pt-TiO2 Catalysts. *J. Phys. Chem. C* **1984**, *88* (12), 2429–2432.

(30) Tauster, S. J.; Fung, S. C.; Baker, R. T.; Horsley, J. A. Strong Interactions in Supported-Metal Catalysts. *Science* **1981**, *211*, 4487.

(31) Wang, Z.-J.; Yan, Z.; Liu, C.-J.; Goodman, D. W. Surface Science Studies on Cobalt Fischer–Tropsch Catalysts. *ChemCatChem* **2011**, *3*, 551–559.

(32) Tauster, S. J. Strong Metal-Support Interactions. **1987**, *20* (3), 389–394.

(33) Xu, X.; He, J.-W.; Wayne Goodman, D. A Surface Spectroscopic Study of Metal-Support Interactions: Model Studies of Copper on Thin SiO2 Films. *Surf. Sci. Lett.* **1993**, *284* (1–2), A279.

(34) Puskas, I.; Fleisch, T. H.; Full, P. R.; Kaduk, J. a.; Marshall, C. L.; Meyers, B. L. Novel Aspects of the Physical Chemistry of Co/SiO2 Fischer-Tropsch Catalyst Preparations. The Chemistry of Cobalt Silicate Formation during Catalyst Preparation or Hydrogenation. *Appl. Catal. A Gen.* **2006**, *311* (1–2), 146–154.

(35) Sexton, B. A.; Hughes, A. E.; Foger, K. XPS Investigation of Strong Metal-Support Interactions on Group Illa-Va Oxides. *J. Catal.* **1982**, *77*, 85–93.

(36) Saib, A. M.; Claeys, M.; van Steen, E. Silica Supported Cobalt Fischer–Tropsch Catalysts: Effect of Pore Diameter of Support. *Catal. Today* **2002**, *71* (3–4), 395–402.

(37) Rane, S.; Borg, Ø.; Yang, J.; Rytter, E.; Holmen, A. Effect of Alumina Phases on

Hydrocarbon Selectivity in Fischer-Tropsch Synthesis. *Appl. Catal. A Gen.* **2010**, *388* (1–2), 160–167.

(38) Mogorosi, R. P.; Fischer, N.; Claeys, M.; Van Steen, E. Strong-Metal-Support Interaction by Molecular Design: Fe-Silicate Interactions in Fischer-Tropsch Catalysts. *J. Catal.* **2012**, *289*, 140–150.

(39) Greuter, F.; Heskett, D.; Plummer, E. W.; Freund, H.-J. Chemisorption of CO on Co(0001). Structure and Electronic Properties. *Phys Rev. B* **1983**, *27* (12).

(40) Toomes, R. L.; King, D. A. Coadsorption and Surface Compound Formation in the Interaction of CO2 with K on CO{101??0}. *Surf. Sci.* **1996**, *349* (1), 65–80.

(41) Geerlings, J. J. C.; Zonnevylle, M. C.; de Groot, C. P. M. Structure Sensitivity of the Fischer-Tropsch Reaction on Cobalt Single Crystals. *Surf. Sci. Lett.* **1991**, *241* (3), A12.

(42) Bardi, U.; Tiscone, P.; Rovida, G. Carbon Monoxide Dissociation on Polycrystalling Cobalt. *Appl. Surf. Sci.* **1986**, *27*, 299–317.

(43) Bridge, M. E.; Comrie, C. M.; Lambert, R. M. Chemisorption Studies on Cobalt Single Crystal Surfaces. *Surf. Sci.* **1977**, *67*, 393–404.

(44) Vaari, J.; Lahtinen, J.; Talo, A.; Hautojärvi, P. Promotion of CO Dissociation by Magnesia on Co(0001). *Surf. Sci.* **1991**, *251–252*, 1096–1099.

(45) Sadki, A.; Castellani, N. J.; Cabeza, G. F.; Le, P. Growth and Structure of Thin Platinum Films Deposited on Co (0001) Studied by Low-Energy Electron Diffraction , X-Ray Photoelectron Spectroscopy , Ultraviolet Photoelectron Spectroscopy and Scanning Tunneling Microscopy. *Surf. Sci.* **2000**, *457*, 121–133.

(46) Lahtinen, J.; Vaari, J.; Kauraala, K. Adsorption and Structure Dependent Desorption of CO on Co(0001). *Surf. Sci.* **1998**, *418*, 502–510.

(47) Papp, H. The Chemisorption of Carbon Monoxide on a CO(1010) Single Crystal Surface. Studied by LEED,UPS,EELS,AES and Work Function Measurements. *J. Phys. Chem. B* **1982**, *86*, 555–562.

(48) Lahtinen, J.; Vaari, J.; Kauraala, K.; Soares, E. A.; Van Hove, M. A. LEED Investigations on Co(0001): The Overlayer. *Surf. Sci.* **2000**, *448*, 269–278.

(49) Vattuone, L.; Savio, L.; Rocca, M. Bridging the Structure Gap: Chemistry of Nanostructured Surfaces at Well-Defined Defects. *Surf. Sci. Rep.* **2008**, *63* (3), 101–168.

(50) Cabeza, G. F.; Légaré, P.; Castellani, N. J. Adsorption of CO on Co (0001) and Pt – Co (0001) Surfaces : An Experimental and Theoretical Study. *Surf. Sci.* **2000**, *465*, 286–300.

(51) Redhead, P. History of Vacuum Devices. *Cern Eur. Organ. Nucl. Res.* **1999**, 281–290.

(52) Madey, T. E. Early Applications of Vacuum, from Aristotle to Langmuir. *Journal of Vacuum Science & Technology*. 1984, pp 110–117.

(53) Lesker, K. J. Kurt J. Lesker Company KF (QF) Flanges Technical Notes Vacuum Science is our Business.

(54) Seah, M. Post-1989 Calibration Energies for X-Ray Photoelectron Spectrometers and the 1990 Josephson Constant. *Surf. Interface Anal.* **1989**.

(55) Cabrera, A. L.; Garrido M, W. H.; Volkmann, U. G. Studies of Carbon Monoxide and

Hydrogen Adsorption on Nickel and Cobalt Foils Aimed at Gaining a Better Insight into the Mechanism of Hydrocarbon Formation. *Catal. Letters* **1994**, *25* (1–2), 115–126.

(56) Haanappel, V.; Corbach, H. Van. The Pyrolytic Decomposition of Aluminium-Tri- Sec-Butoxide during Chemical Vapour Deposition of Thin Alumina Films. *Thermochim. Acta* **1994**, *240*, 67–77.

(57) He, C. Z.; Wang, H.; Zhu, P.; Liu, J. Y. Adsorption and Dissociation of NO on Ir(100): A First-Principles Study. *J. Chem. Phys.* **2011**, *135* (20).

(58) Lide, D. R. *CRC Handbook of Chemistry and Physics.*, 94th ed.; **2013**; Vol. 53.

(59) Gardner, P.; Martin, R.; Nalerinski, R.; Lamorit, C. L. A. Adsorption of Nitric Oxide on lr{1O0}: Influence of Substrate Reconstruction. *J. Am. Chem. Soc.* **1995**, *91* (20), 3575–3584.

(60) Ge, Q.; King, D. A.; Marzari, N.; Payne, M. C. First Principles Calculation of the Energy and Structure of Two Solid Surface Phases on Ir {100}. *Surf. Sci.* **1998**, *418*, 529–535.

(61) Khatua, S.; Liu, Z. P.; King, D. A. NO Restructuring of Surface Ir and Bond Formation to Preadsorbed O on Ir{1 0 0} at 95 K. *Surf. Sci.* **2005**, *584* (2–3), 214–224.

(62) Erikat, I. A.; Hamad, B. A.; Khalifeh, J. M. First-Principles Study of Molecular NO Dissociation on Ir(100) Surface. *Eur. Phys. J. B* **2014**, *87* (2).

(63) Johnson, K.; Ge, Q.; Titmuss, S.; King, D. A. Unusual Bridged Site for Adsorbed Oxygen Adatoms: Theory and Experiment for Ir{100}-(1×2)-O. *J. Chem. Phys.* **2000**, *112* (23), 10460–10466.

(64) Held, G.; Wander, A.; King, D. A. Variations of LEED Intensities with Angle of Incidence and the Influence on Spot Profiles. *Phys Rev. B* **1995**, *51* (24), 17856.

(65) Feyer, V.; Plekan, O.; Skála, T.; Cháb, V.; Matolín, V.; Prince, K. C. The Electronic Structure and Adsorption Geometry of L-Histidine on Cu(110). *J. Phys. Chem. B* **2008**, *112* (110), 13655–13660.

(66) Clegg, M. L.; Morales De La Garza, L.; Karakatsani, S.; King, D. A.; Driver, S. M. Chirality in Amino Acid Overlayers on Cu Surfaces. *Top. Catal.* **2011**, *54* (19–20), 1429–1444.

(67) Barlow, S. M.; Raval, R. Complex Organic Molecules at Metal Surfaces: Bonding, Organisation and Chirality. *Surf. Sci. Rep.* **2003**, *50* (6–8), 201–341.

(68) Eralp, T.; Shavorskiy, A.; Zheleva, Z. V.; Held, G.; Kalashnyk, N.; Ning, Y.; Linderoth, T. R. Global and Local Expression of Chirality in Serine on the Cu{110} Surface. *Langmuir* **2010**, *26* (24), 18841–18851.

(69) Kyriakou, G.; Beaumont, S. K.; Lambert, R. M. Aspects of Heterogeneous Enantioselective Catalysis by Metals. *Langmuir* **2011**, *27* (16), 9687–9695.

(70) Clayden, J.; Greeves, N.; Warren, S. *Organic Chemistry*, 2nd ed.; OUP Oxford: Oxford, **2012**.

(71) Barlow, S. M.; Louafi, S.; Le Roux, D.; Williams, J.; Muryn, C.; Haq, S.; Raval, R. Polymorphism in Supramolecular Chiral Structures of R- and S-Alanine on Cu(110). *Surf. Sci.* **2005**, *590* (2–3), 243–263.

(72) Nyberg, M.; Odelius, M.; Nilsson, A.; Pettersson, L. G. M. Hydrogen Bonding between Adsorbed Deprotonated Glycine Molecules on Cu(110). *J. Chem. Phys.* **2003**, *119* (23), 12577.

(73) Iwai, H.; Emori, A.; Egawa, C. STM Study of L-Serine Adsorption on Cu(001). *Surf. Sci.* **2006**, *600* (8), 1670–1673.

(74) Barlow, S. M.; Raval, R. Complex Organic Molecules at Metal Surfaces: Bonding, Organisation and Chirality. *Surf. Sci. Rep.* **2003**, *50* (6–8), 201–341.

(75) Fan, W. C.; Ignatiev, A. Structure Analysis of the Cu(110)-(1X2) Surface Reconstruction Induced by Alkali-Metal Adsorption. *Phys. Rev. B* **1990**, *41* (14), 9692–9696.

(76) Davis, H. L.; Noonan, J. R.; Jenkins, L. H. Determination of a Cu(110) Surface Constraction by LEED Intensity Analysis. **1979**, *83*, 559–571.